

Characterization of Temporal-Mode Transformations via
Spectral Interferometry

by

MOSTAFA E. EL DEMERY

A dissertation accepted and approved in partial fulfillment of the
requirements for the degree of
Doctor of Philosophy
in Physics

Dissertation Committee:

Steven van Enk, Chair

Brian J. Smith, Advisor

Stephanie A. Majewski, Core Member

Andrew H. Marcus, Institutional Representative

University of Oregon

Spring 2024

© 2024 Mostafa E. El Demery
This work is licensed under a Creative Commons
Attribution-NonCommercial-NoDerivs (United States) License.



DISSERTATION ABSTRACT

Mostafa E. El Demery

Doctor of Philosophy in Physics

Title: Characterization of Temporal-Mode Transformations via Spectral Interferometry

The use of temporal-mode encoding for quantum information science has gained interest due to its robustness to environmental perturbation and suitability for integrated photonics. Temporal-mode transformations, analogous to interferometric networks for spatial-mode encoding, form the basis of many quantum information protocols utilizing temporal-mode encoding. Accurate and efficient characterization of temporal-mode transformations is essential to ensure precise manipulation of quantum information encoded in the temporal modes of light. This dissertation presents a method to determine the temporal-mode transformation of a device by means of spectral interferometry. We demonstrate the feasibility of the method to extract the temporal mode transformation from a suitable set of measurements and set constraints on experimental parameters for achieving characterization. We anticipate that this approach to assess temporal-mode transformations will be applicable to a broad range of systems being pursued in quantum information applications.

CURRICULUM VITAE

NAME OF AUTHOR: Mostafa E. El Demery

GRADUATE AND UNDERGRADUATE SCHOOLS ATTENDED:

University of Oregon, Eugene, USA
University of Cambridge, Cambridge, UK
Menoufiya University, Shebin El Kom, Egypt

DEGREES AWARDED:

Doctor of Philosophy, Physics, 2024, University of Oregon
Master of Advanced Studies, Applied Mathematics, 2013, University of Cambridge
Master of Science, Physics, 2012, Menoufiya University
Bachelor of Science, Physics, 2008, Menoufiya University

PROFESSIONAL EXPERIENCE:

Research Graduate Fellow: University of Oregon, Sep 2018–Dec 2023
Teaching Assistant: University of Oregon, Sep 2017–Aug 2018
R&D Intern: Coherent Inc., August 2016–August 2017
Research Assistant: Egyptian Atomic Energy Agency, May 2010–Aug 2011

GRANTS, AWARDS, AND HONORS:

EMANUEL Optical, Molecular, and Quantum Sciences Scholarship
Cambridge Overseas Trusts Scholarship
African Institute for Mathematical Sciences Scholarship
Egyptian Academy of Sciences, Research and Technology Award

PUBLICATIONS:

M. E. El Demery et al., *Characterization of quantum pulse gates via spectral interferometry*, To be submitted.
M. E. El Demery et al., *Characterization of a temporal-mode sorter using multiple-delay crossed-beam spectral interferometry*. Proc. SPIE 12405, Nonlinear Frequency Generation and Conversion: Materials and Devices XXII (2023), 124050I

M. E. El Demery and S. M. A. Maize., *Sideband control of optical bistability in tunnel-coupled double quantum wells*. *Nonlinear Optics and Quantum Optics* **46** (2012), 1

ACKNOWLEDGMENTS

First and foremost, all Praise is due to Allah Almighty for every blessing He has bestowed upon me throughout my life. Without His unwavering assistance, support, and direction, this PhD would have never been completed. "Truly, my prayers, my worship, my life and my death are all dedicated to Allah – Lord of all worlds. He stands alone without any equal, and I obey His commandments, humbly submitting myself."

I am infinitely grateful and indebted to my parents!

In loving memory of my dear father, the reservoir of wisdom he shared with me has proven to be immeasurable and invaluable. He stood as my ultimate life mentor and an irreplaceable source of guidance and inspiration. Your words, forever etched within me, echo gently: "I hope to live until the day I witness you as a scientist." The weight of regret settles in, Papa, as I grasp that you're no longer here to witness my journey, a dream unfulfilled. *What is life but a chain of broken dreams!* The moment of your departure, just as I embarked on my PhD journey, remains as one of the most poignant experiences I have endured. Yet, amidst the ache, I find a measure of solace knowing you are in a more peaceful place now.

In cherished memory of my beloved mother, whose profound impact on my life will forever remain a beacon of love and inspiration. It was her unwavering belief in my potential that led her to gift me physics books at such a tender age, igniting a passion that has since become the cornerstone of my journey. Her remarkable foresight and nurturing spirit cultivated within me a deep-rooted love for physics that has guided me through countless challenges. My heart overflows with gratitude for the countless sacrifices she made, and the unending support she offered, allowing me to stand on the precipice of my PhD. I am profoundly sorry that she departed this world just before my academic journey's dawn, unable to witness the fruition of her boundless belief in me. Though she is physically absent, her spirit remains my guiding star, illuminating every step of my pursuit with her everlasting love.

I am grateful to my advisors, Profs. Michael Raymer and Brian Smith for their guidance throughout my PhD and I am thankful that I have been supported by the National Science foundation grant No. 1820789 that covered my research towards earning my PhD. I would also like to extend my sincere gratitude to the members who served on my PhD committee. I would like to extend my thanks to the members of our group; Amy, Clark, Jack, Matt and Sarah.

I am greatly thankful to my siblings, Muhammed, Ahmed, Mahmoud, Zahraa

and Randa for their love and support. I would like to thank my dear friends, Alaa and Ali, Estelle and Nick for their generosity and being like a family to me. Many thanks are due to Dileep Reddy, Markus Allgeier, Ibrahim Ahmed and Mohammed Mounier for their help and support throughout my work. I would like to extend my gratitude towards Liz Wallace for all her efforts in making my defense a reality.

To Mariam, Khadiga, Romaisaa, Lamar and all my nieces and nephews, I love you little ones!

At the culmination of this journey, I am deeply grateful to several individuals whose unwavering support was integral to the completion of this work. I extend my heartfelt appreciation to Profs. Stephanie Majewski, Steven van Enk, and Richard Taylor for their invaluable support during the final stages of my PhD pursuit. Among them, Prof. Stephanie Majewski stands out as the true hero of this journey. Without her indispensable support, it is unlikely that you would be holding this PhD thesis in your hands today. My gratitude towards her knows no bounds, and I will forever cherish the debt of gratitude I owe to her.

For ALLAH

"Truly, my prayers, worship, life, and death are all dedicated to Allah – the Lord of all worlds. He stands alone without any equal, and I obey His commandments, humbly submitting myself."

TABLE OF CONTENTS

Chapter	Page
LIST OF FIGURES	11
LIST OF TABLES	19
1. MOTIVATION AND PROBLEM STATEMENT	20
1.1. Quantum Networks	20
1.2. Quantum Information Encoding	26
1.3. Temporal-Mode Transformations and QPGs	30
1.4. Motivation and Problem Statement	31
1.5. Outline	33
2. THEORETICAL BACKGROUND	35
2.1. Maxwell's Equations	35
2.2. Temporal Modes of Light	39
2.3. Ultrashort Pulses	41
2.4. Nonlinear Optics	45
2.5. Temporal-Mode Transformations	53
2.6. Quantum Pulse Gate	54
3. CHARACTERIZATION OF TEMPORAL-MODE TRANSFORMATIONS	62
3.1. Spectral Interferometry	63
3.2. Characterization of the Transfer Map $G(\omega, \omega')$	65
4. EXPERIMENTAL CHARACTERIZATION OF THE QPG	82
4.1. Waveguide	82
4.2. Ultrafast Laser	84
4.3. 4f-Line Pulse Shaping	86
4.4. Characterization of QPGs	97
5. FUTURE DIRECTIONS	115
5.1. Blue Part: $G_{br}(\omega_b, \omega'_r)$	115
5.2. Temporal-Mode Characterization (Blue)	118

6. CONCLUSION	126
REFERENCES CITED	128

LIST OF FIGURES

Figure	Page
1.1.	The top shows a notional quantum network composed of quantum nodes for processing and storing quantum states and quantum channels for distributing quantum information (from [Kim08]). The bottom shows two examples of quantum nodes as a quantum dot and an atomic vapor connected through a quantum channel based on optical fibers and quantum frequency conversion (QFC) to manipulate the photon frequencies suitable for each quantum node (from [RS12]). 22
1.2.	TMs encoding of the amplitude in different time bins (left) and the amplitude in different frequency bins (center) and first three modes of Hermite-Gaussian modes (right). 29
1.3.	A schematic depiction of the action of a QPG. A multi-mode weak input signal $E_s(t)$ co-propagates with a classical single-mode pulse $E_p(t)$ acting as a gating pulse in order to extract photons in a well-defined TM $E_B(t)$ whose shape matches that of the gating pulse. 31
2.1.	The spectral $\tilde{f}_j(\omega)$ (left) and temporal $f_j(t)$ (right) amplitudes of the first three TMs in the Hermite-Gaussian basis. 41
2.2.	Schematic depiction of a quantum pulse gate operation (From [Bre14]). 55
2.3.	Schemes showing frequency conversion in parametric down-conversion (a) and quantum pulse gating (b). 56
2.4.	A schematic depiction of a TMT as a beam-splitter-like transformation for TMs. Part of mode $A(\omega'_r)$ in the red band gets transmitted into $C(\omega_r)$ and the other part gets "converted" into $D(\omega_b)$ in the blue band. Same and opposite transformation applies for $B(\omega'_b)$ 57
2.5.	Green transfer map $G_{rr}(\omega_r, \omega'_r)$ for an ideal QPG with selectivity ~ 1 (a), for a realistic QPG with selectivity ~ 0.5 (b) and for a realistic QPG with selectivity ~ 0.25 (c). 60
2.6.	Filtering representation Eq. (2.87) that shows the unfiltered $G_{rr}(\omega_r, \omega'_r)$ (a), the no-pump Dirac delta (b) which is represented by the diagonal white line and the filtered $\tilde{G}_{rr}(\omega_r, \omega'_r)$ (c). 61

3.1. Schematic setup of a Mach-Zehnder interferometer to characterize amplitude and phase of an ultrashort pulse. A pulse $A(\omega)e^{i\omega t}$ from a laser source is split by a beam splitter (BS) into a top arm that picks up a phase $\phi(t)$ to be characterized and a reference arm (bottom) that picks up a time delay τ . The two-arms pulses $A(\omega)e^{i\omega t + \phi(\omega)}$ and $A(\omega)e^{i\omega(t-\tau)}$ interfere and their spectral interferogram is measured by a spectrometer. WP stands for waveplate and BS stands for beam splitter.	64
3.2. Spectrum in the frequency domain that would be measured on a spectrometer due to the interference of two pulses.	64
3.3. Spectrum in the time domain when the inverse Fourier transform is applied on $\tilde{S}(\omega)$	65
3.4. Schematic diagram of TMTs that describe intraband transformations where there is no frequency conversion and interband transformations where there is frequency conversion.	66
3.5. Schematic setup of interferometric process tomography. A short optical pulse out of a Ti-Saph laser at central wavelength $\lambda_0 = 810\text{nm}$ and bandwidth of $\Delta\lambda = 8\text{nm}$ is split at a beam splitter to generate a probe pulse $A(\omega)$ at central wavelength $\lambda_0 = 805\text{nm}$ and bandwidth of $\Delta\lambda = 5\text{nm}$ and a replica as a reference pulse. The probe pulse is sent to a tunable delay, T , then undergoes a TMT. The interference between the output $C(\omega, T)$ and the reference is measured at one output of the second beam splitter.	67
3.6. Layout of the reconstruction algorithm.	69
3.7. Numerical simulation of tomographic measurements of the linear phase shifter with phase function $\phi(\omega) = \alpha \omega$	72
3.8. Contour plots of the transfer functions of the LPS with a phase function $\phi(\omega) = \alpha \omega$	73
3.9. Spectral phase and intensity after the action of a linear spectral phase shifter with a phase function $\phi(\omega) = \alpha \omega$, where $\alpha = (2000/\omega_0)$ with $\omega_0 = 2\pi c/\lambda_0$ and $\lambda_0 = 803\text{nm}$	75
3.10. Contour plots of the real (left) and imaginary (right) parts of the transfer function of the Dirac delta with a linear Phase $\Phi(\omega) = \alpha\omega$	76
3.11. Quadratic spectral phase and intensity of the input and output pulses undergoing a quadratic phase shift with a phase function $\phi(\omega) = \beta \omega^2$ where $\beta = (150/\omega_0)^2$	76

3.12.	Contour plots of the real (left) and imaginary (right) parts of the transfer function of the Dirac delta with a quadratic phase $\Phi(\omega) = \beta\omega^2$	77
3.13.	A scheme showing sum-frequency generation (SFG) in a nonlinear $\chi^{(2)}$ waveguide that is periodically poled to ensure quasi phasematching.	78
3.14.	A proposed experimental setup to characterize interband TMTs. A probe mode $A(\omega_r)$ is split into two parts to probe the mode sorter and gets frequency doubled to be a reference for the "blue" interferometer. The outputs of the mode sorter $C(\omega_r)$ and $D(\omega_b)$ interfere with $A(\omega_r)$ and $A_{SHG}(\omega_b)$ respectively.	79
4.1.	The wavenumber (β) and the group velocity ($v_g = d\omega/d\beta$) versus wavelength (λ) for a typical 5 μm wide, periodically-poled, MgO:LN waveguide. Also shown are the r-, s-, and p- bands that I utilize for SFG.	83
4.2.	Blue light spectra generated from the QPG in a typical run. The SFG peak requires both the pump and signal to be present at the input, whereas the pump-only SHG peak remains even without the signal, and occurs due to imperfections in poling.	84
4.3.	The spectrum of the in-house built Ti:Sapphire laser system tuned at $\lambda_0 \sim 811$ nm and bandwidth $\Delta\lambda \sim 8$ nm.	85
4.4.	Schematic of a 4f-line pulse shaper that consists of two diffraction gratings, two lenses and a spatial light modulator (SLM) placed at the Fourier plane.	87
4.5.	Modulation mask on the SLM (a) and the respective spectra (b) of the carved out pulses in the pump and signal bands.	89
4.6.	Linear phase ramp applied to the probe band of the modulation mask on the SLM.	90
4.7.	Schematic of spatial displacement of the $m = 1$ reflected beam due to spatial-temporal interference in the pulse shaper when a linear phase mask is applied to the SLM to temporally delay the incident pulse. Larger displacements occur when the pulse shaper is not well-optimized (top) and when longer delays are imposed (far right and far left beams). The efficiency of the coupling in the waveguide is directly affected by beam displacement (right).	91
4.8.	Measured loss profile $L(T)$ (Black), a Sinc function (Blue) and a Gaussian profile (Red).	93

4.9. Modeling of the loss profile $L(T)$ in the spectral domain over finite time scan T as a Gaussian profile (a —c) and a Sinc function (d —f) for bandwidths $\tau_L \sim \tau_A$ in (a, c) and $\tau_L \sim 10\tau_A$ in (b, d) compared to the bandwidth of the probe pulse. 3D plots of (b, d) are shown in (e, f).	94
4.10. A schematic depiction of the probe and pump interaction inside the waveguide in the time domain where we fix the pump and sweep the probe along time with the transmission function profile. The transmission function value is almost constant over the interaction time of the pump and probe. . . .	94
4.11. The numerically-simulated unfiltered $G_{rr}(\omega, \omega')$ transfer map (a) due to the broadening of the loss spectral profile $\Delta(\omega, \omega')$ (b) and the filtered $G_{rr}(\omega, \omega')$ transfer map (c) calculated by subtracting $G_{rr}(\omega, \omega') - \Delta(\omega, \omega')$ for an ideal QPG with selectivity ~ 1 . The bandwidth of the broadening is $\tau_L \sim \tau_A$	96
4.12. The numerically-simulated unfiltered $G_{rr}(\omega, \omega')$ transfer map (a) due to the broadening of the loss spectral profile $\Delta(\omega, \omega')$ (b) and the filtered $G_{rr}(\omega, \omega')$ transfer map (c) calculated by subtracting $G_{rr}(\omega, \omega') - \Delta(\omega, \omega')$ for a realistic QPG with selectivity ~ 0.5 . The bandwidth of the broadening is proportional to $1/\tau_L \sim 1/\tau_A$ where τ_L is the time duration of the transmission profile of the loss and τ_A is the temporal duration of the probe pulse $A(\omega)$	96
4.13. The numerically-simulated unfiltered $G_{rr}(\omega, \omega')$ transfer map (a) due to the broadening of the loss spectral profile $\Delta(\omega, \omega')$ (b) and the filtered $G_{rr}(\omega, \omega')$ transfer map (c) calculated by subtracting $G_{rr}(\omega, \omega') - \Delta(\omega, \omega')$ for a realistic QPG with selectivity ~ 0.5 . The bandwidth of the broadening is $\tau_L \sim 10\tau_A$	97
4.14. Experimental setup of our technique of characterizing the quantum pulse gate that reconstructs the Green transfer map $G_{rr}(\omega_r, \omega'_r)$ in the IR spectral region. WP is waveplate, BS is beam splitter, OF is optical filter, AL is aspherical lens and DM is dichroic mirror. Other optical components are not shown.	98

4.15. CE versus $\bar{\gamma} \propto \sqrt{P_{\text{pump}}}$ for zeroth and first order HG pump pulses. Curves are theory in case of Schmidt modes and marker points are for zeroth and first order HG signal pulses. Blue circles show the case where both pump and signal are zeroth-order HG shape, burble squares is for zeroth-order HG pump and first-order HG signal, red diamond-shped points are for first-oredr HG pump and zeroth-oreder HG signal and green triangle points are for first-rder HG shapes for both pump and signal pulses. The three gray boxes designate the values of the pump power at which we run our CTMT-SI technique. From right to left, we have weak (0.32 mW), moderate (0.98 mW) and strong (2.92 mW) pump powers.	99
4.16. Selectivity versus $\bar{\gamma} \propto \sqrt{P_{\text{pump}}}$, Eq. (2.85), of the QPG under examination for a zeroth-order HG pump shape.	100
4.17. Numerically-simulated spectral interferograms over time scan of different delays between the pump and probe of the QPG.	101
4.18. Experimental measurement of the spectral interferograms over time scan of different delays between the pump and probe of the QPG.	102
4.19. Experimental reconstruction of the no-pump IR Green transfer map $\Delta(\omega_r, \omega'_r)$ of the QPG that will be subtracted from the reconstructed $G_{rr}(\omega_r, \omega'_r)$ to give the filtered $\tilde{G}_{rr}(\omega_r, \omega'_r)$ through Eq. (3.27).	103
4.20. Experimental reconstruction of the IR Green transfer map $G_{rr}(\omega_r, \omega'_r)$ of the QPG for zeroth order HG pump pulse at 2.92 mW. The unfiltered $G_{rr}(\omega_r, \omega'_r)$ (left) when the pump is switched on. By subtracting the no-pump transfer map $\Delta(\omega_r, \omega'_r)$ in Fig. 4.19, we obtain the filtered $\tilde{G}_{rr}(\omega_r, \omega'_r)$ (right). . .	104
4.21. Experimental reconstruction of the IR Green transfer map $G_{rr}(\omega_r, \omega'_r)$ of the QPG for first order HG pump pulse at 2.92 mW. The unfiltered $G_{rr}(\omega_r, \omega'_r)$ (left) when the pump is switched on. By subtracting the no-pump transfer map $\Delta(\omega_r, \omega'_r)$ in Fig. 4.19, we obtain the filtered $\tilde{G}_{rr}(\omega_r, \omega'_r)$ (right). . .	104
4.22. Experimental reconstruction of the IR Green transfer map $G_{rr}(\omega_r, \omega'_r)$ of the QPG for second order HG pump pulse at 2.92 mW. The unfiltered $G_{rr}(\omega_r, \omega'_r)$ (left) when the pump is switched on. By subtracting the no-pump transfer map $\Delta(\omega_r, \omega'_r)$ in Fig. 4.19, we obtain the filtered $\tilde{G}_{rr}(\omega_r, \omega'_r)$ (right). . .	105
4.23. Experimental reconstruction of the IR Green transfer map $G_{rr}(\omega_r, \omega'_r)$ of the QPG for zeroth order HG pump pulse at 0.98 mW. The unfiltered $G_{rr}(\omega_r, \omega'_r)$ (left) when the pump is switched on. By subtracting the no-pump transfer map $\Delta(\omega_r, \omega'_r)$ in Fig. 4.19, we obtain the filtered $\tilde{G}_{rr}(\omega_r, \omega'_r)$ (right). . .	105

4.24. Experimental reconstruction of the IR Green transfer map $G_{rr}(\omega_r, \omega'_r)$ of the QPG for first order HG pump pulse at 0.98 mW. The unfiltered $G_{rr}(\omega_r, \omega'_r)$ (left) when the pump is switched on. By subtracting the no-pump transfer map $\Delta(\omega_r, \omega'_r)$ in Fig. 4.19, we obtain the filtered $\tilde{G}_{rr}(\omega_r, \omega'_r)$ (right). . .	106
4.25. Experimental reconstruction of the IR Green transfer map $G_{rr}(\omega_r, \omega'_r)$ of the QPG for second order HG pump pulse at 0.98 mW. The unfiltered $G_{rr}(\omega_r, \omega'_r)$ (left) when the pump is switched on. By subtracting the no-pump transfer map $\Delta(\omega_r, \omega'_r)$ in Fig. 4.19, we obtain the filtered $\tilde{G}_{rr}(\omega_r, \omega'_r)$ (right). . .	106
4.26. Experimental reconstruction of the IR Green transfer map $G_{rr}(\omega_r, \omega'_r)$ of the QPG for zeroth order HG pump pulse at 0.32 mW. The unfiltered $G_{rr}(\omega_r, \omega'_r)$ (left) when the pump is switched on. By subtracting the no-pump transfer map $\Delta(\omega_r, \omega'_r)$ in Fig. 4.19, we obtain the filtered $\tilde{G}_{rr}(\omega_r, \omega'_r)$ (right). . .	107
4.27. Experimental reconstruction of the IR Green transfer map $G_{rr}(\omega_r, \omega'_r)$ of the QPG for first order HG pump pulse at 0.32 mW. The unfiltered $G_{rr}(\omega_r, \omega'_r)$ (left) when the pump is switched on. By subtracting the no-pump transfer map $\Delta(\omega_r, \omega'_r)$ in Fig. 4.19, we obtain the filtered $\tilde{G}_{rr}(\omega_r, \omega'_r)$ (right). . .	107
4.28. Experimental reconstruction of the IR Green transfer map $G_{rr}(\omega_r, \omega'_r)$ of the QPG for second order HG pump pulse at 0.32 mW. The unfiltered $G_{rr}(\omega_r, \omega'_r)$ (left) when the pump is switched on. By subtracting the no-pump transfer map $\Delta(\omega_r, \omega'_r)$ in Fig. 4.19, we obtain the filtered $\tilde{G}_{rr}(\omega_r, \omega'_r)$ (right). . .	108
4.29. (a) CE of the first 3 Schmidt modes for the first 3 HG modes of the pump deduced from our CTMT-SI technique with strong pump power of 2.92 mW. (b) The difference between conversion efficiencies of CTMT-SI against directly measured CE of the QPG showing good agreement within $\pm 2\%$. .	110
4.30. (a) CE of the first 3 Schmidt modes for the first 3 HG modes of the pump deduced from our CTMT-SI technique with moderate pump power of 0.98 mW. (b) The difference between conversion efficiencies of CTMT-SI against directly measured CE of the QPG showing reasonable agreement within $\pm 3\%$.	110
4.31. (a) CE of the first 3 Schmidt modes for the first 3 HG modes of the pump deduced from our CTMT-SI technique with weak pump power of 0.32 mW. (b) The difference between conversion efficiencies of CTMT-SI against directly measured CE of the QPG showing noticeable error of approximately 8%.	111

4.32. Zeroth (a), first (b) and second (c) Schmidt modes of the Green transfer map $G_{rr}(\omega_r, \omega'_r)$ reconstructed from CTMT-SI plotted with HG modes for clarification	112
4.33. The overlap between zeroth (a) and first (b) Schmidt modes and HG modes.	112
4.34. CE vs $\bar{\gamma}$ for zeroth (a) and first (b) HG pump and both HG and Schmidt signal modes.	113
4.35. Spectral interferometric measurement (blue) of the zeroth order (a), first order (b) and second order (c) Schmidt modes generated by the pulse shaper and obtained from our CTMT-SI technique (red) and respective HG modes (Gray) shown for reference.	114
5.1. SHG-CTMT-SI schematic proposed setup. The QPG is probed by a probe pulse $A(\omega_r, T)$ and the upconverted output blue is $D(\omega_b, T) = \int d\omega'_r G_{br}(\omega_b, \omega'_r) A(\omega_r, T)$ which is interfered with a frequency-doubled replica of the reference pulse $A_{\text{SHG}}(\omega_b)$ in the blue interferometer to extract $G_{br}(\omega_b, \omega_r)$	116
5.2. DFG-CTMT-SI schematic proposed setup. The QPG is probed by a probe pulse $A(\omega_r, T)$ and the upconverted output blue is $D(\omega_b, T) = \int d\omega'_r G_{br}(\omega_b, \omega'_r) A(\omega_r, T)$ which is coupled with a replica of the reference pulse $A(\omega_r)$ in the DFG waveguide. The DFG signal $A_{\text{DFG}}(\omega_r, T)$ is then interfered with a replica of the reference pulse $A(\omega_r)$ in the red interferometer to extract $G_{br}(\omega_b, \omega_r)$	117
5.3. DFG Spider.	119
5.4. Layout of the reconstruction algorithm.	121
5.5. DFG-SPIDER Schematic proposed setup.	122
5.6. Spectrum of the Ti:Sapphire laser (solid) and the spectra of the two reference pulses used to characterize the blue unknown pulse.	122
5.7. Numerical simulation of the steps of reconstructing an ultrashort pulse in the blue spectral region of a zeroth-order HG TM. The top left plot shows the spectrum $S_i(T_1, T_2; \omega)$ while scanning the time delay T_1 and fixing T_2 . The bottom left is the Fourier transform of $S_i(T_1, T_2; \omega)$ with respect to T_1 which shows the DC signal with the AC sideband signals. The top left shows the correlation $\langle \mathcal{E}_B(T_2) \mathcal{E}_B(\Omega) \rangle$ compared to the filtered spectral measurement $FS_i(\Omega, T_2; \omega)$ in the frequency domain while the bottom right shows the same in the time domain.	124

5.8. Numerical simulation of the steps of reconstructing an ultrashort pulse in the blue spectral region of a first-order HG TM. The top left plot shows the spectrum $S_i(T_1, T_2; \omega)$ while scanning the time delay T_1 and fixing T_2 . The bottom left is the Fourier transform of $S_i(T_1, T_2; \omega)$ with respect to T_1 which shows the DC signal with the AC sideband signals. The top right shows the correlation $\langle \mathcal{E}_B(T_2) \mathcal{E}_B(\Omega) \rangle$ compared to the filtered spectral measurement $FS_i(\Omega, T_2; \omega)$ in the frequency domain while the bottom right shows the same in the time domain. 125

LIST OF TABLES

Table	Page
4.1. Transmission coefficients for strong pump power of 2.92 mW.	108
4.2. Transmission coefficients for moderate pump power of 0.98 mW.	109
4.3. Transmission coefficients for weak pump power of 0.32 mW.	109

CHAPTER 1

MOTIVATION AND PROBLEM STATEMENT

*One accurate measurement is
worth a thousand expert
opinions.*

Grace Hopper

1.1 Quantum Networks

The concept of quantum networks [Kim08; WEH18] introduces a framework for networking quantum computational resources, facilitating the quantum-based exchange and manipulation of information. This infrastructure is tailored to address computational challenges that are currently beyond the reach of classical systems. Through the application of quantum phenomena such as entanglement and superposition, quantum networks is anticipated to significantly enhance computational paradigms, particularly in the realms of quantum computing, communication, and metrology [Bri+10].

The superiority of quantum connectivity over classical networks is not merely confined to the enhanced capabilities of specific algorithms but extends to the fundamental architectural advantages. A network comprising k nodes, each equipped with n quantum bits (qubits), linked via classical channels, would possess a state space dimensionality of 2^nk . On the other hand, a network employing quantum connectivity would exhibit a state space of an exponentially greater magnitude, quantified as 2^{kn} [Kim08]. This quantum connectivity is essential in addressing and potentially overcoming the inherent challenges of size-scaling and error-correlation, which currently impede the expansion of quantum processing machines.

Quantum networks, characterized by their ability to exploit quantum mechanical phenomena for communication and computation, are poised to revolutionize the way information is processed and transmitted. The bedrock of these networks lies in quantum entanglement [EPR35; NC10a; Hor+09], a unique correlation between quantum entities across vast distances, underpinning secure communication protocols and distributed quantum computing. Quantum entanglement in quantum networks serves as the primary means for establishing non-local connections

between nodes. This phenomenon underpins various quantum communication protocols, including quantum teleportation [Ben+93; Bou+97; NC10b] and entanglement swapping [Žuk+93; Pan+12], which are essential for achieving long-distance quantum communication and for the construction of quantum repeaters [Bri+98; San+11]. Recent experiments have demonstrated entanglement distribution via satellites and through optical fibers over hundreds of kilometers, showcasing the feasibility of global quantum networks [Yin+17; Lia+18].

A model of a quantum network incorporates quantum nodes that are responsible for the generation, processing, and storage of quantum information. The interconnection of these nodes is facilitated through quantum channels that ensure the high-fidelity transmission of quantum states and the distribution of quantum entanglement across the network's entirety. A notional schematic example of a quantum network is shown in Fig. 1.1 in which the different nodes could be realized through different platforms that are summarized below. Two examples of such nodes, namely, a quantum dot and an atomic vapor are shown while they are connected through an optical fiber based quantum channel. Since the optical frequencies suitable for quantum dots ω_1 , for atomic vapors ω_2 and for optical fibers ω_3 are in different spectral regimes, quantum frequency conversion (QFC) [Kum90] is employed to manipulate photon frequencies to facilitate the connection of different quantum nodes examples shown in Fig. 1.1.

Platforms for Quantum Network Nodes

Quantum networks are composed of nodes that store and process quantum information and can be implemented using various physical systems, each with its unique advantages and challenges. For example, trapped ions and superconducting circuits offer high-fidelity quantum operations, quantum dots provide a versatile source of single photons, and diamond color centers offer robustness at room temperature. As the field progresses, hybrid approaches combining the advantages of different platforms, along with advancements in materials and fabrication techniques, are likely to play a crucial role in realizing scalable and efficient quantum networks.

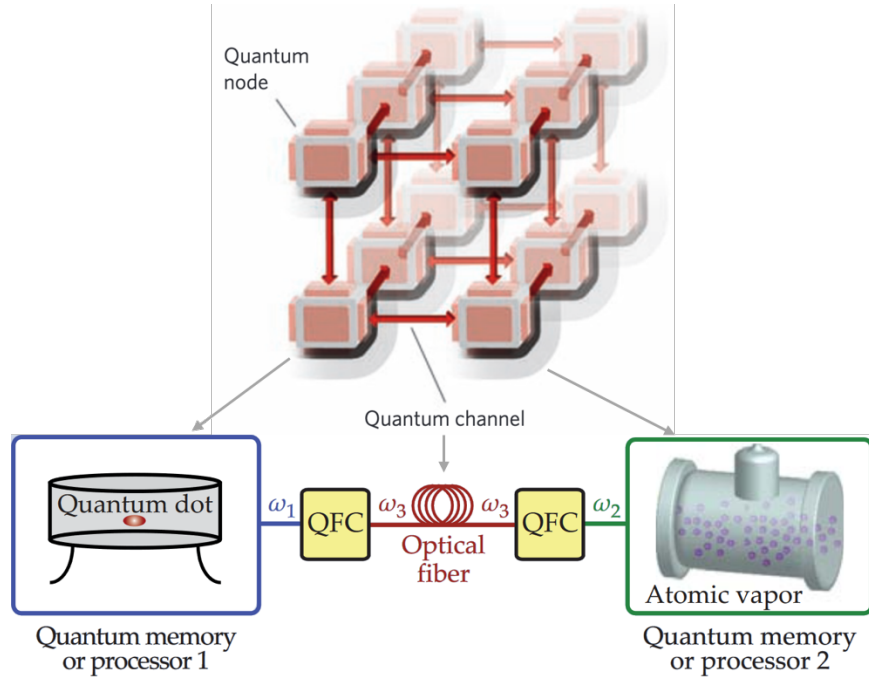


Figure 1.1. The top shows a notional quantum network composed of quantum nodes for processing and storing quantum states and quantum channels for distributing quantum information (from [Kim08]). The bottom shows two examples of quantum nodes as a quantum dot and an atomic vapor connected through a quantum channel based on optical fibers and quantum frequency conversion (QFC) to manipulate the photon frequencies suitable for each quantum node (from [RS12]).

Trapped Ions

Trapped ion systems [Mon+14] stand out in quantum networking due to their remarkable coherence times and high operational fidelities. In these systems, ions are confined using electromagnetic fields in ultra-high vacuum environments, allowing for precise quantum state manipulation through laser or microwave interactions [Mon+95]. The ability to individually address ions and perform entangling operations makes trapped ions a versatile platform for quantum computation and communication tasks. Notable advancements include the implementation of quantum error correction codes and the realization of entangled states over significant distances, underscoring the potential for trapped ions in scalable quantum networks [Ha14].

Recent advancements in trapped ion technology include the development of

scalable ion trap architectures and the integration of ion traps with photonic devices for efficient information transfer [Kru+23]. High-fidelity quantum gates and state preparation, essential for quantum computation and communication, have been demonstrated with trapped ions, showcasing their potential as versatile nodes in quantum networks [BW08].

Superconducting Circuits

Superconducting circuits leverage the principles of superconductivity to create quantum coherent electronic devices [NPT99]. These circuits operate at microwave frequencies and are cooled to millikelvin temperatures to maintain quantum coherence. The Josephson junction, a fundamental component, enables non-linear inductance, essential for qubit construction and manipulation. Superconducting qubits [Mar15], characterized by their design variations such as transmon, flux, and phase qubits, offer rapid gate operations and scalability. Integration with classical control electronics and advancements in coherence times position superconducting circuits as a promising platform for quantum processors and quantum network nodes.

The scalability of superconducting circuits, combined with their compatibility with existing semiconductor fabrication techniques, makes them a strong candidate for quantum computing and networking applications. Recent breakthroughs include the demonstration of quantum error correction, entanglement of multiple qubits, and the development of quantum processors with increasing qubit counts [DS13]. Moreover, significant advancements in quantum computing using superconducting circuits have yielded remarkable outcomes, notably exemplified by the Google experiment [Aru+19]. This experiment stands out for its pioneering demonstration of a quantum computer solving a task that poses formidable challenges for classical counterparts due to its time-intensive nature that underscores quantum supremacy.

Quantum Dots

Quantum dots are semiconductor nano-crystals that can confine electrons or holes in three dimensions [Han+07], leading to discrete energy levels and the ability to emit or absorb single photons. This property is harnessed in quantum networks for generating indistinguishable photons, crucial for quantum communication protocols. Techniques such as cavity quantum electrodynamics (cavity QED) [HR06] enhance the interaction between quantum dots and light, improving the efficiency

of single-photon sources and enabling deterministic entanglement generation. The integration of quantum dots with photonic structures like waveguides and micro-cavities further facilitates their application in scalable quantum photonic networks [Lod+15].

Significant research has focused on integrating quantum dots with photonic structures to enhance light-matter interaction, essential for efficient information transfer in quantum networks [SSW17]. Challenges remain in achieving deterministic entanglement generation and reliable integration with other components of quantum networks, but ongoing advancements in material science and nano-fabrication are promising.

Diamond Color Centers

Diamond color centers, particularly the nitrogen-vacancy (NV) centers [Doh+13], offer a robust platform for quantum networking due to their long coherence times and operation at room temperature. NV centers are point defects in diamond where a carbon atom is replaced by a nitrogen atom adjacent to a vacancy. They can be optically initialized and read out, and their spin states can be coherently manipulated using microwave radiation. The capacity for NV centers to be entangled over long distances through photon-mediated interactions makes them suitable for quantum repeater architectures, crucial for overcoming distance limitations in quantum communication [BK05].

Diamond color centers are particularly attractive for quantum networks due to their potential for integration with photonic devices and the possibility of creating entangled networks over long distances using optically transmitted photons. Research efforts [CH13] are directed towards enhancing the efficiency of photon emission and collection, as well as developing scalable fabrication techniques for diamond-based quantum devices.

Connecting Quantum Network Nodes

Optical Fibers

Optical fibers, the backbone of modern telecommunications, also play a crucial role in quantum networks by providing a medium for transmitting quantum information, typically encoded in photons. The key advantage of using optical fibers is

their ability to guide light over relatively long distances with low loss, making them suitable for quantum communication. However, quantum communication via optical fibers faces significant challenges, primarily due to photon loss and decoherence mechanisms such as birefringence and scattering, which degrade the quantum information.

To counteract these challenges, quantum repeaters have been developed by which the range of quantum communication is extended by segmenting the transmission line into shorter, manageable sections [Tak+15]. Within each segment, quantum entanglement is established and then extended across the network through entanglement swapping and entanglement purification protocols to maintain high-fidelity quantum states over long distances [Bri+98; Dua+01].

Free Space

Free-space quantum communication offers an alternative to fiber-based systems by using the atmosphere or the vacuum of space as the transmission medium. This approach is particularly appealing for establishing long-distance and satellite-based quantum networks. The successful demonstration of satellite-to-ground quantum key distribution (QKD) has marked a significant milestone, showcasing the feasibility of global quantum communication networks that can overcome the range limitations of fiber networks [Yin+17; Lia+18]. However, free-space communication is not without its challenges. Atmospheric turbulence, absorption, and scattering can significantly affect the fidelity of the transmitted quantum states. Adaptive optics and sophisticated error correction techniques are employed to mitigate these effects, ensuring the reliable transmission of quantum information through free-space channels.

Hybrid Approaches

Hybrid quantum networks represent an innovative approach to quantum connectivity, combining different transmission media and quantum technologies to optimize network performance. In a hybrid network, short- and medium-range connections might be established using optical fibers, while long-distance and intercontinental links could rely on free-space channels or satellite links. Integrating different quantum node platforms within a hybrid network requires the development of efficient interfaces for quantum state conversion and transfer [RE24]. Quantum trans-

ducers [Mar+17a], which convert quantum states between different physical systems are crucial for this purpose. These devices enable the coherent transfer of quantum information across diverse network components, facilitating a seamless and versatile quantum network architecture [Kim08; Kur+15].

1.2 Quantum Information Encoding

Upon discussing the grand scheme of quantum networks in the previous section, it follows that quantum information encoding in quantum networks is a critical aspect that defines how information is represented, processed, and transmitted within the network. The choice of encoding scheme directly impacts the network's capacity, security, and resilience to errors. Quantum information encoding in spin states is a fundamental aspect of quantum computing and quantum information processing, particularly in systems such as trapped ions and quantum dots. Spin states are associated with the intrinsic angular momentum of particles, such as electrons or atoms, and can serve as quantum bits (qubits) in quantum information processing.

However, for the scope of the present work, I confine myself to discussing quantum information encoding in photonics-based quantum networks. The quantum information encoding in photonics systems follows directly from the definition of modes of the quantized electric field of photons, propagating in the \mathbf{z} -direction, in terms of the creation and annihilation operators, such that

$$\hat{\mathbf{E}}(\mathbf{r}, t) = \sum_{n, \epsilon} E_0 [g_n(\mathbf{x}, \mathbf{y}) f_n(t) \hat{a}_{n, \epsilon} e^{-i\omega_{n, \epsilon}(t-z/c)} + \text{H.c.}], \quad (1.1)$$

where ϵ represents the index corresponding to polarization states, E_0 is the electric field amplitude and $\hat{a}_{n, \epsilon}$ is the annihilation operator for the photon in mode n with polarization ϵ . The functions $g_n(\mathbf{x}, \mathbf{y})$ and $f_n(t)$ are the transverse spatial and temporal profiles of mode n respectively. Photons are ideal candidates for encoding and transferring of quantum information due to their suitability for long-distance transmission and accessibility to various degrees of freedom. Single-photon excitations are common due to the light-matter interface with material quantum systems in which a single photon is coupled with a material excitation. In this context, the quantum information is encoded in the mode occupied by the photon.

Polarization

Encoding quantum information in the polarization degrees of freedom is one of the simplest and most widely used methods for encoding, especially in photonic systems. The photon can be described by its polarization direction (e.g., horizontal $|H\rangle$ or vertical $|V\rangle$) to represent the binary quantum states $|0\rangle$ and $|1\rangle$, respectively. Polarization encoding is particularly suitable for free-space quantum communication due to its robustness against environmental changes. However, in optical fibers, polarization can be affected by birefringence, requiring careful management to maintain the integrity of the quantum states.

While polarization has been extensively utilized due to the simplicity of its manipulation through beam splitters and waveplates, it is limited to a two-dimensional Hilbert space. This dimensional limitation poses challenges for various quantum protocols, such as quantum key distribution and quantum teleportation, that can benefit from using a larger Hilbert space in order to reach strong security and stability of the information processing and transmission [Zha+14]. To overcome this limitation, alternative degrees of freedom of the photon, such as transverse electric-field distribution and temporal structure [Pay92; TG66] are exploited.

Spatial-Mode Encoding

Quantum information encoding using the spatial-mode degrees of freedom of the electric field harnesses the spatial structure of light beams, such as their amplitude and phase patterns across the transverse plane, to encode quantum bits (qubits) or even higher-dimensional quantum units (qudits). The spatial modes of light, especially those described by Laguerre-Gaussian (LG) and Hermite-Gaussian (HG) modes, exhibit distinct patterns that can be orthogonally separated, providing a basis for high-dimensional quantum encoding.

Spatial-mode encoding utilizes the complex amplitude distribution of light in the transverse plane. For instance, LG modes are characterized by an azimuthal phase dependence $\exp(il\phi)$, where l is the azimuthal quantum number representing the orbital angular momentum (OAM) of the photon, and ϕ is the azimuthal angle. This OAM of light introduces an additional degree of freedom, enabling the encoding of information in the "twist" of the light beam, with different values of l corresponding to different quantum states [All+92].

Hermite-Gaussian modes, on the other hand, are defined by their Cartesian symmetry and are characterized by two quantum numbers corresponding to the number of nodes in the horizontal and vertical directions. Both LG and HG modes provide a rich set of orthogonal states that can be exploited for quantum encoding, significantly expanding the information capacity beyond conventional polarization. OAM-encoded photons can be generated and manipulated using specially designed optical elements, but they are sensitive to turbulence in free-space communication, posing challenges for practical implementations [Mai+01].

Temporal Modes of Light

Spectral-Temporal Modes (TMs) [SR07] are essentially different ways in which a photon can be distributed across different frequencies and times. Spectral and temporal terms are used interchangeably through Fourier transformation, therefore, the term *temporal modes* (TMs) will be used exclusively to describe spectral and/or temporal modes. They have gained significant attention in recent years owing to their robustness to environmental degradation and suitability to integrated optics platforms [Bre+15b]. TMs information encoding is more practical than that of the spatial modes of the electromagnetic field, OAM encoding, in case of single-mode fiber networks and dispersion-engineered waveguides due to TM interferometric stability [Ans+17; Ans18].

Although it is tempting to call a TM the ‘state’ of the photon, such language can be misleading if used without care. In particular, it does not easily apply to quantum states of the field beyond individual photons [Lam95; SR07]. In this sense, a TM is more like a ‘*container*’ which is populated by an arbitrary state of light.

Eq. (1.1) sets no bound on the dimension of the Hilbert space that is spanned over by TMs. As a result, single photons in the TMs basis have much larger capacity for information encoding contrasted to that of the 2-dimensional Hilbert space of photon polarization or electron spin. A key difference is that a set of TMs is in principle infinite dimensional, which implies temporal mode transformations (TMTs) are also infinite dimensional. However, when considering quantum information encoding, we often limit the infinite dimensional space to a finite subspace of modes. This offers the ability to utilize large-dimensional alphabet spaces that greatly increases the information capacity of the photon and improves the efficiency of quantum information processing.

The left column of Fig. 1.2 shows information encoding through the amplitude of the pulse in different time bins while the middle column shows encoding in the amplitude of the pulse in different frequency bins or with different carrier frequencies, as well as the first three HG modes in the right column. While the left two columns show that orthogonal bases can be constructed by slicing up the space into different bins, the right column depicts orthogonal intensity-overlapping waveforms. In other words, different TMs of light propagate in the same spatial mode.

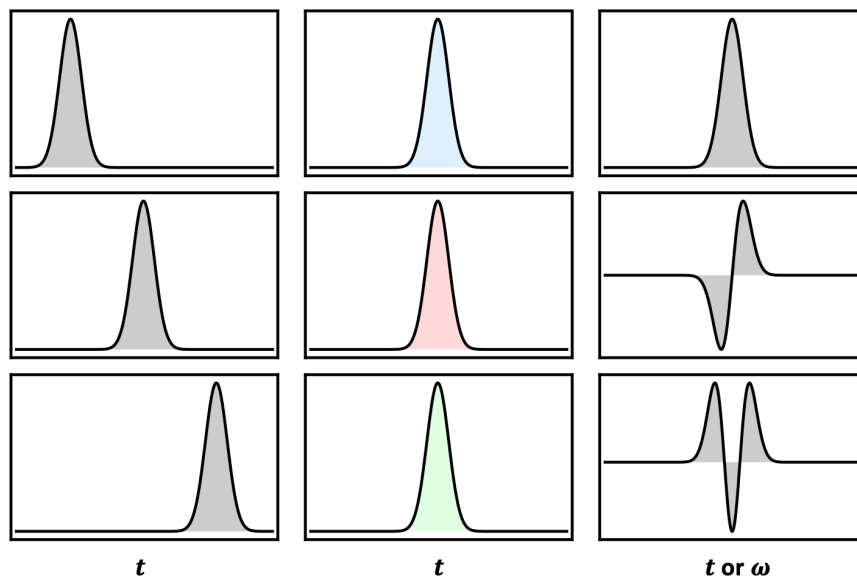


Figure 1.2. TMs encoding of the amplitude in different time bins (left) and the amplitude in different frequency bins (center) and first three modes of Hermite-Gaussian modes (right).

The manipulation of temporal modes, transform one set of TMs to another, requires precise control over the phase and amplitude of the electromagnetic field, typically achieved through ultrafast optical techniques such as amplitude and phase modulators, pulse shapers, and programmable optical delays. The ability to manipulate TMs underlies many QIS applications including computation, communications and networking. However, in order to take advantage of TMs, it is necessary to be able to generate [Mey+17], manipulate [Ans+18b], and characterize [NTH12] them efficiently and accurately. Among the tools that manipulate TMs, the quantum pulse gate (QPG) emerges as a promising tool in the realm of channels connecting different quantum network nodes as shown in Fig. 1.1.

1.3 Temporal-Mode Transformations and QPGs

Many quantum photonics applications rely on the ability to implement unitary linear transformations on modes. For TMs, the mapping between two different TMs, $A(\omega')$ as an input and $C(\omega)$ as an output of a temporal-mode transformation (TMT), can be written as

$$C(\omega) = \int d\omega' G(\omega, \omega') A(\omega'), \quad (1.2)$$

where $G(\omega, \omega')$ is the transformation map for a single frequency band in which both frequencies ω and ω' are within the same spectral band. An essential example of TMTs is what is called a quantum pulse gate (QPG).

QPGs [EBS11; Red+13] are critical for manipulating temporal modes, acting as a selective interface between different temporal modes or between temporal modes and other degrees of freedom of light, such as polarization or frequency. Analogous to a polarizing beam splitter, which directs input polarizations of light into two orthogonal spatial-mode outputs, the QPG was introduced as a TM selective beam splitter. A schematic depiction of the action of a QPG is shown in Fig. 1.3 where a multi-mode input signal pulse $E_s(t)$ co-propagates with a single-mode control (gating or pump) pulse $E_p(t)$. The QPG converts one mode from the input signal field that matches the shape of the pump pulse to an output mode, while all other modes pass through without being affected.

A QPG operates through the nonlinear optical interaction of sum-frequency generation (SFG) that is engineered so that it occurs only for a specific temporal mode of the quantum pulse, enabling selective manipulation of quantum information encoded in temporal modes. The utility of QPGs extends to the implementation of high-fidelity quantum gates, essential for quantum computing, and the conversion of quantum information between different physical platforms [Bre+15a]. QPGs can play a crucial role in quantum networking applications, such as quantum state teleportation and entanglement swapping, where the ability to selectively interact with specific temporal modes enables the coherent transfer of quantum information across network nodes [Gao+13]. Furthermore, QPGs can enhance the performance of quantum key distribution (QKD) systems by enabling the use of high-dimensional temporal mode entanglement, increasing the security and data rate of quantum communication [Bre+15a].

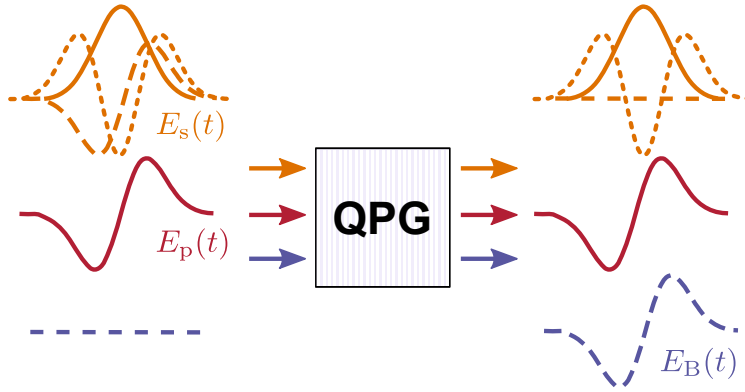


Figure 1.3. A schematic depiction of the action of a QPG. A multi-mode weak input signal $E_s(t)$ co-propagates with a classical single-mode pulse $E_p(t)$ acting as a gating pulse in order to extract photons in a well-defined TM $E_B(t)$ whose shape matches that of the gating pulse.

1.4 Motivation and Problem Statement

Now that I have laid out most of the pieces of the puzzle of quantum networks, I pick up one piece and study it for my PhD so that I could put it in the right place. That piece, in other words the project of my PhD, is the characterization of temporal-mode transformations, specifically QPGs. In general, the characterization of devices in quantum information processing experiments is critical to ensure that devices under investigation are performing to desired specifications. For the sake of scalability and mass manufacturing of such devices, efficient and simple techniques of characterization are preferred.

The characterization of devices used in quantum information processing experiments typically relies on quantum process tomography (QPT) [MRL08; DP09] in which an overcomplete set of probe quantum states is prepared and subjected to the quantum process of interest, and then measurements on the output states are made. The measurement outcomes are used to reconstruct the complete set of operators that describe the quantum process, providing a comprehensive understanding of how the *state* of the system evolves.

To ensure that TMTs, which are classical mode transformations, perform to desired specification, similar techniques to quantum process tomography (QPT) can be used. One approach to characterize TMTs is based upon the analogy of

QPT in which the TMT is probed with an overcomplete set of orthogonal and non-orthogonal known input TMs, which was used to (partially) characterize a QPG [Ans+17]. This approach measured the conversion efficiency of each input TM, but did not verify the coherence properties or temporal shapes of the transmitted signal. In this approach, increasing the size of the TM space probing the TMT in order to obtain accurate characterization has two drawbacks. The number of measurements of overlap probabilities, $[N \times (N + 1)]^2$, required for characterization grows quartically large as the size of the TM space where N is the number of the mutually-unbiased states. Second, in case of higher-dimensional spaces, spectral side lobes of TMs start to appear requiring spectral filtering to improve the characterization process [Ans+18b]. On top of the computational complexity in case of large dimensional spaces, the TM structure of highly efficient QPGs is slightly distorted due to the time-ordering effects of the strong-coupling of the interaction Hamiltonian [QS16; Chr+15]. These pitfalls pose challenges to the efficient and accurate characterization of TMTs.

In the present work, we introduce a method to characterize TMTs based upon spectral interferometry (CTMT-SI). The approach involves probing the TMT with a set of Gaussian pulses displaced in time. The output of the TMT is interfered with a coherent reference pulse, which has spectral support larger than the output temporal mode, followed by spectrally-resolved measurement. In the proposed method, the TMT can be directly determined from the measured spectral interference pattern with no need for data fitting. This direct method allows precise determination of the TMT implemented by a device without the need of spectral filtering.

I introduce three different measurements that provide a complete framework of characterizing QPGs. The first measurement relies on investigating the *transmitted* signal in the same frequency band of the input pulse. I call this experiment IR-CTMT-SI since the spectral region of the TMs employed in this experiment is in the infrared (IR) region. The reconstruction of the transfer map of the TMT in this experiment provides valuable information about the temporal structure of input modes as well as transmitted output modes in the same spectral region. In addition, the transmission probabilities of the TMs as well conversion probabilities to TMs in a different spectral region, blue in our case, are provided. Due to the unitarity of TMTs of QPGs, the temporal structures of the input TMs in the blue spectral region, if the QPG were to perform in reverse action, are the same as the

temporal structure of both input and output TMs in the IR spectral regions. The only missing piece of information that is not provided by the IR-CTMT-SI is the temporal structure of the output TMs in the blue spectral region for which I propose the following two experiments.

The second measurement is proposed to reconstruct the transfer map of the TMT in the blue spectral region and follows similarly the method of the IR-CTMT-SI of the first measurement. I provide two schemes for this experiment based on second harmonic generation (SHG-CTMT-SI) and on difference frequency generation (DFG-CTMT-SI) respectively. Either SHG-CTMT-SI or DFG-CTMT-SI are expected to provide information about the temporal structure of input and output TMs in the blue spectral region as well as conversion probabilities (and transmission probabilities) and the temporal structure of the input TMs in the IR spectral region if the QPG were to perform in reverse action where the input signal is in the blue spectral region and the QPG relies on DFG instead of SFG. Again, information about the temporal structure of the output TMs in the IR spectral region is not provided from this Blue-CTMT-SI measurement.

The third measurement I propose is what I call DFG-SPIDER which directly characterizes the temporal structure of the output TMs in the blue spectral region, the missing piece of information from the IR-CTMT-SI experiment. The naming stems from using a similar technique to SPIDER in characterizing ultrashort pulses while employing DFG to access the temporal structure of the TMs in the blue spectral region.

In this thesis, I present the theory of characterizing QPGs and an experimental demonstration of the CTMT-SI in the IR spectral region during my PhD and show preliminary results showcasing the validity of our proposed CTMT-SI technique. The remaining two experiments could very well be considered for a future PhD project if someone is interested in this line of work.

1.5 Outline

The present thesis is outlined as follows. Chapter 2 reviews the theoretical background of ultrashort pulses of light as well as describing their propagation in nonlinear media. The mathematical framework of temporal modes as the basis employed for quantum information encoding is also presented along with temporal-mode transformations (TMTs). QPGs as an example of TMTs are reviewed with

the no-pump correction of the Green transfer maps.

In Chapter 3, I review spectral interferometry as the principal tool of our characterization method of the Green transfer maps of QPGs. I then lay out the theory of characterizing TMTs based on crossed-beam spectral interferometry.

Chapter 4 presents the experimental demonstration of the CTMT-SI method in the transmitted Green transfer map as well as discussing some of the issues that arise in the experiment. In Chapter 5, I propose other experiments that completes the proposed characterization technique that could be implemented in the future. I finally draw the findings and lay out the conclusions in Chapter 6.

CHAPTER 2

THEORETICAL BACKGROUND

2.1 Maxwell's Equations

In this section I give the formal framework of describing ultrashort pulses of electromagnetic fields. The starting point is the Maxwell equations that govern the dynamics of the electric $\mathbf{E}(\mathbf{r}, t)$ and magnetic $\mathbf{B}(\mathbf{r}, t)$ fields that are expressed in their differential form as

$$\nabla \cdot \mathbf{E} = \frac{\rho}{\varepsilon_0}, \quad (2.1)$$

$$\nabla \cdot \mathbf{B} = 0, \quad (2.2)$$

$$\nabla \times \mathbf{E} = -\frac{\partial \mathbf{B}}{\partial t}, \quad (2.3)$$

$$\nabla \times \mathbf{B} = \mu_0 \mathbf{J} + \mu_0 \varepsilon_0 \frac{\partial \mathbf{E}}{\partial t}, \quad (2.4)$$

where ρ and \mathbf{J} are the charge and current densities respectively, ε_0 and μ_0 are the free space permittivity and permeability respectively. In free space and where there are no charge or currents ($\rho = 0$ and $\mathbf{J} = 0$), Eqs. (2.1 —2.4) are decoupled into two, three-dimensional wave equations. For the electric \mathbf{E} and magnetic \mathbf{B} fields, the wave equations are

$$(\nabla^2 - \mu_0 \varepsilon_0 \partial_t^2) \mathbf{E} = 0, \quad (2.5)$$

$$(\nabla^2 - \mu_0 \varepsilon_0 \partial_t^2) \mathbf{B} = 0. \quad (2.6)$$

A particularly insightful solution to these equations is the plane wave characterized by its uniform amplitude and phase across any plane perpendicular to the direction of propagation. Considering a harmonic time dependence $e^{-i\omega t}$, where ω is the angular frequency, and assuming a wave propagating in the positive z-direction, the electric and magnetic fields of the plane wave can be expressed as

$$\mathbf{E}(z, t) = \mathbf{E}_0 e^{i(kz - \omega t)}, \quad (2.7)$$

$$\mathbf{B}(z, t) = \mathbf{B}_0 e^{i(kz - \omega t)}, \quad (2.8)$$

where $k = \omega/c$ is the wave number, and $c = 1/\sqrt{\mu_0 \varepsilon_0}$ is the speed of light in vacuum. The electric field $\mathbf{E}(\mathbf{r}, t)$ and magnetic field $\mathbf{B}(\mathbf{r}, t)$ are perpendicular to each other and to the direction of propagation.

Slowly Varying Envelope Approximation (SVEA)

In many practical situations, especially in laser physics and nonlinear optics, the amplitude of the electromagnetic wave does not remain constant but varies slowly over the distance of one wavelength or the period of one optical cycle. The SVEA is an approximation that simplifies the analysis of such waves by assuming that the envelope of the wave varies much more slowly than the phase. This allows for the separation of the rapidly oscillating phase from the slowly varying envelope.

Neglecting polarization and transverse spatial mode distribution, for an electric field described as $E(z, t) = A(z, t)e^{i(kz - \omega t)}$, where $A(z, t)$ represents the slowly varying amplitude, the SVEA leads to the following approximate form of the wave equation

$$\left(\frac{\partial^2}{\partial z^2} + 2ik \frac{\partial}{\partial z} \right) A(z, t) \approx 0. \quad (2.9)$$

Under the SVEA, terms involving the second derivative of the amplitude with respect to z are neglected, yielding a first-order differential equation that is more tractable for analytical and numerical solutions

$$\frac{\partial A(z, t)}{\partial z} + \frac{i}{2k} \frac{\partial^2 A(z, t)}{\partial t^2} \approx 0. \quad (2.10)$$

This equation describes the propagation of the slowly varying amplitude of the wave in a dispersive medium, where k is a function of ω , reflecting the medium's dispersive properties. The plane wave solutions of Maxwell's equations provide a foundational understanding of electromagnetic wave propagation, while the SVEA offers a powerful tool for analyzing wave propagation in more complex settings, such as dispersive and nonlinear media. Together, these concepts form the bedrock of much of modern optics and photonics, underpinning technologies ranging from laser design to telecommunications systems.

Paraxial Approximation

In the domain of wave optics, when examining light as a wave phenomenon, the direction of propagation typically aligns perpendicular to the wavefronts, except in cases involving spatial walk-off. For configurations such as lasers and optical fibers where the propagation of light is guided along effectively straight paths, the paraxial approximation is applied in order to separate the transverse field profile

from its longitudinal periodic functional dependence. In case of linearly polarized and compact free-space beams, where most of the beam intensity is confined close to the principal axis with a single maximum in the transverse plan, the field amplitude can be approximated by the fundamental Gaussian mode

$$E(r, z) = E_0 \frac{w_0}{w(z)} \exp\left(-\frac{r^2}{w^2(z)}\right) \exp\left(i\left[kz - \arctan\frac{z}{z_R} + \frac{kr^2}{2R(z)}\right]\right), \quad (2.11)$$

where r is the radial distance from the principal axis, z is the axial distance from the beam's focal point, $k = 2\pi/\lambda$ is the wavenumber, $w(z)$ is the beam radius at which the field amplitudes fall to $1/e$ of their axial values, $w_0 = w(0)$ is the waist radius, $R(z)$ is the radius of curvature of the beam's wavefronts, and $\arctan(z/z_R)$ is the phase attributed to the phase velocity of light. The beam radius $w(z)$ and radius of curvature $R(z)$ are expressed as

$$w(z) = w_0 \sqrt{1 + \left(\frac{z}{z_R}\right)^2}, \quad R(z) = z \left[1 + \left(\frac{z_R}{z}\right)^2\right]. \quad (2.12)$$

Under circumstances where the paraxial approximation is applicable, a second-order differential equation, derived from Maxwell equations, can be simplified to a more tractable first-order equation. This simplification provides a more straightforward understanding of beam propagation and critical limitations such as the minimum beam parameter product $BPP = w_0\theta$, where θ is the beam divergence half-angle (measured in the far field). The paraxial approximation necessitates ensuring that divergence angles remain significantly below 1 radian, indicating that the beam radius at the waist should be substantially larger than the wavelength.

Plane-wave and wave-packet modes

The classical Hamiltonian of the electromagnetic field in free space is given as

$$H = \frac{\varepsilon_0}{2} \int d^3r [|\mathbf{E}|^2 + c^2|\mathbf{B}|^2]. \quad (2.13)$$

Since the Hamiltonian is quadratic in the canonical fields, this is a linear field theory [Ste07], meaning that the Hamiltonian equations of motion are linear differential equations. Therefore, we can express the fields as a superposition of a set of non-interacting normal modes (such as plane waves) and then apply the general

quantization procedure for all modes [Dir27]. It is customary to write down the Hermitian field operators into positive-frequency and negative-frequency parts,

$$\hat{\mathbf{E}}(\mathbf{r}, t) = \hat{\mathbf{E}}^{(+)}(\mathbf{r}, t) + \hat{\mathbf{E}}^{(-)}(\mathbf{r}, t), \quad (2.14)$$

$$\hat{\mathbf{B}}(\mathbf{r}, t) = \hat{\mathbf{B}}^{(+)}(\mathbf{r}, t) + \hat{\mathbf{B}}^{(-)}(\mathbf{r}, t), \quad (2.15)$$

where $\hat{\mathbf{E}}^{(-)}(\mathbf{r}, t) = \left[\hat{\mathbf{E}}^{(+)}(\mathbf{r}, t) \right]^\dagger$ and $\hat{\mathbf{B}}^{(-)}(\mathbf{r}, t) = \left[\hat{\mathbf{B}}^{(+)}(\mathbf{r}, t) \right]^\dagger$. For orthonormal modes that are characterized by the wave vector \mathbf{k} and polarization index $\sigma = \pm 1$ and for plane waves as the choice for mode functions $\mathbf{f}(\mathbf{r}, t)$

$$\mathbf{u}_{\mathbf{k},\sigma} = \mathbf{e}_{\mathbf{k},\sigma} \exp(i\mathbf{k} \cdot \mathbf{r}), \quad (2.16)$$

the field operators can be rewritten as

$$\hat{\mathbf{E}}^{(+)}(\mathbf{r}, t) = i \sum_{\sigma} \int \frac{d^3k}{(2\pi)^3} \sqrt{\frac{\hbar c k}{2\varepsilon_0}} \hat{a}_{\mathbf{k},\sigma} \mathbf{u}_{\mathbf{k},\sigma}(\mathbf{r}) \exp(-i\omega_{\mathbf{k}} t), \quad (2.17)$$

$$\hat{\mathbf{B}}^{(+)}(\mathbf{r}, t) = i \sum_{\sigma} \int \frac{d^3k}{(2\pi)^3} \sqrt{\frac{\hbar c k}{2\varepsilon_0}} \hat{a}_{\mathbf{k},\sigma} \left[\frac{\mathbf{k}}{ck} \times \mathbf{u}_{\mathbf{k},\sigma}(\mathbf{r}) \right] \exp(-i\omega_{\mathbf{k}} t), \quad (2.18)$$

with the corresponding normalization conditions and commutators

$$\int d^3r \mathbf{u}_{\mathbf{k},\sigma}^*(\mathbf{r}) \cdot \mathbf{u}_{\mathbf{k}',\sigma'}(\mathbf{r}) = (2\pi)^3 \delta^{(3)}(\mathbf{k} - \mathbf{k}') \delta_{\sigma,\sigma'}, \quad (2.19)$$

$$\left[\hat{a}_{\mathbf{k},\sigma}, \hat{a}_{\mathbf{k}',\sigma'}^\dagger \right] = (2\pi)^3 \delta^{(3)}(\mathbf{k} - \mathbf{k}') \delta_{\sigma,\sigma'}. \quad (2.20)$$

The monochromatic plane-wave annihilation $\hat{a}_{\mathbf{k},\sigma}$ and creation $\hat{a}_{\mathbf{k},\sigma}^\dagger$ operators annihilate and create single-quantum of the field excitation when acting on the quantum vacuum state similar to the case of a simple harmonic oscillator such that

$$\hat{a}_{\mathbf{k},\sigma}^\dagger |0\rangle_{\mathbf{k},\sigma} = |1\rangle_{\mathbf{k},\sigma}, \quad \hat{a}_{\mathbf{k},\sigma} |1\rangle = |0\rangle_{\mathbf{k},\sigma}, \quad (2.21)$$

where the state $|n\rangle_{\mathbf{k},\sigma}$ ($n > 0$) is the n -photon Fock state defined by successive creation operators acting on the vacuum for the designated \mathbf{k}, σ plane-wave mode. One can define spatial-temporal wave-packet modes [TG66; SR07] through the non-unitary spatial Fourier transform

$$\mathbf{v}_{j,\sigma}(\mathbf{r}, t) = i \sqrt{\frac{\hbar c}{2\varepsilon_0}} \int \frac{d^3k}{(2\pi)^3} \sqrt{k} U_j^{(\sigma)}(\mathbf{k}) \mathbf{u}_{\mathbf{k},\sigma}(\mathbf{r}) \exp(-i\omega_{\mathbf{k}} t), \quad (2.22)$$

where $U_j^{(\sigma)}(\mathbf{k})$ is a unitary transformation matrix and the non-unitarity arises from the factor \sqrt{k} . As a result of the non-unitarity of the transformation, the wave-packet modes $\mathbf{v}_{j,\sigma}(\mathbf{r}, t)$ do not generally form an orthogonal set under inner product overlap integral. However, the SVEA makes us consider wave-packet modes that are monochromatic carrier waves with slowly varying envelopes whose spectra are narrowband. The transformation matrix $U_j^{(\sigma)}(\mathbf{k})$ thus becomes only nonzero around a narrow neighborhood of carrier wave vector \mathbf{k}_0 . This makes the wave-packet modes $\mathbf{v}_{j,\sigma}(\mathbf{r}, t)$ *nearly* orthogonal under the regular inner product overlap integral such that

$$\int d^3r \mathbf{v}_{j,\sigma}^*(\mathbf{r}, t) \cdot \mathbf{v}_{j',\sigma'}(\mathbf{r}, t) \approx \frac{\hbar c |\mathbf{k}_0|}{2\varepsilon_0} \delta_{j,j'} \delta_{\sigma,\sigma'}. \quad (2.23)$$

Eq. (2.22) can be used to transform the plane-wave annihilation $\hat{a}_{\mathbf{k},\sigma}$ and creation $\hat{a}_{\mathbf{k},\sigma}^\dagger$ operators into the new wave-packet annihilation $\hat{A}_{j,\sigma}$ and creation $\hat{A}_{j,\sigma}^\dagger$ operators such that

$$\hat{A}_{j,\sigma} = \int \frac{d^3k}{(2\pi)^3} \left[U_j^{(\sigma)}(\mathbf{k}) \right]^* \hat{a}_{\mathbf{k},\sigma}, \quad \hat{a}_{\mathbf{k},\sigma} = \sum_j U_j^{(\sigma)}(\mathbf{k}) \hat{A}_{j,\sigma}, \quad (2.24)$$

with the wave-packet commutation relation $[\hat{A}_{j,\sigma}, \hat{A}_{j',\sigma'}^\dagger] = \delta_{j,j'} \delta_{\sigma,\sigma'}$. The field operators can now be expressed in terms of the wave-packet operators such that

$$\hat{\mathbf{E}}^{(+)}(\mathbf{r}, t) = \sum_{j,\sigma} \hat{A}_{j,\sigma} \mathbf{v}_{j,\sigma}(\mathbf{r}, t), \quad (2.25)$$

$$\hat{\mathbf{B}}^{(+)}(\mathbf{r}, t) = \sum_{j,\sigma} \hat{A}_{j,\sigma} \left[\frac{\mathbf{k}_j}{c|\mathbf{k}_j|} \times \mathbf{v}_{j,\sigma}(\mathbf{r}, t) \right]. \quad (2.26)$$

It is worth noting that the electric field is not the optimum field for quantization in nonlinear optical media, and we would need to use the displacement field instead [HM84; QS17]. Further, the quantization of the electromagnetic field in free space is not particularly accurate for dispersive media. However, the narrowband approximation (2.23) will allow us to circumvent this problem.

2.2 Temporal Modes of Light

Temporal modes (TMs) are a weighted linear superposition of a continuum of monochromatic modes within a neighborhood of some central frequency and are

exactly orthogonal and better suited for narrowband integrated systems [Bre+15b]. Knowledge of TMs is necessary to fully understand the behavior of ultrashort pulses particularly while travelling in a beam-like geometry or in a waveguide [Blo+90]. Dropping the polarization index, Eq. (2.24) for an electromagnetic field propagating in the positive z -direction in the frequency domain reduces to

$$\hat{A}_j = \int d\omega \tilde{f}_j(\omega) \hat{a}(\omega), \quad (2.27)$$

where $\tilde{f}_j(\omega)$ is the mode function that defines the spectral amplitude of the wave-packet mode, Eq. (2.22). The inverse Fourier transform of $\tilde{f}_j(\omega)$ yields the temporal shape, $f_j(t)$, of the wave-packet mode [Bre+15b] and they satisfy the SVEA equation of motion, Eq. (2.10). The operator $\hat{a}(\omega)$ is a monochromatic annihilation operator that satisfies bosonic commutation relations $[\hat{a}(\omega), \hat{a}^\dagger(\omega')] = 2\pi\delta(\omega - \omega')$. It is worth noting that mode functions in both spectral and time domains $\tilde{f}_j(\omega)$ and $f_j(t)$ are orthogonal

$$\int \frac{d\omega}{2\pi} \tilde{f}_j^*(\omega) \tilde{f}_k(\omega) = \int dt f_j^*(t) f_k(t) = \delta_{jk}, \quad (2.28)$$

and form a complete set

$$\begin{aligned} \sum_{j=0}^{\infty} \tilde{f}_j^*(\omega) \tilde{f}_j(\omega') &= 2\pi\delta(\omega - \omega'), \\ \sum_{j=0}^{\infty} \tilde{f}_j^*(t) \tilde{f}_j(t') &= \delta(t - t'). \end{aligned} \quad (2.29)$$

Fig. 2.1 shows both the spectral $\tilde{f}_j(\omega)$ and temporal $f_j(t)$ amplitudes in the Hermite-Gaussian basis for the first three modes for $j = 0, 1, 2$.

TMs can be regarded as "buckets" that can be filled with arbitrary states of light whether they are classical or quantum mechanical. For instance, the quantum state of a single photon excitation in a specific temporal mode labeled j can be defined as

$$|1_j\rangle = \hat{A}_j^\dagger |vac\rangle, \quad (2.30)$$

where \hat{A}_j^\dagger , defined by Eq. (2.27), is the photon creation operator for temporal mode j that satisfies bosonic commutation relationship, $[\hat{A}_j, \hat{A}_k^\dagger] = \delta_{jk}$. In the TM basis, the state of any arbitrary single photon can therefore be expressed as a superposition of TMs

$$|\psi\rangle = \sum_j c_j \hat{A}_j^\dagger |vac\rangle, \quad (2.31)$$

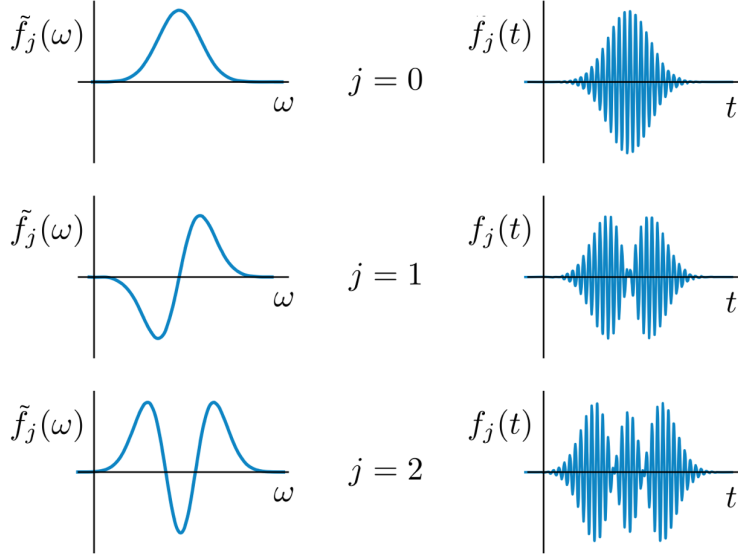


Figure 2.1. The spectral $\tilde{f}_j(\omega)$ (left) and temporal $f_j(t)$ (right) amplitudes of the first three TMs in the Hermite-Gaussian basis.

where c_j are complex-valued expansion coefficients. We can define a TM qudit as a coherent superposition of d states in the TM basis [Bre+15b]

$$|\psi\rangle_{\text{TM}}^d = \sum_{j=0}^{d-1} \alpha_j |A_j\rangle. \quad (2.32)$$

2.3 Ultrashort Pulses

Ultrashort pulses, central to the field of ultrafast optics, are light pulses with durations on the order of 100 femtoseconds (10^{-15} seconds) to picoseconds (10^{-12} seconds). These pulses are critical in probing and manipulating physical, chemical, and biological processes that unfold on extremely rapid timescales, offering insights into the fundamental mechanisms governing various phenomena at the atomic and molecular levels.

An ultrashort pulse is distinguished not only by its brief duration but also by its broad spectral content. The pulse's temporal shape, often approximated by a Gaussian or sech^2 function, encapsulates the intensity's time-dependent variation. For a Gaussian-shaped pulse, the temporal intensity profile is given by

$$I(t) = I_0 \exp\left(-\frac{4 \ln(2)t^2}{\tau^2}\right), \quad (2.33)$$

where $I(t)$ represents the intensity at time t , I_0 is the peak intensity, and τ denotes the pulse duration defined by the full width at half maximum (FWHM).

Generation

The generation of ultrashort pulses, an essential aspect of ultrafast optics, involves sophisticated techniques that enforce a coherent superposition of multiple optical frequencies within a laser cavity, leading to the emission of pulses with durations on the femtosecond to picosecond scale. This section delves into the technical aspects of ultrashort pulse generation, focusing on mode-locking mechanisms and the operational principles of commonly used ultrafast laser systems.

Mode-locking stands as the cornerstone technique for ultrashort pulse generation, characterized by the phase-locking of different longitudinal modes of a laser cavity, resulting in the constructive interference of these modes at regular intervals to produce a train of pulses. There are two types of mode-locking, namely, active and passive mode-locking. In active mode-locking, an external modulator, typically an acoustic-optic or electro-optic modulator, is placed inside the laser cavity. This modulator imposes a periodic modulation on the intracavity light at a frequency matching the cavity's round-trip frequency. The modulation depth and synchronization are crucial for effective pulse generation and can be described by

$$E(t) = E_0 \cos(\omega t) \sum_n \delta(t - nT), \quad (2.34)$$

where $E(t)$ is the electric field, E_0 is the field amplitude, ω is the angular frequency of light, δ is the Dirac delta function, and T is the round-trip time of the cavity.

On the other hand, passive mode-locking employs a saturable absorber within the laser cavity, a nonlinear optical element that exhibits decreased absorption for higher light intensities. The saturable absorber preferentially attenuates low-intensity light, allowing high-intensity pulses to form and circulate within the cavity. The dynamics of pulse formation in the presence of a saturable absorber can be modeled by the rate equations for the absorber's transmission and the intracavity pulse energy.

The main two classes of ultrafast laser systems are the solid-state lasers and fiber lasers. Fiber lasers, leveraging the advantages of doped optical fibers as the

gain medium, have emerged as versatile sources for ultrashort pulses. The inherent waveguiding properties of fibers facilitate high beam quality and excellent heat dissipation. Nonlinear polarization rotation and soliton mode-locking are key mechanisms in fiber lasers for ultrashort pulse generation.

The workhorse of solid-state lasers particularly in the field of nonlinear optics is Ti:Sapphire lasers. Ti:Sapphire lasers, utilizing Titanium-doped sapphire ($\text{Ti}^{3+} : \text{Al}_2\text{O}_3$) as the gain medium, are renowned for their broad emission bandwidth and high peak powers, enabling the generation of ultrashort pulses. The mode-locking in Ti:Sapphire lasers relies on the synchronization of the phases of longitudinal modes to produce coherent ultrashort pulses. Notably, Kerr-Lens Mode-Locking (KLM) and the use of Semiconductor Saturable Absorber Mirrors (SESAMs) are prevalent in Ti:Sapphire systems. To maintain ultrashort pulse durations, dispersion compensating elements such as prism pairs and chirped mirrors are employed within the laser cavity. Efficient operation of Ti:Sapphire lasers typically involves pumping by green light sources, such as frequency-doubled Nd:YAG lasers, to excite the Ti^{3+} ions effectively.

Spectral and Temporal Characteristics

The spectral and temporal characteristics of ultrashort pulses are fundamental to their behavior and applications in ultrafast optics. These characteristics not only define the pulse's shape and duration but also influence its interaction with various media. The spectral content of an ultrashort pulse encompasses a broad range of frequencies, a direct consequence of its short temporal duration. The spectral width at half maximum (FWHM), $\Delta\omega$, is inversely related to the pulse duration τ through the time-bandwidth product (TBP), a principle that encapsulates the inherent trade-off between temporal and spectral dimensions of a pulse. For a transform-limited Gaussian pulse, the TBP is given by:

$$\Delta\omega \cdot \tau = 0.44, \tag{2.35}$$

where c is the speed of light. This relation highlights that any attempt to compress the pulse duration further necessitates an expansion of its spectral width, and vice versa. The temporal profile of an ultrashort pulse describes its intensity variation over time. Temporal modes in ultrashort pulses refer to the coherent superpositions of frequency components that give rise to distinct temporal shapes and

phases of the pulse. These modes can be manipulated to tailor the pulse's temporal characteristics for specific applications, a process known as pulse shaping. Temporal modes are particularly relevant in the context of mode-locked lasers, where the phase relation among the longitudinal modes of the cavity defines the resulting ultrashort pulse. In mode-locked lasers, the synchronization of cavity modes leads to the generation of ultrashort pulses. The temporal mode structure of these pulses is determined by the phase relationship among the locked modes, which can be engineered through active or passive mode-locking techniques.

By modulating the amplitude and phase of individual temporal modes, pulse shaping techniques can produce ultrashort pulses with tailored temporal profiles. This is typically achieved using spatial light modulators (SLMs) or acousto-optic programmable dispersive filters (AOPDFs) in a 4f pulse shaper configuration.

Moreover, the propagation of ultrashort pulses through dispersive media can lead to temporal mode broadening, affecting the pulse duration and shape. Dispersion management strategies are essential to maintain the integrity of the temporal modes over long distances or through various media.

Dispersion and Broadening

Dispersion in optical media arises from the wavelength-dependent phase velocity of light, leading to the temporal spreading of ultrashort pulses. The dispersion can be quantitatively described by the group velocity dispersion (GVD) parameter, D (fs^2/mm), defined as

$$D = \frac{d^2k}{d\omega^2}, \quad (2.36)$$

where k is the wave number and ω is the angular frequency. The GVD parameter D indicates how different frequency components of the pulse travel at different speeds, leading to pulse broadening. It occurs when the constituent spectral components of an ultrashort pulse experience different phase delays as they propagate through a dispersive medium. For a Gaussian pulse, the broadening effect due to second-order dispersion can be modeled as

$$\tau' = \tau \sqrt{1 + \left(\frac{4 \ln(2) DL}{\tau^2} \right)^2}, \quad (2.37)$$

where τ is the input pulse duration, τ' is the broadened pulse duration after propagating a distance L through the medium, and D is the GVD parameter.

While second-order dispersion is often the dominant factor in pulse broadening, higher-order dispersion terms can significantly impact pulse shape and temporal characteristics, especially in media with strong wavelength-dependent dispersion or over long propagation distances. Third-order dispersion (TOD), for instance, can introduce asymmetric broadening and temporal shifts within the pulse envelope.

Effective dispersion management is essential for preserving ultrashort pulse characteristics in applications. Several techniques have been developed to counteract dispersion effects. Prism and grating pairs are used to introduce negative dispersion to compensate for the positive dispersion encountered allowing for the recompression of broadened pulses. Another alternative is to employ Chirped Mirrors which are specially designed mirrors that introduce wavelength-dependent delay, counteracting dispersion by reflecting different spectral components of the pulse at slightly different depths. Photonic Crystal Fibers (PCFs) can be engineered to exhibit anomalous dispersion at specific wavelengths, enabling soliton propagation and dispersion compensation within the fiber.

2.4 Nonlinear Optics

Nonlinear optical processes are essential in order to enable complex manipulation of light, and they have been exploited extensively in the classical and quantum regimes for a wide variety of purposes, e.g. classical single- and multiple-channel frequency conversion [Kum90; Cho+99], optical parametric amplification [CD03], generation of squeezed states and entangled photons [Thy+09], frequency conversion for single-photon detection [AW04; Rou+04; VK04] and to interface single photons with quantum memories [Pel+12; Rüt+17; Mar+17b]. In this section, the mathematical description of the nonlinear processes is presented with particular focus on second-order nonlinear processes in waveguides.

In nonlinear media, the induced macroscopic dielectric polarization density $\mathbf{P}(t)$, dipole moment per unit volume, responds nonlinearly to the electric field $\mathbf{E}(t)$ of sufficiently strong intensity. Due to this nonlinear dependence, one needs to consider a higher order expansion for $\mathbf{E}(t)$ while expressing the instantaneous response

$$\begin{aligned}
\mathbf{P}(t) &= \varepsilon_0 [\chi^{(1)} \mathbf{E}(t) + \chi^{(2)} \mathbf{E}(t)^2 + \chi^{(3)} \mathbf{E}(t)^3 + \dots], \\
&= \underbrace{\mathbf{P}^{(1)}(t)}_{\mathbf{P}_L(t)} + \underbrace{\mathbf{P}^{(2)}(t) + \mathbf{P}^{(3)}(t) + \dots}_{\mathbf{P}_{NL}(t)},
\end{aligned} \tag{2.38}$$

where $\chi^{(n)}$ denotes the n -th order susceptibility tensor and $\mathbf{P}_{L/NL}$ indicates the linear/nonlinear components of the polarization density. It is worth noting that the presence of higher order terms in the expansion, Eq. (2.38), gives rise to the generation of electric fields at different frequencies. In other words, the nonlinear polarization density $\mathbf{P}_{NL}(t)$ acts as a driving current source in Maxwell's equations (2.1–2.4).

If we write the electric field $\mathbf{E}(t)$ as a linear combination of fields at different frequencies $\mathbf{E}(t) = \sum_i \mathbf{E}_i \exp(i\omega_i t) + \text{c.c.}$, the quadratic nonlinear response $\mathbf{P}^{(2)}(t)$ takes the form

$$\begin{aligned}
\mathbf{P}^{(2)}(t) &\propto \underbrace{\sum_m \mathbf{E}_m^2 e^{i2\omega_m t}}_{\text{second harmonic generation}} + \text{c.c.} \\
&+ \underbrace{\sum_{\substack{mn \\ m \neq n}} \mathbf{E}_m \mathbf{E}_n^* e^{i(\omega_m - \omega_n)t}}_{\text{difference frequency generation}} + \text{c.c.} \\
&+ \underbrace{\sum_{\substack{mn \\ m \neq n}} \mathbf{E}_m \mathbf{E}_n e^{i(\omega_m + \omega_n)t}}_{\text{sum frequency generation}} + \text{c.c.} \\
&+ \underbrace{\sum_m \mathbf{E}_m \mathbf{E}_m^*}_{\text{optical rectification}} + \text{c.c.} .
\end{aligned} \tag{2.39}$$

The driving current density $\mathbf{J}(t) = \partial_t \mathbf{P}_{NL}(t)$ thus has components at twice the frequencies of the incident field and at all possible sum and difference combinations of incident frequencies, provided that the total energy is conserved. In other words, for non-zero second-order nonlinear susceptibility $\chi^{(2)}$, up to three different frequencies can be coupled together giving rise to three-wave mixing (TWM). Similarly, one can note that materials with $\chi^{(3)}$ nonlinearity allow the coupling of up to four different frequencies or four-wave mixing (FWM), and so on. The present

work deals with second-order nonlinear waveguides with non-zero $\chi^{(2)}$, therefore, I confine the discussion for TWM processes.

Three-Wave Mixing (TWM)

In nonlinear optical processes, it is customary to define different types of allowed processes according to the polarizations of the interacting fields. TWM processes, therefore, fall in three categories: *type 0* processes where all the three fields have the same polarization, *type I* processes where the two input fields (in the case of SHG, SFG or DFG) or the two generated fields (in the case of parametric down-conversion PDC) have the same polarization, and *type II* processes where the two input fields (in the case of SHG, SFG or DFG) or the two generated fields (in the case of PDC) have different polarizations. In TWM processes, the second-order nonlinear susceptibility tensor $\chi^{(2)}$ couples the induced polarization density with the electric field, in the frequency domain, through [Boy08]

$$P_i^{(2)}(\omega_m + \omega_n) = \varepsilon_0 \sum_{jk} \sum_{(mn)} \chi_{ijk}^{(2)}(-\omega_m - \omega_n, \omega_m, \omega_n) E_j(\omega_m) E_k(\omega_n), \quad (2.40)$$

where i, j and k are indices running over the polarisation components of the electric fields and (mn) denotes a summation over the possible permutations of the frequencies (ω_m, ω_n) such that $\omega_{\text{sum}} = \omega_m + \omega_n$ is constant. In general, the second order susceptibility $\chi^{(2)}$ is a rank-3, frequency dependent tensor that couples all polarization components with the three fields involved in the nonlinear process. However, when the processes under investigation lie far away from the resonant frequencies of $\chi^{(2)}$, as it is the case for processes studied in this thesis, the $\chi^{(2)}$ tensor can be greatly simplified, first by neglecting the frequency dependence and then using Kleinman's symmetry conditions [Boy08], that is

$$\chi_{ijk}^{(2)} = \chi_{jki}^{(2)} = \chi_{kij}^{(2)} = \chi_{ikj}^{(2)} = \chi_{jik}^{(2)} = \chi_{kji}^{(2)}. \quad (2.41)$$

Therefore, the notation of Eq. (2.40) can be reduced by introducing the nonlinear coefficient

$$d_{il} = \frac{\chi_{ijk}^{(2)}}{2}, \quad (2.42)$$

where l runs from 1 to 6 and is related to the combinations ($jk : 11; 22; 33; 23, 32; 31, 13; 12, 21$) respectively. Along the crystallographic directions (X, Y, Z), the second-order non-linear polarization density can be related to the incident fields as

$$\begin{bmatrix} P_X(\omega_3) \\ P_Y(\omega_3) \\ P_Z(\omega_3) \end{bmatrix} = M\varepsilon_0 \begin{bmatrix} d_{11} & d_{12} & d_{13} & d_{14} & d_{15} & d_{16} \\ d_{21} & d_{22} & d_{23} & d_{24} & d_{25} & d_{26} \\ d_{31} & d_{32} & d_{33} & d_{34} & d_{35} & d_{36} \end{bmatrix} \begin{bmatrix} E_X(\omega_1)E_X(\omega_2) \\ E_Y(\omega_1)E_Y(\omega_2) \\ E_Z(\omega_1)E_Z(\omega_2) \\ E_Y(\omega_1)E_Z(\omega_2) + E_Z(\omega_1)E_Y(\omega_2) \\ E_X(\omega_1)E_Z(\omega_2) + E_Z(\omega_1)E_X(\omega_2) \\ E_X(\omega_1)E_Y(\omega_2) + E_Y(\omega_1)E_X(\omega_2) \end{bmatrix}, \quad (2.43)$$

where M is the multiplicity factor that takes values 1 for type 0/I SHG and 2 for all other processes. The components (d_{11}, d_{22}, d_{33}) are responsible for type 0 processes, while the components ($d_{12}, d_{21}, d_{13}, d_{31}, d_{23}, d_{32}$) are responsible of type I processes. The rest components of d are responsible for type II processes.

For Lithium Niobate (LiNbO₃), the d tensor is given as [Nik05]

$$d_{\text{LiNbO}_3} = \begin{bmatrix} 0 & 0 & 0 & 0 & d_{31} & -d_{22} \\ -d_{22} & d_{22} & 0 & d_{31} & 0 & 0 \\ d_{31} & d_{31} & d_{33} & 0 & 0 & 0 \end{bmatrix}, \quad (2.44)$$

where $d_{22} = 2.1 \pm 0.21$ pm/V, $d_{31} = 4.35 \pm 0.44$ pm/V and $d_{33} = 27.2 \pm 2.7$ pm/V.

TWM in Waveguides

For the sake of simplicity and without loss of generality, the subsequent discussion introduces the equations of motion of a continuous wave (CW) waveguide mode in the presence of nonlinear polarization density induced in three-wave mixing (TWM) processes in waveguides. For a thorough derivation and solutions, the reader is referred to [Mar91; SF03]. Consider the case of a waveguide with propagation axis along z -direction, the monochromatic guided mode \mathbf{E} can be expressed as a superposition of the waveguide eigenmodes $\{\tilde{\mathcal{E}}_m\}$, that is

$$\mathbf{E}_m(x, y, z) = \sum_m \gamma_m A_m(z) \tilde{\mathcal{E}}_m(x, y) e^{-i\beta_m z}, \quad (2.45)$$

where $\beta_m = \mathbf{k}_{\parallel} = k_0 n_m$ is the propagation vector with n_m the effective index of refraction of the m -th mode, $\gamma_m = \sqrt{2/(n_m c \varepsilon_0)}$ and $A_m(z)$ is the slowly varying

field amplitude. In the SVEA, the general equation of motion of the field amplitude $A_m(z)$ in the presence of a nonlinear polarization density \mathbf{P}_{NL} is [SF03]

$$\frac{dA_m}{dz} = -i\gamma_m \frac{\omega}{4} e^{i\beta_m z} \iint dx dy \tilde{\boldsymbol{\epsilon}}_m^* \cdot \mathbf{P}_{NL,m}. \quad (2.46)$$

Eq. (2.46) describes the evolution of the envelope of the m -th eigenmode (at frequency ω_m) which depends on the nonlinear polarization density generated at the same frequency by the other fields present in the waveguide. The complete description of a TWM process requires solving Eq. (2.46) for all three fields, as they are coupled by the polarization density terms.

For a TWM process where all three fields are linearly polarized and $\omega_3 = \omega_1 + \omega_2$, the polarization density components for a SFG/DFG process ($\omega_1 \neq \omega_2$) are given by

$$P_1(\omega_1) = 2\varepsilon_0 d(x, y, z) E_2^*(\omega_2) E_3(\omega_3), \quad (2.47)$$

$$P_2(\omega_2) = 2\varepsilon_0 d(x, y, z) E_1^*(\omega_1) E_3(\omega_3), \quad (2.48)$$

$$P_3(\omega_3) = 2\varepsilon_0 d(x, y, z) E_1(\omega_1) E_2(\omega_2), \quad (2.49)$$

while for a type II SHG process ($\omega_1 = \omega_2$), the polarization density components are given by

$$P_\omega = 2\varepsilon_0 d(x, y, z) E^*(\omega) E(2\omega), \quad (2.50)$$

$$P_{2\omega} = \varepsilon_0 d(x, y, z) E^2(\omega), \quad (2.51)$$

where $d(x, y, z)$ is the spatial distribution of the nonlinear tensor. The factor 2 in Eqs. (2.47 — 2.50) arises from the multiplicity factor $M = 2$ for SFG/DFG and type II SHG process. In these processes, there are three distinct eigenmodes that differ in frequency or in polarization. For type 0 and type I SHG, there are only two distinct eigenmodes, as the fields at ω that have the same polarization and thus belong to the same waveguide mode hence $M = 1$.

SFG/DFG and type II SHG Processes

For SFG/DFG and type II SHG processes, we substitute Eqs. (2.47 — 2.49) for the polarization densities into Eq. (2.46) to get

$$\frac{dA_1}{dz} = -i\gamma_1 \frac{\varepsilon_0 \omega_1}{2} \int \int dx dy \tilde{\mathcal{E}}_1^* E_2^* E_3 e^{i\beta_1 z}, \quad (2.52)$$

$$\frac{dA_1}{dz} = -i\gamma_2 \frac{\varepsilon_0 \omega_2}{2} \int \int dx dy \tilde{\mathcal{E}}_2^* E_1^* E_3 e^{i\beta_2 z}, \quad (2.53)$$

$$\frac{dA_1}{dz} = -i\gamma_3 \frac{\varepsilon_0 \omega_3}{2} \int \int dx dy \tilde{\mathcal{E}}_3^* E_1 E_2 e^{i\beta_3 z}. \quad (2.54)$$

We define the field components E_i in terms of amplitude $A_i(z)$ and transverse profile $\tilde{\mathcal{E}}_i(x, y)$ such that

$$E_i(x, y, z) = \gamma_i A_i(z) \tilde{\mathcal{E}}_i(x, y) \exp(-i\beta_i z), \quad (2.55)$$

and the nonlinear tensor $d(x, y, z)$ as

$$d(x, y, z) = d_0 \hat{d}(x, y) g(z), \quad (2.56)$$

where $d_0 = \max |d|$ is the magnitude of the nonlinear coefficient, $|\hat{d}(x, y)| \leq 1$ is its normalised transversal distribution and $|g(z)| \leq 1$ is its profile along the propagation axis of the waveguide. Substituting in Eqs. (2.52 — 2.54), we get the following system

$$\frac{dA_1}{dz} = -i\kappa_1 \theta^* g(z) A_2^* A_3 e^{-i\Delta\beta z}, \quad (2.57)$$

$$\frac{dA_2}{dz} = -i\kappa_2 \theta^* g(z) A_1^* A_3 e^{-i\Delta\beta z}, \quad (2.58)$$

$$\frac{dA_3}{dz} = -i\kappa_3 \theta g(z) A_1 A_2 e^{i\Delta\beta z}, \quad (2.59)$$

where $\kappa_j = \sqrt{\frac{8\pi^2 d_0^2}{n_1 n_2 n_3 c \varepsilon_0 \lambda_j}}$ is the coupling coefficient for $j = 1, 2, 3$ and the field overlap θ is defined as

$$\theta = \int \int dx dy \hat{d}(x, y) \tilde{\mathcal{E}}_1(x, y) \tilde{\mathcal{E}}_2(x, y) \tilde{\mathcal{E}}_3^*(x, y). \quad (2.60)$$

The phase mismatch (or propagation vector mismatch) $\Delta\beta$ is defined as

$$\begin{aligned} \Delta\beta &= \beta_3 - \beta_2 - \beta_1, \\ &= 2\pi \left[\frac{n_3(\lambda_3)}{\lambda_3} - \frac{n_2(\lambda_2)}{\lambda_2} - \frac{n_1(\lambda_1)}{\lambda_1} \right]. \end{aligned} \quad (2.61)$$

In general, the phasemismatch is non-zero in which case what is called quasi-phasematching is employed. The waveguide is divided into different domains on which high voltage is applied periodically creating a grating with a period Λ adding an extra phase to $\Delta\beta$ that forces input fields to propagate in phase throughout the waveguide. Eq. (2.61) therefore reads

$$\Delta\beta = 2\pi \left[\frac{n_3(\lambda_3)}{\lambda_3} - \frac{n_2(\lambda_2)}{\lambda_2} - \frac{n_1(\lambda_1)}{\lambda_1} \right] + \frac{2\pi}{\Lambda}. \quad (2.62)$$

In practice, ultrashort pulses are not monochromatic therefore the wavenumber, β_i , of different bands $i = 1, 2, 3$ can be Taylor expanded with respect to frequency. The Taylor expansion of Eq. (2.62) then defines the group-velocity matching condition required for the quantum pulse gate [Red+13].

Type 0/I SHG Processes

The evolution of the fields in type 0/I SHG processes is deduced similarly by substituting Eqs. (2.50, 2.51) into Eq. 2.46 yielding the system

$$\frac{dA_\omega}{dz} = -i\kappa_\omega\theta^*g(z)A_\omega^*A_{2\omega}e^{-i\Delta\beta z}, \quad (2.63)$$

$$\frac{dA_{2\omega}}{dz} = -\frac{i}{2}\kappa_{2\omega}\theta g(z)A_{2\omega}^2e^{i\Delta\beta z}, \quad (2.64)$$

where $\kappa_j = \sqrt{\frac{8\pi^2d_0^2}{n_\omega^2n_{2\omega}c\epsilon_0\lambda_j^2}}$ is the coupling coefficient for $j = \omega, 2\omega$ and the field overlap θ is defined as

$$\theta = \int \int dx dy \hat{d}(x, y)\tilde{\mathcal{E}}_\omega^2(x, y)\tilde{\mathcal{E}}_{2\omega}^*(x, y). \quad (2.65)$$

It is worth noting that the above treatment for TWM processes has been derived for continuous wave (CW) fields. In case of ultrafast laser pulses, a treatment that takes into consideration the different propagation speeds of the pulse envelopes is necessary [CD03]. The analytical solutions of the systems (2.57 —2.59) and (2.63, 2.64) in the general case are quite complex [Boy08]. However, under certain approximations, simple solutions can be derived.

SFG under No-Pump Depletion Approximation (NPDA)

In the no-pump depletion approximation (NPDA), we consider the case of a strong classical pump field at ω_2 that is constant throughout the waveguide, that

is $dA_2/dz = 0$ and $A_2(z) = A_{\text{pump}} = \sqrt{I_{\text{pump}}}$. Under perfect phase matching with a weak field at ω_1 , the phase mismatch condition is $\Delta\beta = 0$ and we consider a uniform nonlinear crystal with a constant nonlinear profile $g(z) = 1$. Eqs. (2.57–2.59), therefore, reduce to

$$\frac{dA_1}{dz} = -i\kappa_1\theta^* A_{\text{pump}}^* A_3, \quad (2.66)$$

$$\frac{dA_3}{dz} = -i\kappa_3\theta A_1 A_{\text{pump}}. \quad (2.67)$$

Differentiate the first equation with respect to z and then substitute, we get

$$\frac{d^2 A_1}{dz^2} = \eta^{(\text{SFG})} I_{\text{pump}} A_3, \quad (2.68)$$

where

$$\eta^{(\text{SFG})} = \kappa_1\kappa_3|\theta|^2 = \frac{8\pi^2 d_0^2 |\theta|^2}{n_1 n_2 n_3 c \varepsilon_0 \lambda_1 \lambda_3}, \quad (2.69)$$

is the normalized conversion efficiency. For the initial boundary conditions $A_1(0) = \sqrt{I_1(0)}$ and $A_3(0) = 0$, the solutions to Eqs. (2.66, 2.67) are then

$$A_1(z) = A_1(0) \cos\left(\sqrt{\eta^{(\text{SFG})} I_{\text{pump}}} z\right), \quad (2.70)$$

$$A_3(z) = -iA_1(0) \sqrt{\frac{\lambda_1}{\lambda_3}} \frac{|\theta|}{\theta^*} \frac{|A_{\text{pump}}|}{A_{\text{pump}}^*} \sin\left(\sqrt{\eta^{(\text{SFG})} I_{\text{pump}}} z\right). \quad (2.71)$$

The factor λ_1/λ_3 ensures that solutions (2.70 and 2.71) satisfy energy conservation as imposed by Manley-Rowe relations [MR59; Boy08].

SHG is widely used in various applications, including frequency doubling of lasers to generate new wavelengths. For example, converting 1064 nm light from a Nd:YAG laser to 532 nm green light. SHG is utilized in optical parametric oscillators (OPOs) and amplifiers (OPAs) for generating tunable output frequencies. SHG microscopy is used for imaging structures without the need for fluorescent dyes, useful in biological and medical imaging. Not all materials exhibit significant $\chi^{(2)}$ nonlinearity. Non-centrosymmetric crystals, such as Lithium Niobate (LiNbO_3), Beta Barium Borate (BBO), and Potassium Titanyl Phosphate (KTP), are commonly used for SHG due to their strong $\chi^{(2)}$ susceptibilities. The absence of inversion symmetry in these crystals is a key requirement for second-order nonlinear processes.

SFG is used in a variety of applications. For instance SFG spectroscopy is a powerful tool for investigating surface and interface properties, as the SFG signal is inherently surface-specific due to the non-centrosymmetry requirement at interfaces. SFG can be used to for frequency up-conversion to generate light at new frequencies, particularly in the ultraviolet (UV) range, which is useful for applications requiring high-energy photons. Optical signal processing is another example that uses SFG can for mixing signals in optical communication systems, enabling wavelength conversion and the generation of new optical frequencies for data transmission. On the other hand, DFG is utilized in various applications, including infrared (IR) generation from two lasers operating at different frequencies, where direct sources might not be available or practical. Optical parametric oscillators (OPOs) depends on DFG where it is used to generate tunable output across a wide range of frequencies by varying the frequencies of the input waves. DFG enables the generation of coherent light in spectral regions that are difficult to access with conventional lasers, facilitating advanced spectroscopic techniques.

2.5 Temporal-Mode Transformations

TMT refers to the coherent manipulation of a wave form in the TM basis, which maps the input TM $A(\omega')$ into the output TM $C(\omega)$ through

$$\text{TMT} : A(\omega') \mapsto C(\omega) = \int d\omega' G(\omega, \omega') A(\omega'), \quad (2.72)$$

where $G(\omega, \omega')$ is the Green transfer map of the TMT. We classify TMTs into two categories, namely, intraband and interband TMTs. Intraband transformations occur when the input and output modes fall within the same spectral region, that is $\nu = |\omega - \omega'| \ll \omega$. On the other hand, interband transformations occur when the input and output modes fall in two different spectral regions. In other words, the TMT maps the TM into another TM with frequency conversion attached to the transformation map. Therefore, Eq. (2.72) can be generalized for any number of TMs and spectral regions.

For the sake of completeness, since TMs are modes that can be populated by arbitrary states of light (classical or quantum mechanical), we can write a TMT map, analogous to Eq. (2.72), for a quantum mechanical state. For example, for a single-photon state $|\psi\rangle$ defined as in Eq. (2.31), we can define the map

$$\text{TMT} : A^\dagger|vac\rangle \mapsto C^\dagger|vac\rangle = \exp\left(\mathcal{C} \int d\omega d\omega' G(\omega, \omega') \hat{a}(\omega') \hat{c}^\dagger(\omega)\right) |vac\rangle, \quad (2.73)$$

where \mathcal{C} measures the strength of the transformation.

In the present thesis, we focus our investigation on intraband TMTs in the infrared (IR) spectral region and interband TMTs between IR and blue spectral regions. Therefore, I introduce the subscript "r" for IR and "b" for blue. Eq. (2.72) thus changes for intraband and interband TMTs respectively as

$$C(\omega_r) = \int d\omega'_r G_{rr}(\omega_r, \omega'_r) A(\omega'_r), \quad (2.74)$$

$$D(\omega_b) = \int d\omega'_r G_{br}(\omega_b, \omega'_r) A(\omega'_r), \quad (2.75)$$

where the primes are added to designate input frequencies.

2.6 Quantum Pulse Gate

TMTs can be physically realized in second-order $\chi^{(2)}$ nonlinear media, utilizing frequency conversion (FC) [Kum90]. One intuitive approach to understand frequency conversion is by imagining a rapidly moving mirror or a beam splitter: light reflected from the beam splitter's front undergoes a blue shift, whereas light from its rear experiences a red shift [Ray+10]. With equal yet opposite frequency shifts, and assuming 100% reflectivity, the colors characterizing the modes undergo an interchange. Such frequency conversion does not alter the nature of the state populating the modes undergoing interchange.

A quantum pulse gate (QPG) is a device that multiplexes and demultiplexes TMs based on sum frequency generation (SFG) [EBS11]. As shown in Fig. (2.2), a multi-mode weak input light pulse co-propagates with a classical single-mode pulse (gating pulse) in a second-order nonlinear medium, in which the pump and signal fields propagate with nearly the same group velocity, in order to extract photons in a well-defined TM whose shape matches that of the gating pulse. Therefore, shaping the gating pulse is used to convert modes from an arbitrary input state with efficiency close to unity. In fact, the unitary QPG operation is completely defined by the bright pump and the waveguide dispersion.

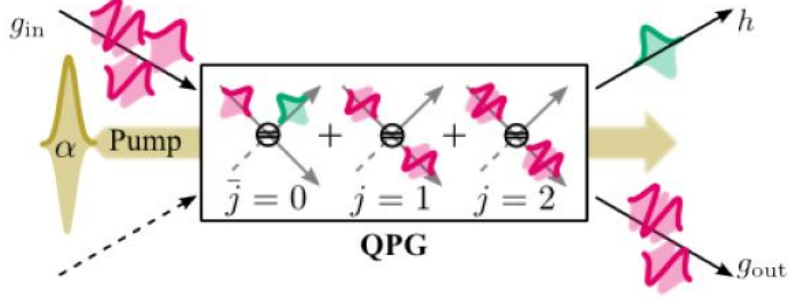


Figure 2.2. Schematic depiction of a quantum pulse gate operation (From [Bre14]).

Silberhorn group [EBS11; Bre+11] first proposed implementing the QPG based on three-wave mixing in a type-II periodically-poled Lithium Niobate (PPLN) waveguide with a gating pulse at 870nm and an input signal at 1550nm and the upconverted pulse at 557nm. That was experimentally demonstrated for weak coherent states [Bre+14; Ans+18a] as well as quantum light [Ans+18b]. Around the same time, the Raymer group developed a theoretical framework of QPGs [Red+13; RRM15; RR17] and demonstrated a QPG in a type-0 periodically-poled Lithium Niobate (PPLN) waveguide with a gating pulse at 821nm and an input signal at 812nm and the upconverted pulse at 408nm with high conversion efficiency through an interferometric scheme [RR18]. It is worth mentioning that the latter QPG is not a good fit for single-photon wave packets due to noise constraints.

The theory of QPGs is based on frequency conversion in three-wave mixing in nonlinear optical materials. Detailed account of the theory of the QPG can be found in [Red+13; RRM15; RR17; Bre14]. We limit our interest to sum and difference frequency generation processes based on three-wave mixing in a medium with a second-order nonlinearity, $\chi^{(2)}$, as shown in Fig. (2.3). It should be noted that the formal treatment of parametric down-conversion is similar to that of quantum pulse gate.

For a bright classical gating pulse, the effective interaction Hamiltonian of SFG that creates a photon with the SFG frequency ω_b and annihilates a photon with signal frequency ω_r is given by [EBS11; Red+13]

$$\hat{H}_{\text{eff}}^{(\text{FC})} = \theta \int \int d\omega_r d\omega_b G_{br}(\omega_b, \omega_r) \hat{a}(\omega_r) \hat{c}^\dagger(\omega_b) + h.c., \quad (2.76)$$

where $\theta \propto \chi^{(2)} \sqrt{P}$ is the mode-coupling strength that depends on the medium non-

linearity, $\chi^{(2)}$, and the gating pulse power, P . The transfer function $G_{br}(\omega_b, \omega_r) = \alpha(\omega_b - \omega_r) \times f(\omega_b, \omega_r)$ maps the signal frequencies ω_r to the sum frequencies ω_b , where $\alpha(\omega_b - \omega_r)$ is the spectral amplitude of the pump pulse and $f(\omega_r, \omega_b)$ is the phase-matching function which depends on the dispersive properties of the medium.

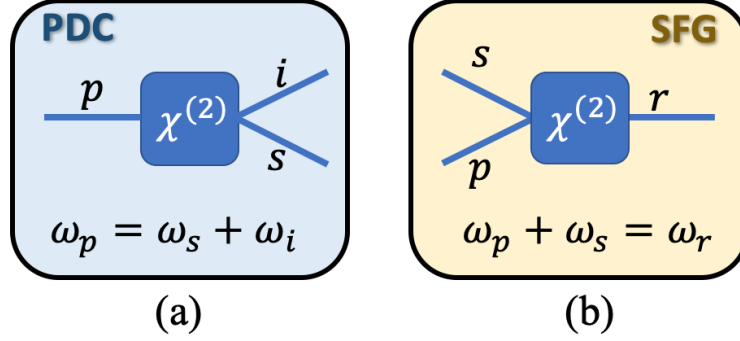


Figure 2.3. Schemes showing frequency conversion in parametric down-conversion (a) and quantum pulse gating (b).

In general, the transfer function $G_{br}(\omega_b, \omega_r)$ is not separable, that is we can not write $G_{br}(\omega_b, \omega_r) \neq g(\omega_b)f(\omega_r)$ as the product of two independent functions. However, the transfer function can be represented using Schmidt decomposition [Ray10; EBS11; Red+13]

$$G_{br}(\omega_b, \omega_r) = \sum_j \lambda_j \Psi_j(\omega_b) \phi_j(\omega_r), \quad (2.77)$$

where ϕ_j (Ψ_j) are the signal (register) *Schmidt modes* with Schmidt coefficients λ_j such that $\sum_j \lambda_j^2 = 1$. In the Schmidt decomposition, the set of Schmidt coefficients $\{\lambda_j\}$ are ordered in decreasing magnitude, such that $\lambda_0 \geq \lambda_1 \geq \lambda_3 \dots$. It is worth mentioning that Eq. (2.77) is the frequency-domain equivalent of Eqs. (4) in [Red+13]. Substituting Eq. (2.27) with its complex conjugate and Eq. (2.77) into Eq. (2.76) yields

$$\hat{H}_{\text{eff}}^{(\text{FC})} = \theta \sum_j \lambda_j (\hat{A}_j \hat{C}_j^\dagger + \hat{A}_j^\dagger \hat{C}_j). \quad (2.78)$$

Since $\hat{H} = \theta \hat{a} \hat{c}^\dagger + h.c.$ is the form of the Hamiltonian of an optical beam splitter [PSM87], Eq. (2.78) shows that a QPG can be formally interpreted as a set of

beam splitters independently operating on TMs as depicted in Fig. (2.2). In other words, a QPG action can be defined as

$$QPG : \hat{A}_j \rightarrow \cos(\theta_j)\hat{A}_j + i \sin(\theta_j)\hat{C}_j, \quad (2.79)$$

where $\theta_j = \theta\lambda_j$ is the effective coupling constant.

TMT Green's functions and Schmidt Decomposition

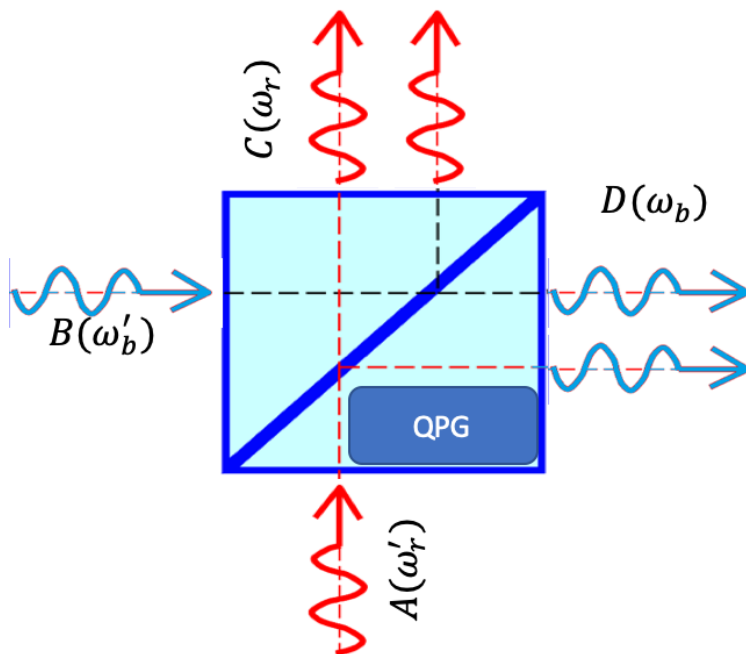


Figure 2.4. A schematic depiction of a TMT as a beam-splitter-like transformation for TMs. Part of mode $A(\omega'_r)$ in the red band gets transmitted into $C(\omega_r)$ and the other part gets "converted" into $D(\omega_b)$ in the blue band. Same and opposite transformation applies for $B(\omega'_b)$.

An approach of representing QPGs is to adopt the Green's function formalism. A QPG can act like a beam splitter for TMs where frequency conversion is equivalent to reflection in ordinary beam splitters. Fig. 2.4 depicts a TMT for temporal modes in which the two input ports of the QPG are occupied by the two input modes $A(\omega'_r)$ and $B(\omega'_b)$ in the "red" and "blue" frequency bands respectively. The output ports are occupied by the two modes $C(\omega_r)$ and $D(\omega_b)$ which are related to the input modes through the general transformation [Ray+10]

$$\begin{aligned}
C(\omega_r) &= \int d\omega'_r G_{rr}(\omega_r, \omega'_r) A(\omega'_r) + \int d\omega'_b G_{rb}(\omega_r, \omega'_b) B(\omega'_b), \\
D(\omega_b) &= \int d\omega'_r G_{br}(\omega_b, \omega'_r) A(\omega'_r) + \int d\omega'_b G_{bb}(\omega_b, \omega'_b) B(\omega'_b).
\end{aligned} \tag{2.80}$$

The Green's functions G_{ij} are the elements of such unitary transformation that obeys the unitarity condition

$$\begin{aligned}
&\int d\omega'_i G_{ii}(\omega_1, \omega'_i) G_{ii}^*(\omega_2, \omega'_i) \\
&+ \int d\omega'_j G_{ij}(\omega_1, \omega'_j) G_{ij}^*(\omega_2, \omega'_j) = \delta(\omega_1 - \omega_2),
\end{aligned} \tag{2.81}$$

for $i \neq j$. Performing singular-value decomposition (SVD), also known as Schmidt decomposition, of each of the Green's functions that describe the TMT we get the following relationships [Ray+10]

$$\begin{aligned}
G_{rr}(\omega_r, \omega'_r) &= \sum_n \tau_n \Phi_n(\omega_r) \phi_n(\omega'_r), \\
G_{bb}(\omega_b, \omega'_b) &= \sum_n \tau_n \Psi_n(\omega_b) \psi_n(\omega'_b), \\
G_{rb}(\omega_r, \omega'_b) &= - \sum_n \rho_n \Phi_n(\omega_r) \psi_n(\omega'_b), \\
G_{br}(\omega_b, \omega'_r) &= \sum_n \rho_n \Psi_n(\omega_b) \phi_n(\omega'_r),
\end{aligned} \tag{2.82}$$

where $\phi_n(\omega'_r)$ and $\psi_n(\omega'_b)$ are the two input Schmidt modes while $\Phi_n(\omega_r)$ and $\Psi_n(\omega_b)$ are the two output Schmidt modes in the red and blue frequency bands respectively. The coefficients τ_n represent the transmission of "intra-band" Schmidt modes while the coefficients ρ_n represent the frequency conversion of "inter-band" Schmidt modes. For instance, $G_{rr}(\omega_r, \omega'_r)$ maps/transfers the input Schmidt mode $\phi_n(\omega'_r)$ in the red band into the output Schmidt mode $\Phi_n(\omega_r)$ in the red band with transmission probability τ_n^2 . On the other hand, $G_{br}(\omega_b, \omega'_r)$ maps the input Schmidt mode $\phi_n(\omega'_r)$ in the red band into the output Schmidt mode $\Psi_n(\omega_b)$ in the blue band with conversion ρ_n^2 . We should note that only a set of four Schmidt modes is sufficient to describe the TMT instead of eight.

Conversion Efficiency and Selectivity

The equivalence between the QPG and the beam splitter represented in Eq. (2.78) gives a straightforward intuition of two figures of merit that can be used to

characterize the QPG. Conversion efficiency (CE) is defined as the probability of converting a photon in mode \hat{A}_j to an up-converted photon in mode \hat{C}_j , that is

$$\eta_j = \sin^2(\theta_j), \quad (2.83)$$

where $\theta_j = \theta\lambda_j$. Mode discrimination (MD) can be defined as the probability of conversion efficiency of the leading mode, $j = 0$, with respect to conversion efficiencies of all modes and is expressed as [Red+13]

$$MD \equiv \frac{\sin^2(\theta_0)}{\sum_j \sin^2(\theta_j)} \leq 1. \quad (2.84)$$

Another figure of merit is selectivity, S , that is defined as the product of CE and MD for the leading mode such that

$$S = \frac{\sin^4(\theta_0)}{\sum_j \sin^2(\theta_j)}. \quad (2.85)$$

Selectivity describes the ability to discriminate between different orders of Schmidt modes of the Schmidt decomposition of the transfer kernel $G(\omega, \omega')$. A selectivity value of 1 denotes an ideal operation limited to a single temporal mode, while a value of 0 indicates a complete lack of discrimination between different modes. Figs. 2.5 show different Green transfer maps $G_{rr}(\omega_r, \omega'_r)$ for an ideal QPG with selectivity ~ 1 in (a) and for realistic QPG with selectivity ~ 0.5 in (b) and ~ 0.25 in (c) respectively.

No-Pump Representation of QPGs

Considering the case of the IR Green transfer map $G_{rr}(\omega_r, \omega'_r)$, we can rewrite its Schmidt decomposition as follows

$$\begin{aligned} G_{rr}(\omega_r, \omega'_r) &= \sum_n \tau_n \Phi_n(\omega_r) \phi_n(\omega'_r), \\ &= \sum_n \Phi_n(\omega_r) \phi_n(\omega'_r) - \sum_n \Phi_n(\omega_r) \phi_n(\omega'_r) + \sum_n \tau_n \Phi_n(\omega_r) \phi_n(\omega'_r), \\ &= \delta(\omega_r, \omega'_r) - \sum_n (1 - \tau_n) \Phi_n(\omega_r) \phi_n(\omega'_r), \\ &= \delta(\omega_r, \omega'_r) + \tilde{G}_{rr}(\omega_r, \omega'_r), \end{aligned} \quad (2.86)$$

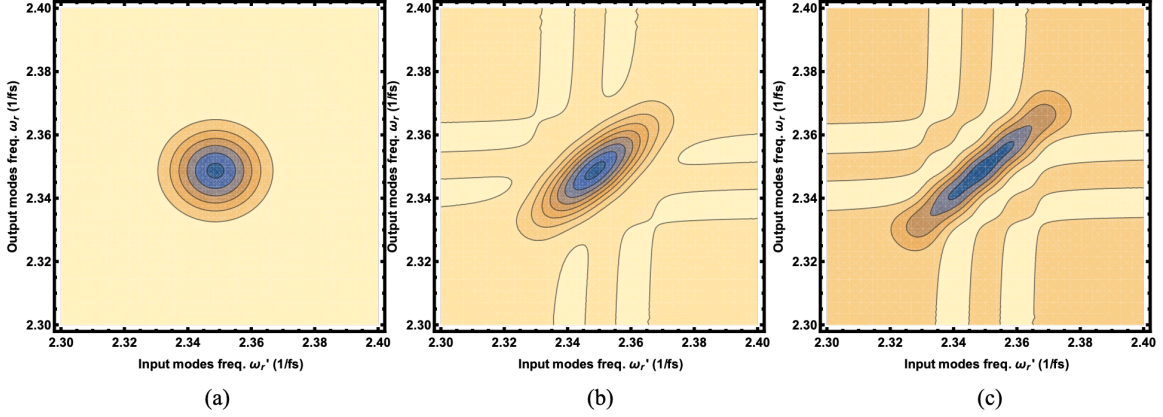


Figure 2.5. Green transfer map $G_{rr}(\omega_r, \omega_r')$ for an ideal QPG with selectivity ~ 1 (a), for a realistic QPG with selectivity ~ 0.5 (b) and for a realistic QPG with selectivity ~ 0.25 (c).

where we call $\tilde{G}_{rr}(\omega_r, \omega_r') = -\sum_n \lambda_n \Phi_n(\omega_r) \phi_n(\omega_r')$ the filtered Green transfer map whose Schmidt coefficients $\lambda_n = 1 - \tau_n$. We used the completeness relation of the Schmidt modes, $\delta(\omega_r, \omega_r') = \sum_n \Phi_n(\omega_r) \phi_n(\omega_r')$. Therefore, the representation of the filtered Green transfer map $\tilde{G}_{rr}(\omega_r, \omega_r')$ is given as

$$\tilde{G}_{rr}(\omega_r, \omega_r') = G_{rr}(\omega_r, \omega_r') - \delta(\omega_r, \omega_r'). \quad (2.87)$$

We call Eq. (2.87) as the no-pump correction representation of the QPG transfer function. It should be pointed out that both \tilde{G} and G are equivalent but not equal. It is worth mentioning that the Dirac delta term $\delta(\omega_r, \omega_r')$ is the identity transformation which represents the no-pump case where the input pulse undergoes *no* transformation and we can say that the input and output modes are identical. This follows from the fact that $\tau_n \rightarrow 1$ (transmission of all modes goes to one, none are converted) and the filtered $\tilde{G}(\omega_r, \omega_r') \rightarrow 0$. As the pump power increases, transmission τ_n decreases which leads to greater effect of the QPG. Hence, the action of the QPG is encapsulated in $\tilde{G}(\omega_r, \omega_r')$.

An illustration of Eq. 2.87 is shown in Fig. 2.6 where the first and second terms of the R.H.S. are shown in (a) and (b) respectively and the L.H.S. is illustrated in (c).

For the sake of clarity and consistency, all plots of the Green transfer map, whether unfiltered or filtered, will be of the absolute value for the rest of the thesis.

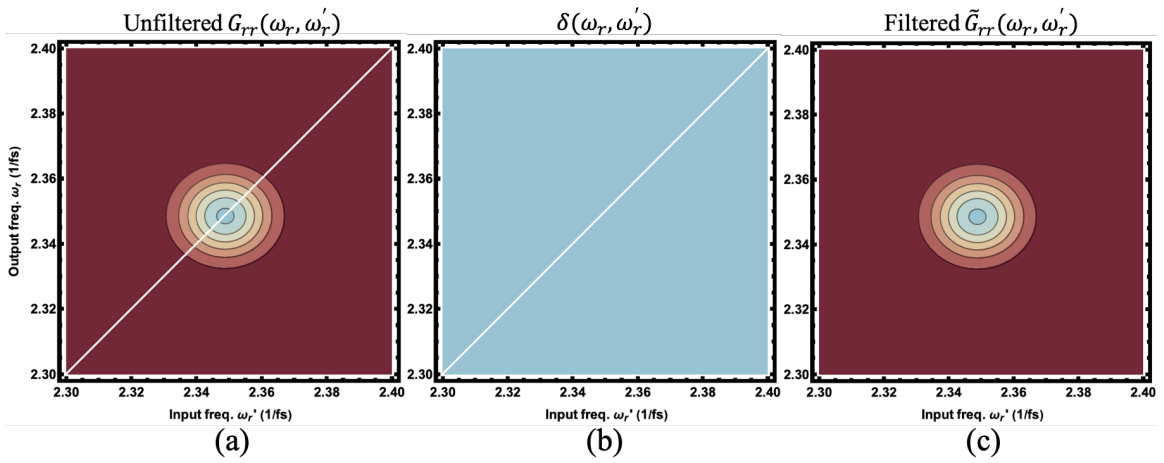


Figure 2.6. Filtering representation Eq. (2.87) that shows the unfiltered $G_{rr}(\omega_r, \omega'_r)$ (a), the no-pump Dirac delta (b) which is represented by the diagonal white line and the filtered $\tilde{G}_{rr}(\omega_r, \omega'_r)$ (c).

CHAPTER 3

CHARACTERIZATION OF TEMPORAL-MODE TRANSFORMATIONS

Spectral interferometry is a versatile technique widely used in optics and photonics research for characterizing the temporal and spectral characteristics of electromagnetic fields. It provides valuable insights into the temporal coherence, spectral phase, and amplitude of optical pulses, making it an indispensable tool in various scientific and engineering disciplines. The principle of spectral interferometry dates back to the early 20th century when Michelson developed the Michelson interferometer, which paved the way for the measurement of optical interference phenomena [Mic81]. Building upon Michelson's work, Hanbury Brown and Twiss introduced intensity interferometry, which played a crucial role in the study of stellar sources and the development of quantum optics [HT56].

In the context of spectral interferometry, the development of Fourier transform spectroscopy (FTS) by Fellgett and Jacquinot revolutionized the field by enabling high-resolution spectroscopic measurements using interferometric techniques [FJ55]. FTS provides a powerful tool for analyzing the spectral content of optical signals and has found widespread applications in fields ranging from astronomy to molecular spectroscopy.

Over the years, significant advancements have been made in experimental techniques for spectral interferometry. Pioneering work by Dorrer and Kang in the late 1990s demonstrated the use of spectral interferometry for characterizing ultrashort optical pulses with femtosecond durations [DK98]. Their work laid the foundation for ultrafast spectroscopy techniques based on spectral interferometry, enabling the study of ultrafast dynamics in materials and molecules with unprecedented temporal resolution.

Spectral interferometry finds applications in a wide range of scientific and engineering fields. In ultrafast science, spectral interferometry is used for pulse characterization, and the study of ultrafast phenomena such as laser-induced dynamics and photochemical reactions [Tre97]. In quantum optics, spectral interferometry plays a crucial role in the characterization of quantum states of light, enabling applications in quantum communication, quantum information processing, and quantum metrology [LR09].

The present chapter starts by giving an overview of the general technique of spectral interferometry in Section 3.1 in order to lay the foundations of our pro-

posed method that characterizes temporal-mode transformations which is laid out in Section 3.2. We discuss different classes of CTMT-SI particularly in linear and quadratic phase shifters in addition to some of the technical issues that arise in realistic experiments.

3.1 Spectral Interferometry

The principal idea of spectral interferometry is to characterize the spectral phase $\phi(\omega)$ of ultrashort pulses. As discussed in Chapter 2, an optical pulse is described by an envelope function and a phase, $\alpha(t)e^{i\psi(t)}$. This holds in the frequency domain such that the pulse is described by $A(\omega)e^{i\phi(\omega)}$. However, note that $\alpha(t)$ and $A(\omega)$ are not Fourier transform pairs.

The setup in Fig. 3.1 shows a schematic of how an unknown spectral phase $\phi(\omega)$ can be characterized by splitting a pulse, $A(\omega)e^{-i\omega t}$ coming from a well characterized laser source, by a beam splitter into two interferometer arms. The first arm (top) has the unknown phase component $\phi(\omega)$, to be characterized, picked up by the pulse to become $A(\omega)e^{-i\omega t + \phi(\omega)}$. The reference arm (bottom) picks up a fixed time delay, τ , that can not be greater than $1/\Delta\nu$, where $\Delta\nu$ is the spectral resolution of the spectrometer. The interference pattern will have fringe spacing in the spectral domain of the order $1/\tau$. The two fields are interfered at a BS and the spectrum at the output, $\tilde{S}(\omega)$, is measured on a spectrometer (see Fig. 3.2) and can be expressed as

$$\begin{aligned}\tilde{S}(\omega) &= \left| \frac{1}{2} \int dt [A(\omega)e^{-i\omega\tau} + A(\omega)e^{i\phi(\omega)}] e^{-i\omega t} \right|^2, \\ &= \frac{1}{4} |A(\omega)|^2 \left| \{1 + \cos[\omega\tau + \phi(\omega)]\} \right|^2, \\ &= \tilde{S}_{\text{DC}}(\omega) + \tilde{S}_{\text{AC}}^{(-)}(\omega)e^{i\omega\tau} + \tilde{S}_{\text{AC}}^{(+)}(\omega)e^{-i\omega\tau},\end{aligned}\tag{3.1}$$

where $\tilde{S}_{\text{DC}}(\omega) = |A(\omega)|^2/4$ is the DC component and $\tilde{S}_{\text{AC}}^{(+)}(\omega) = |A(\omega)|^2 e^{i\omega\tau} e^{i\phi(\omega)}$ is the well separated positive frequency AC signal and $\tilde{S}_{\text{AC}}^{(-)}(\omega) = [\tilde{S}_{\text{AC}}^{(+)}(\omega)]^*$ is the negative frequency AC signal.

To extract the phase, $\phi(\omega)$, we apply the inverse Fourier transform over ω the time domain (see Fig. 3.3) showing both positive and negative AC signals as sidebands displaced in time by the time delay τ

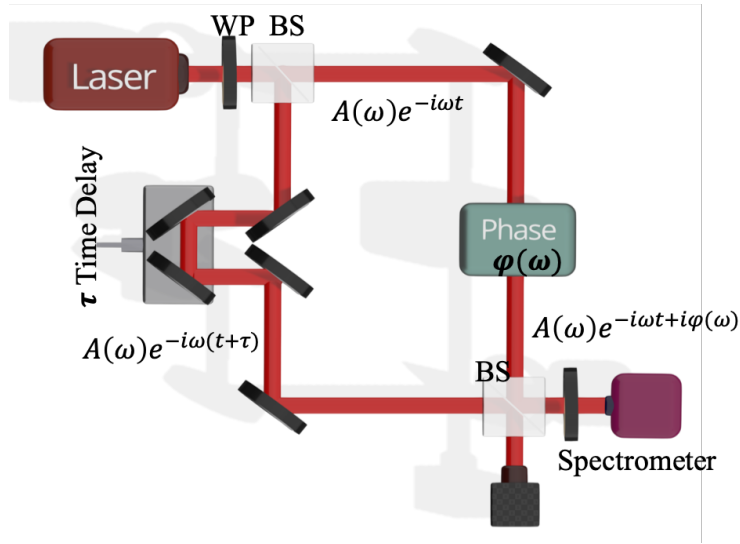


Figure 3.1. Schematic setup of a Mach-Zehnder interferometer to characterize amplitude and phase of an ultrashort pulse. A pulse $A(\omega)e^{i\omega t}$ from a laser source is split by a beam splitter (BS) into a top arm that picks up a phase $\phi(t)$ to be characterized and a reference arm (bottom) that picks up a time delay τ . The two-arms pulses $A(\omega)e^{i\omega t+\phi(\omega)}$ and $A(\omega)e^{i\omega(t-\tau)}$ interfere and their spectral interferogram is measured by a spectrometer. WP stands for waveplate and BS stands for beam splitter.

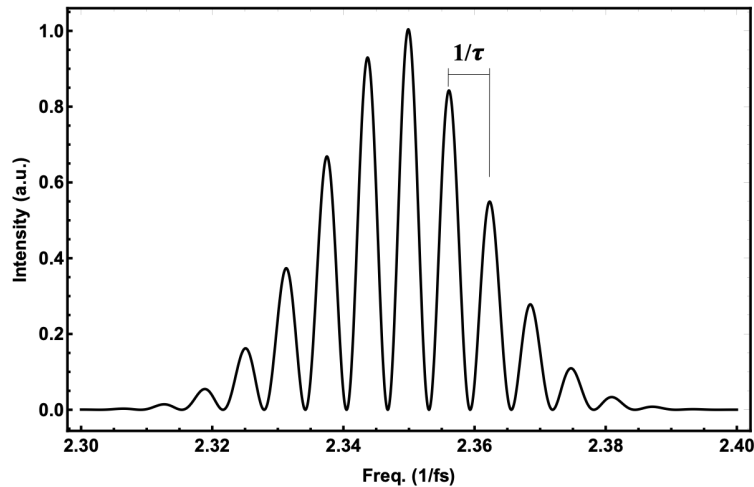


Figure 3.2. Spectrum in the frequency domain that would be measured on a spectrometer due to the interference of two pulses.

$$\begin{aligned}
S(t) &= \frac{1}{\sqrt{2\pi}} \int d\omega \tilde{S} e^{i\omega t}, \\
&= S_{\text{DC}}(t) + S_{\text{AC}}^{(-)}(t - \tau) + S_{\text{AC}}^{(+)}(t + \tau),
\end{aligned} \tag{3.2}$$

where we use the conventional $1/\sqrt{2\pi}$ factor for Fourier transforms.

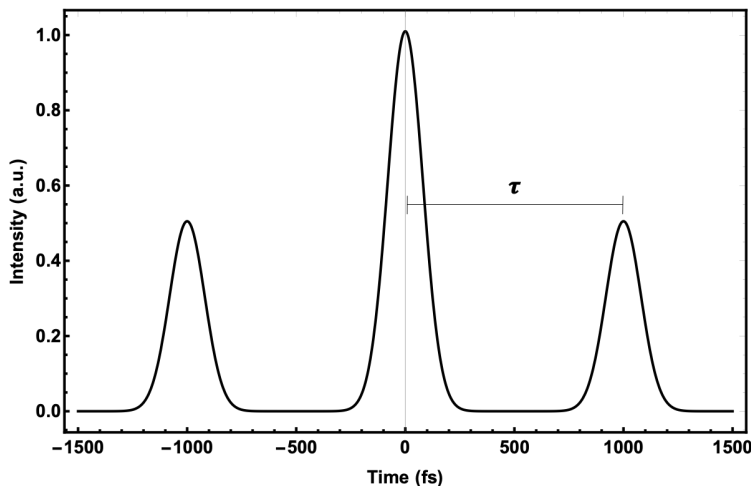


Figure 3.3. Spectrum in the time domain when the inverse Fourier transform is applied on $\tilde{S}(\omega)$.

By filtering out the DC component along with one of the sidebands and then Fourier transform back to the frequency domain, we are able to extract the phase $\phi(\omega)$ such that

$$\phi(\omega) = \arg \left[\tilde{S}_{\text{AC}}^{(+)}(\omega) \right]. \tag{3.3}$$

3.2 Characterization of the Transfer Map $G(\omega, \omega')$

Now that we have discussed the mathematical framework of temporal modes and temporal mode transformations, I introduce a method for characterizing TMTs based upon spectral interferometry (CTMT-SI). In general, TMTs are divided into two classes as shown in Fig. 3.4 based on whether there is frequency conversion or not. In the context of optics, the first class represents intraband TMTs that describe linear optics systems, e.g., phase shifters, lenses, ordinary beam splitters,

waveplates, and many other common components. On the other hand, the second class describes interband TMTs of nonlinear optics systems where there is energy and/or momentum exchange, e.g., frequency mixing, optical Kerr effect, cross-phase modulation, and Raman amplification to mention a few examples.

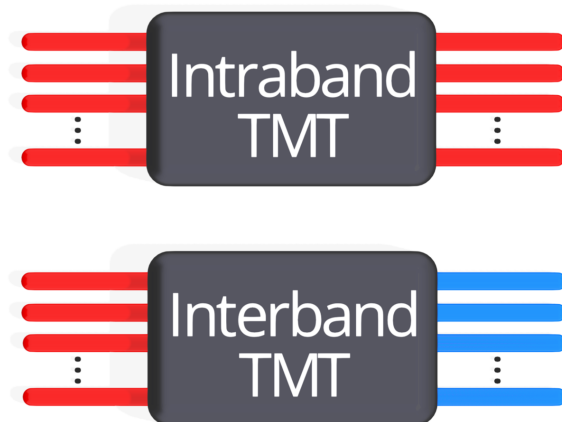


Figure 3.4. Schematic diagram of TMTs that describe intraband transformations where there is no frequency conversion and interband transformations where there is frequency conversion.

The general concept for the proposed CTMT-SI is depicted in Fig. 3.5. A short optical pulse is split at a beam splitter to generate a probe pulse, described in the frequency domain by $A(\omega)$, and a replica as a reference pulse. The reference pulse is time delayed by a fixed time τ and the reference pulse becomes $A(\omega, \tau) = A(\omega)e^{-i\omega\tau}$. The probe pulse is sent to a tunable delay, T , that adds a spectral phase factor to the probe pulse $A(\omega, T) = A(\omega)e^{-i\omega T}$. The temporal duration of the probe pulse is much shorter than the range over which T is scanned. The time-shifted probe is sent through the TMT resulting in an output temporal mode

$$C(\omega, T) = \int d\omega' G(\omega, \omega') A(\omega') e^{-i\omega' T}, \quad (3.4)$$

where $G(\omega, \omega')$ is the map of the TMT under investigation which transforms the probe $A(\omega, T) = A(\omega)e^{-i\omega T}$ into the output $C(\omega, T)$ which is interfered with the reference pulse, $A(\omega)e^{-i\omega\tau}$ that has a delay τ , on a beam splitter. One output of the beam splitter is monitored with a spectrometer giving a spectrum $S(\omega, T) = I_A(\omega) + I_C(\omega) + 2\text{Re}\{A(\omega, \tau)C^*(\omega, T)\}$. The interference between $C(\omega, T)$ and $A(\omega, T)$ gives rise to spectral interferograms with changing visibility and spacing

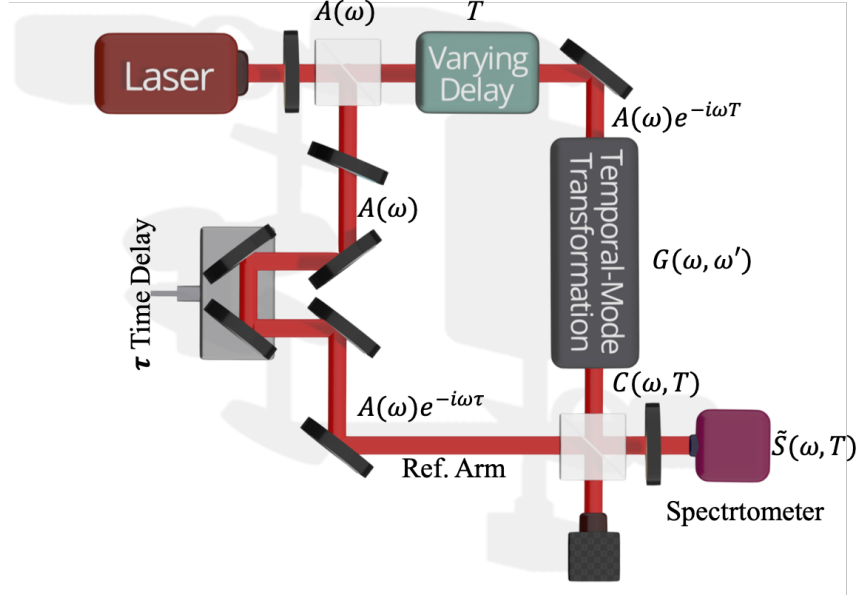


Figure 3.5. Schematic setup of interferometric process tomography. A short optical pulse out of a Ti-Saph laser at central wavelength $\lambda_0 = 810\text{nm}$ and bandwidth of $\Delta\lambda = 8\text{nm}$ is split at a beam splitter to generate a probe pulse $A(\omega)$ at central wavelength $\lambda_0 = 805\text{nm}$ and bandwidth of $\Delta\lambda = 5\text{nm}$ and a replica as a reference pulse. The probe pulse is sent to a tunable delay, T , then undergoes a TMT. The interference between the output $C(\omega, T)$ and the reference is measured at one output of the second beam splitter.

between fringes that depends on time delays T and τ , and the action of the map $G(\omega, \omega')$ on $A(\omega, T)$. In order to determine the transfer map $G(\omega, \omega')$, we use SI tools of Fourier analysis. The spectral interferograms between $C(\omega, T)$ and $A(\omega, \tau)$ are expressed as

$$\begin{aligned}
 S(\omega, T) &= \frac{1}{2} [s_{\text{DC}}(\omega, T) + s_{AC}^{(-)}(\omega, T) + s_{AC}^{(+)}(\omega, T)], \\
 &= \frac{1}{2} \left[|A(\omega)|^2 + |C(\omega, T)|^2 + A(\omega)C^*(\omega, T)e^{-i\omega\tau} \right. \\
 &\quad \left. + A^*(\omega)C(\omega, T)e^{+i\omega\tau} \right], \tag{3.5}
 \end{aligned}$$

where the first line of Eq. (3.5) represents the DC ($\omega = 0$) component and the second and third lines represent the positive and negative AC ($\omega = \pm 2\pi/(\tau - T)$) components and τ is a fixed time delay. Since T is varying, the AC peaks move along

the time axis in the time domain causing the two sidebands to be slanted as shown in Fig. 3.7b. To extract the map $G(\omega, \omega')$, we can implement the following algorithm. We apply a Fourier transform to the measured spectra $S(\omega, T)$ with respect to ω ($\omega \Rightarrow t$), such that

$$\begin{aligned}
\tilde{S}(t, T) &= \frac{1}{\sqrt{2\pi}} \int d\omega S(\omega, T) e^{i\omega t}, \\
&= \frac{1}{2\sqrt{2\pi}} \int d\omega [|A(\omega, T)|^2 + |C(\omega, T)|^2] e^{i\omega t} \\
&\quad + \frac{1}{2\sqrt{2\pi}} \int d\omega \int d\omega' A(\omega) G^*(\omega, \omega') A^*(\omega') e^{i\omega[t-(\tau+T)]} e^{i\omega'T} \\
&\quad + \frac{1}{2\sqrt{2\pi}} \int d\omega \int d\omega' A^*(\omega) G(\omega, \omega') A(\omega') e^{i\omega[t+(\tau+T)]} e^{-i\omega'T}. \tag{3.6}
\end{aligned}$$

where the tilde $\tilde{\cdot}$ denotes the Fourier transform. The first line of Eq. (3.6) is the DC component at $\tau = 0$, while the second line is the negative AC component at $-(\tau + T)$ and the third line is the positive AC component at $+(\tau + T)$. We filter out the DC and negative AC components by multiplying by a 2D super Gaussian filtering function that takes the form $e^{-(x-x_0)^4/\delta x^4} e^{-(y-y_0)^4/\delta y^4}$. We then get the positive AC component at $t = \tau + T$,

$$\begin{aligned}
\tilde{S}^{(+)}(t, T) &= \frac{1}{2\sqrt{2\pi}} \int \int d\omega d\omega' A^*(\omega) G(\omega, \omega') A(\omega') \\
&\quad \times e^{iT(\omega-\omega')} e^{i\omega(t+\tau)}, \tag{3.7}
\end{aligned}$$

Fourier transform Eq. (3.7) to the frequency domain $t \Rightarrow \omega$, such that

$$\begin{aligned}
\tilde{S}^{(+)}(\omega, T) &= \frac{1}{\sqrt{2\pi}} \int dt \tilde{S}^{(+)}(t, T) e^{-i\omega t}, \\
&= \frac{1}{2} \int \int d\omega' d\omega'' \left[\int \frac{dt}{2\pi} e^{it(\omega''-\omega)} \right] \\
&\quad \times A^*(\omega'') G(\omega'', \omega') A(\omega') e^{iT(\omega''-\omega')} e^{-i\omega''\tau} \\
&= \frac{1}{2} \int \int d\omega' d\omega'' \delta(\omega'' - \omega) A^*(\omega'') G(\omega'', \omega') A(\omega') e^{iT(\omega''-\omega')} e^{-i\omega''\tau} \\
&= \frac{1}{2} \int d\omega' A^*(\omega) G(\omega, \omega') A(\omega') e^{iT(\omega-\omega')} e^{-i\omega\tau}, \tag{3.8}
\end{aligned}$$

Applying an inverse Fourier transform with respect to time $T \Rightarrow \nu$, we obtain

$$\tilde{S}^{(+)}(\omega, \nu) = \frac{1}{\sqrt{2\pi}} \int dT \tilde{S}^{(+)}(\omega, T) e^{-i\nu T},$$

$$\begin{aligned}
&= \frac{1}{2\sqrt{2\pi}} \int dT \int d\omega' A^*(\omega)G(\omega, \omega')A(\omega')e^{-i\omega\tau}e^{i(\omega-\omega')T}e^{-i\nu T}, \\
&= \sqrt{\frac{\pi}{2}} \int d\omega' \left[\frac{1}{2\pi} \int dT e^{iT[(\omega-\nu)-\omega']} \right] A^*(\omega)G(\omega, \omega')A(\omega')e^{-i\omega\tau}, \\
&= \sqrt{\frac{\pi}{2}} \int d\omega' \delta[(\omega' + \nu) - \omega] A(\omega)G^*(\omega, \omega')A^*(\omega')e^{-i\omega\tau}, \\
&= \sqrt{\frac{\pi}{2}} A^*(\omega)G(\omega, \omega - \nu)A(\omega - \nu)e^{-i\omega\tau}. \tag{3.9}
\end{aligned}$$

The reconstructed transfer map is obtained as

$$G(\omega, \omega') = \sqrt{\frac{2}{\pi}} \frac{\tilde{S}^{(+)}(\omega, \nu)e^{i\omega\tau}}{A^*(\omega)A(\omega')}, \tag{3.10}$$

where $\nu = \omega - \omega'$ is the variation between input and output frequency degrees of freedom due to the action of the transfer map G .

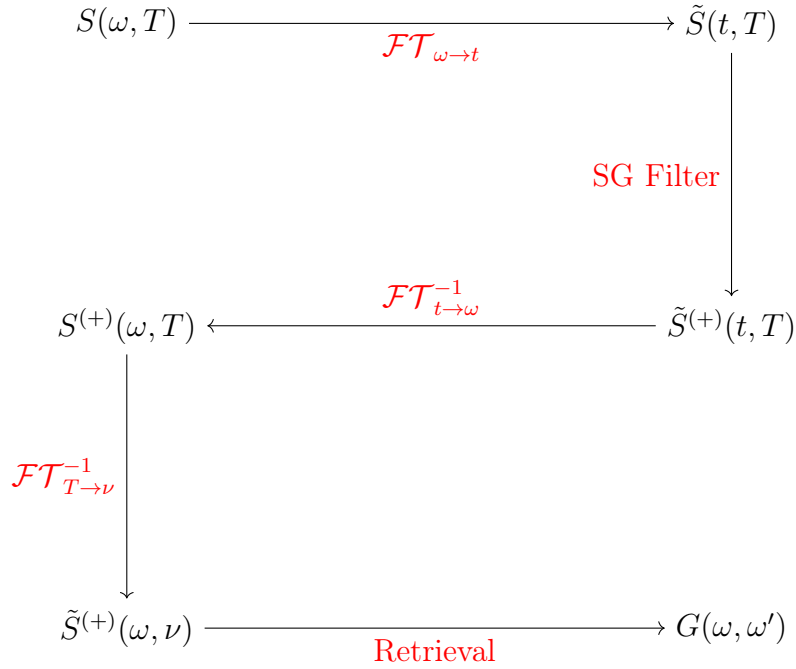


Figure 3.6. Layout of the reconstruction algorithm.

To summarize, the algorithm of extracting the transfer Green's function $G(\omega, \omega')$ is laid out in Fig. 3.6.

CTMT-SI Algorithm

1. Acquire Spectral data $S(\omega, T)$.
2. Fourier transform the spectral data from $S(\omega, T)$ to $\tilde{S}(t, T)$.
3. Filter out one of the AC components (e.g. positive sideband) $\tilde{S}^{(+)}(t, T)$.
4. Inverse Fourier transform back $\tilde{S}^{(+)}(t, T)$ from the time domain to $\tilde{S}^{(+)}(\omega, \nu)$ in the spectral domain.
5. Extract $G(\omega, \omega')$ from $\tilde{S}^{(+)}(\omega, \nu)$.

Numerical Simulation

We perform numerical simulation in order to show that the proposed technique is experimentally feasible. Assume a Gaussian probe pulse $A(\omega)$ with a central frequency $\omega_0 = 2\pi/\lambda_0$ where $\lambda_0 = 803$ nm, and a temporal duration of 200 fs. We use the single-value decomposition to define the TMT output, such that

$$C(\omega, T) = \sum_{n=0}^{\infty} \tau_n \Phi_n(\omega) \int d\omega' \phi_n(\omega') A(\omega') e^{-i\omega' T}, \quad (3.11)$$

where $\phi(\omega')$ and $\Phi(\omega)$ are the input and output Schmidt modes respectively. We choose the Hermite-Gaussian (HG) basis to define our temporal modes such that

$$\phi_n(\omega) = \frac{H_n\left(\frac{\omega-\omega_0}{\Delta\omega_i}\right)}{\sqrt{n!2^n \Delta\omega_i \sqrt{\pi}}} e^{-\left(\frac{\omega-\omega_0}{\Delta\omega_i}\right)^2}, \quad (3.12)$$

where $\Delta\omega_i$ is the spectral bandwidth of the input modes and $H_n(x)$ is the Hermite polynomials expressed as

$$H_n(x) = (-1)^n e^{x^2} \frac{d^n}{dx^2} e^{-x^2}. \quad (3.13)$$

The first 5 terms of the Hermite polynomials are expressed as

$$\begin{aligned} H_0(x) &= 1, \\ H_1(x) &= 2x, \\ H_2(x) &= 4x^2 - 2, \end{aligned}$$

$$\begin{aligned}
H_3(x) &= 8x^3 - 12x, \\
H_4(x) &= 16x^4 - 48x^2 + 12.
\end{aligned}$$

We limit our numerical simulation to the first 5 modes, $n = 0, 1, 2, 3, 4$. The choice of the transmission coefficients τ_n depends on the case to be numerically simulated. For instance, in case of simulating a delta function, described below, we choose $\tau_n = 1$ for all n . We scan the varying time delay T over a period of 1 ps and 6 ps respectively to show the effect of the finite time sampling on the spectral broadening of the delta-like transfer maps. We then follow the algorithm described in above to extract $G(\omega, \omega')$ from the interference between $C(\omega, T)$ and $A(\omega, \tau)$.

Intraband TMT

As we mentioned above, intraband TMTs map temporal modes in the same spectral band, that is no frequency conversion between input and output modes occurs. As an example of an intraband TMT, we consider the case of a spectral phase shifter with the transfer function $G(\omega, \omega') \sim e^{i\phi(\omega)}\delta(\omega - \omega')$ as TMT to be probed with our interferometric method. Such a TMT does not alter the spectrum of the pulse $A(\omega')$. The spectral interferograms obtained at the output of the MZ interferometer with a scan over time T are given by Eq. (3.5) such that,

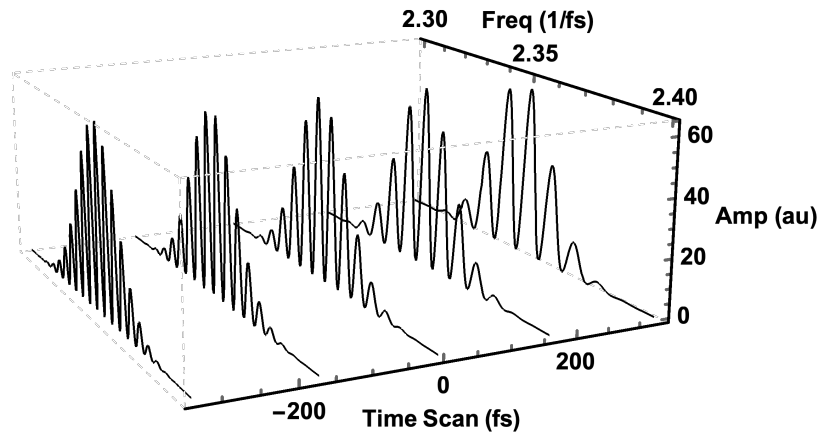
$$S(\omega, T) = |A(\omega)|^2 \{1 + \cos [\omega(T - \tau) - \phi(\omega)]\}, \quad (3.14)$$

which is identical in form to Eq. (3.1). We apply the algorithm described above in order to obtain the filtered AC component as

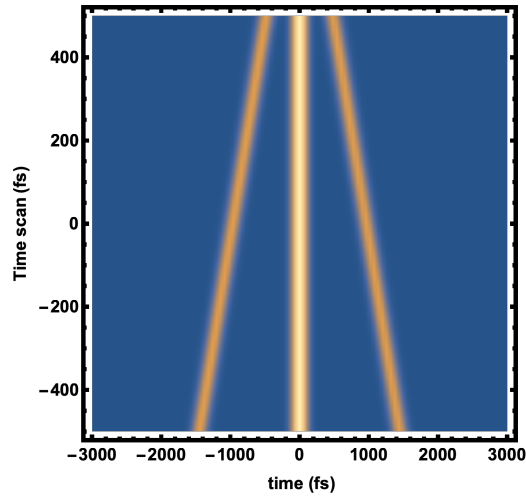
$$\tilde{S}^{(+)}(\omega, \nu) = \frac{1}{2}|A(\omega)|^2 e^{i\phi(\omega)} e^{i\omega\tau} [\sqrt{2\pi}\delta(\nu)]. \quad (3.15)$$

Since there is no frequency conversion between input and output modes in intraband TMTs, $\nu \sim \omega - \omega' = 0$, we substitute Eq. (3.15) into Eq. (3.10) to obtain the sought after transfer function $G(\omega, \omega') = e^{i\phi(\omega)}\delta(\omega - \omega')$.

An interesting case to consider for numerical simulation is the Dirac delta distribution $G(\omega, \omega') \sim \delta(\omega - \omega')$. The reason behind this interest is that QPGs are controlled by the temporal shape and strength of the gating pump pulse. In other words, the pump pulse is considered to be a control knob of the QPG. When the pump is switched off, the input mode undergoes no TMT and, therefore, the input and output modes are identical and their transfer map is represented by a

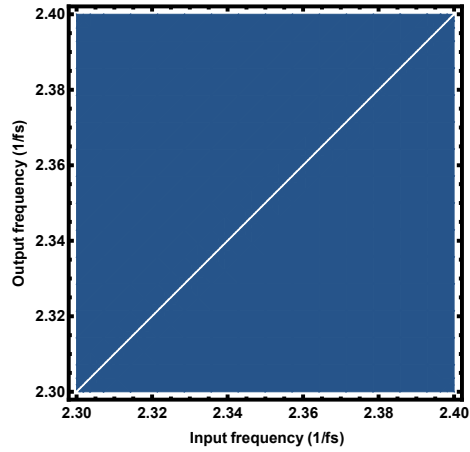


(a) Numerically-simulated spectrograms at different time scans for the linear phase shifter $S(\omega, T)$.

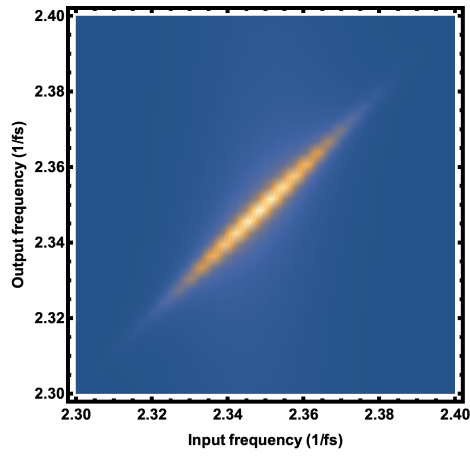


(b) Slanted sidebands due to the time scan T of the Fourier transform $\tilde{S}(t, T)$ of the spectrograms in 3.7a.

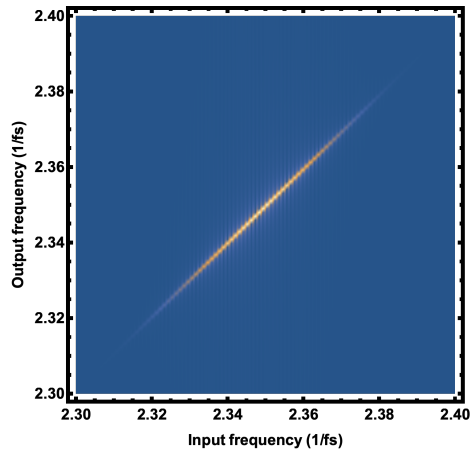
Figure 3.7. Numerical simulation of tomographic measurements of the linear phase shifter with phase function $\phi(\omega) = \alpha \omega$.



(a) Analytical transfer function $G(\omega, \omega') \sim e^{i\phi(\omega)}\delta(\omega - \omega')$.



(b) Simulation of the reconstructed transfer function over 1 ps time scan.



(c) Simulation of the reconstructed transfer function over 6 ps time scan.

Figure 3.8. Contour plots of the transfer functions of the LPS with a phase function $\phi(\omega) = \alpha \omega$.

Dirac delta. The Schmidt decomposition of the Dirac delta is not unique because all the weights, Schmidt coefficients, are equal to unity, in other words they are degenerate. The decomposition can be done with any complete set of orthonormal functions that satisfy Eqs. (2.29). Examples of typical orthogonal polynomials are Legendre, Hermite, Laguerre, Chebyshev and etc. We chose to work with Hermite-Gaussian basis since it represents the TM framework we employ. Therefore, the Schmidt decomposition of a Dirac-delta like transfer kernel is given as

$$\delta(\omega - \omega') = \sum_{n=0}^{\infty} \Phi_n(\omega) \phi_n(\omega'), \quad (3.16)$$

where both $\Phi_n(\omega)$ and $\phi_n(\omega')$ are output and input Hermite-Gaussian modes respectively. The fact that all the weights are equal to unity makes the sum of the squares of the weights diverges because the Dirac delta is not square-integrable. The numerical simulation then uses the decomposition (3.16) to identify the TMT output

$$C(\omega, T) = \sum_{n=0}^{\infty} \Phi_n(\omega) \int d\omega' \phi_n(\omega') A(\omega') e^{-i\omega' T}, \quad (3.17)$$

which undergoes spectral interference with the replica of the probe pulse $A(\omega')$. The steps described in the above algorithm and laid out in Fig. 3.6 are then applied in order to find the transfer kernel $G(\omega, \omega') \sim \delta(\omega - \omega')$. We now illustrate the reconstruction of linear and quadratic phase of intraband TMTs as examples of Dirac-delta like transfer maps.

Linear Spectral Phase $\phi(\omega) = \alpha \omega$

We now consider the case of a linear spectral phase shifter (LPS) in place of the TMT box under investigation, Fig. 3.5, with a phase function $\phi(\omega) = \alpha \omega$, where α is the induced time delay of a pulse in the units of fs. We probe the linear spectral phase shifter with a short Gaussian pulse $A(\omega)$ that is time-delayed and interfered with a replica of itself. Figures (3.7) show the numerical simulation of the resulting interferograms $S(\omega, T)$ and their Fourier transform $\tilde{S}(t, T)$ using a 1 ps time scan period T . Fig. 3.7b shows the slanted sidebands due to the time scan T . Applying the algorithm described in Section 3.2, we can reconstruct the transfer function of the LPS from Eq. (3.10) shown in Fig. 3.8. When extending the scan period $[-T', T']$ over times much longer than the time duration of the probing pulse

$A(\omega)$, $T' \gg \tau_A$, the reconstructed transfer function $G(\omega, \omega')$ asymptotically (by increasing T') reaches a delta-like function $\Delta(\omega - \omega' - \nu)$ of spectral bandwidth proportional to $1/2T'$ as shown in Figs (3.8b) and (3.8c). This behavior is expected since the limits of the Fourier transform with respect to T run from $-\infty$ to ∞ that gives rise to the delta function through which we are able to extract $G(\omega, \omega')$. As a result, the time period over which we delay the probe should always be longer than all other relevant times particularly the time duration of the probe pulse $A(\omega)$.

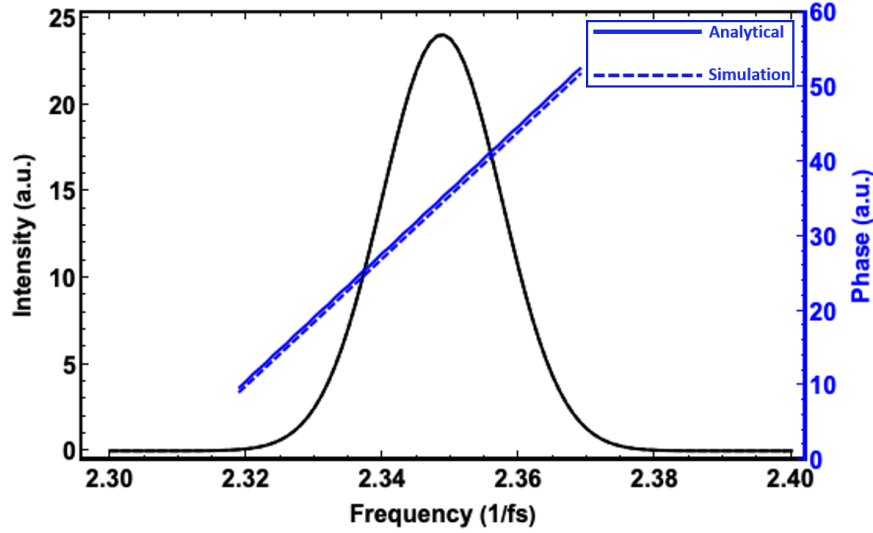


Figure 3.9. Spectral phase and intensity after the action of a linear spectral phase shifter with a phase function $\phi(\omega) = \alpha \omega$, where $\alpha = (2000/\omega_0)$ with $\omega_0 = 2\pi c/\lambda_0$ and $\lambda_0 = 803\text{nm}$.

The simulation shows that the reconstructed transfer function of the linear phase shifter agrees with the analytical expression $G(\omega, \omega') \sim e^{i\phi(\omega)}\delta(\omega - \omega')$ shown in Fig. 3.8a demonstrating feasibility of the proposed CTMT-SI technique.

As an example, we simulate the LPS setting the time-delay parameter $\alpha = 852$ fs and the central wavelength is $\lambda_0 = 803$ nm in the Hermite-Gaussian basis of TMs. We get the input-output pulses with the linear phase shown in Fig. 5.13 with a simulated time-delay parameter $\alpha_{\text{sim}} \sim 855\text{fs}$. The input and output pulses match since there is no pulse stretching or compression.

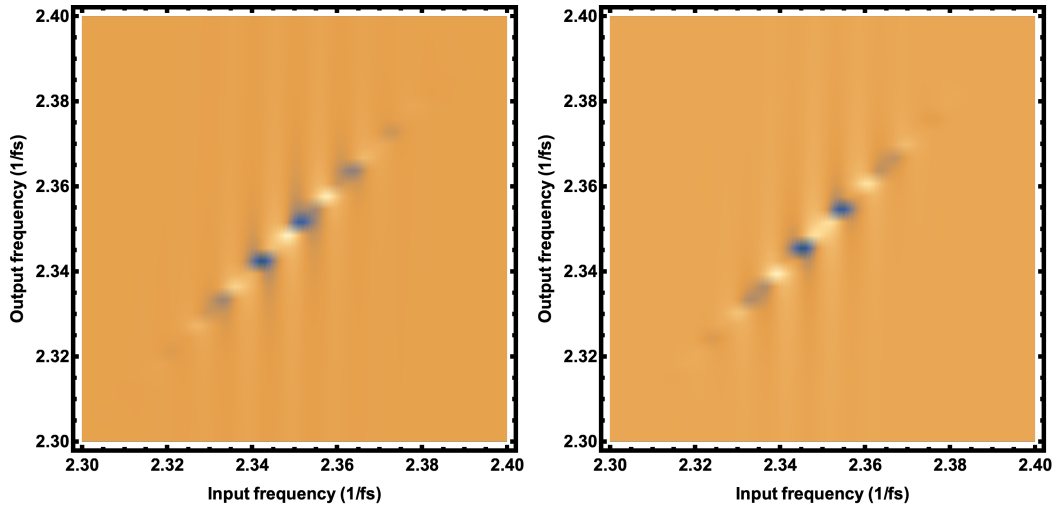


Figure 3.10. Contour plots of the real (left) and imaginary (right) parts of the transfer function of the Dirac delta with a linear Phase $\Phi(\omega) = \alpha\omega$.

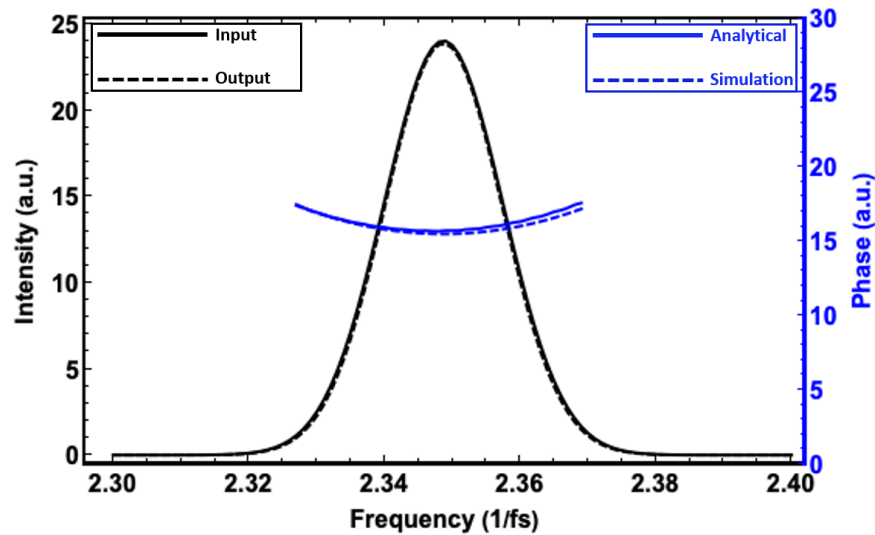


Figure 3.11. Quadratic spectral phase and intensity of the input and output pulses undergoing a quadratic phase shift with a phase function $\phi(\omega) = \beta \omega^2$ where $\beta = (150/\omega_0)^2$.

Quadratic Phase Shifter $\phi(\omega) = \beta \omega^2$

It is worth investigating the case of a quadratic spectral phase when there is a chirp added to the pulse. The phase function of the quadratic phase shifter (QPS) is expressed as $\phi(\omega) = \beta \omega^2$, where β is the chirping parameter in units of fs^2 . For the case of a waveguide with a chirping parameter $\beta \sim 4080 \text{ fs}^2$ the input-output pulses with the quadratic phase are shown in Fig. 3.11 with a simulated chirping parameter $\beta_{\text{sim}} \sim 4360 \text{ fs}^2$. The quadratic nature of the transfer function $G(\omega, \omega')$ appears when plotting the real and imaginary parts of $G(\omega, \omega')$ as shown in Figs. (3.12). The chirping parameter of a periodically-poled Lithium niobate (PPLN) waveguide of thickness 10 mm that is used in the experiment described in [El +] is measured to be $\beta_{\text{exp}} \sim 4166 \text{ fs}^2$. The Sellmeier equation for Lithium niobate predicts the chirping parameter for the same waveguide to be $\beta_{\text{Sellmeier}} \sim 4257 \text{ fs}^2$ which agrees with our model.

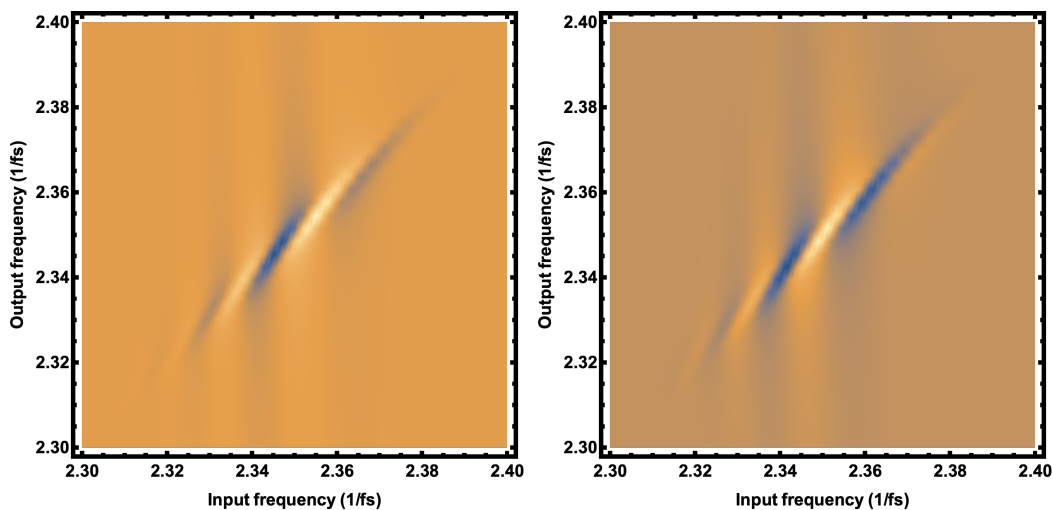


Figure 3.12. Contour plots of the real (left) and imaginary (right) parts of the transfer function of the Dirac delta with a quadratic phase $\Phi(\omega) = \beta\omega^2$.

It should be noted that the *artifacts* that appear in Figs. 3.8, 3.10 and 3.12 are due to using a limited number of modes in our simulations. In our numerical simulations, we used only five modes, $n = 0, 1, 2, 3, 4$. Increasing the number of modes considered in the sum in Eq. (3.17) gets rid of these artifacts asymptotically with $n \rightarrow \infty$.

Interband TMT

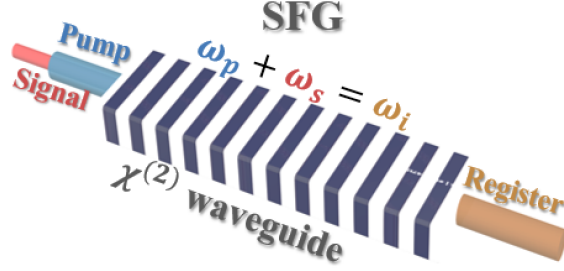


Figure 3.13. A scheme showing sum-frequency generation (SFG) in a nonlinear $\chi^{(2)}$ waveguide that is periodically poled to ensure quasi phasematching.

In interband TMTs, the frequency of light in the mode undergoing transformation gets converted in second order nonlinear crystals $\chi^{(2)}$. In Fig. 3.13 we show the process of sum-frequency generation (SFG) in a nonlinear optical processes where the striped medium is a periodically-poled second-order nonlinear $\chi^{(2)}$ waveguide to ensure group-velocity matching between the pump and signal in the red band by the employ of quasi-phasematching [Red+13]. A configuration as in Fig. 3.13 performs a TMT of the form of Eq. (2.72) and is represented by Eqs. (2.80). In the absence of a seeding signal, $B(\omega'_i) = 0$, the output fields $C(\omega_r)$ and $D(\omega_b)$ read

$$C(\omega_r) = \int_{-\infty}^{+\infty} d\omega'_r G_{rr}(\omega_r, \omega'_r) A(\omega'_r), \quad (3.18)$$

$$D(\omega_b) = \int_{-\infty}^{+\infty} d\omega'_r G_{br}(\omega_b, \omega'_r) A(\omega'_r), \quad (3.19)$$

where both $G_{rr}(\omega_r, \omega'_r)$ and $G_{br}(\omega_b, \omega'_r)$ should be reconstructed in order to fully characterize the process under investigation. The technique described above in Section 3.2 is applied once for each transfer map yielding similar expressions to Eq. (3.10) with the difference that the probe for $G_{br}(\omega_b, \omega'_r)$ is frequency doubled prior to interference with idler/register fields. The transfer maps are expressed as

$$G_{rr}(\omega_r, \omega'_r) = \sqrt{\frac{2}{\pi}} \frac{\tilde{S}^{(+)}(\omega_r, \nu) e^{i\omega_r \tau}}{A^*(\omega'_r) A(\omega_r)}, \quad (3.20)$$

$$G_{br}(\omega_b, \omega'_r) = \sqrt{\frac{2}{\pi}} \frac{\tilde{S}^{(+)}(\omega_b, \nu) e^{i\omega_b \tau'}}{A^*(\omega'_r) A_{SHG}(\omega_b)}, \quad (3.21)$$

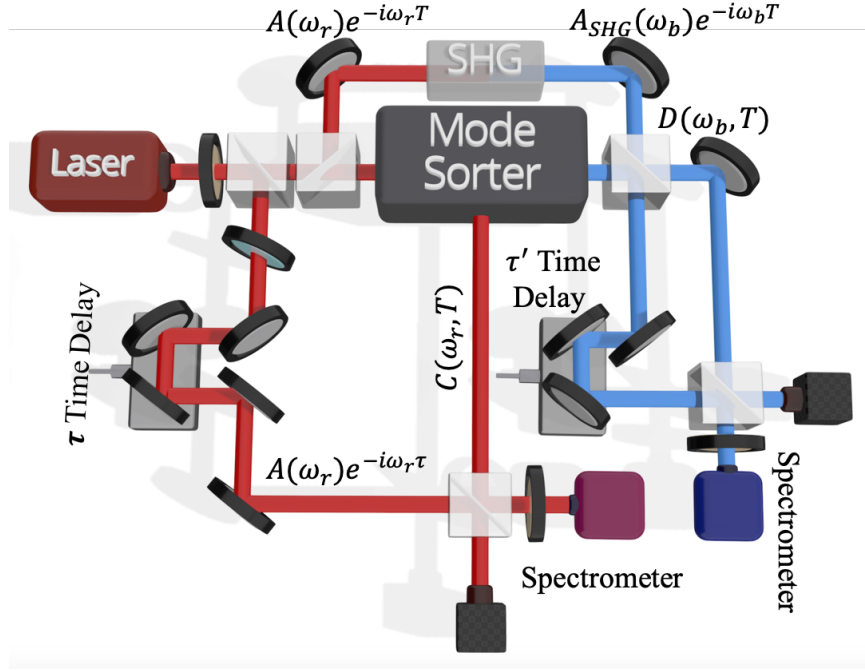


Figure 3.14. A proposed experimental setup to characterize interband TMTs. A probe mode $A(\omega_r)$ is split into two parts to probe the mode sorter and gets frequency doubled to be a reference for the "blue" interferometer. The outputs of the mode sorter $C(\omega_r)$ and $D(\omega_b)$ interfere with $A(\omega_r)$ and $A_{SHG}(\omega_b)$ respectively.

where $A_{SHG}(\omega_b) = -igL A^2(\omega_r') \frac{\sin(\Delta kL/2)}{\Delta kL/2} e^{i\Delta kL/2}$ with g the coupling constant that depends on $\chi^{(2)}$ of the nonlinear crystal whose length is L and $\Delta k = k(\omega_b) - 2k(\omega_r')$ is the phase-matching condition. A proposed experimental setup to characterize interband TMTs is shown in Fig. 3.14. The probe pulse $A(\omega_r)$ is split into two parts, one probes the TMT and the other gets frequency doubled in the blue band to be the reference for the blue interferometer. The outputs of the mode sorter $C(\omega_r)$ and $D(\omega_b)$ interfere with $A(\omega_r)$ and $A_{SHG}(\omega_b)$ respectively giving time-dependent spectrograms from which the Green functions can be extracted.

Time-Dependent Loss

In realistic experiments when we have a discretized time delay T over a finite sampling set, the Dirac delta function $\delta(\omega - \omega' - \nu) = \frac{1}{2\pi} \int dT e^{iT(\omega - \omega' - \nu)}$, arising from the Fourier transform of Eq. (3.8) with respect to T ($T \Rightarrow \nu$), becomes broader in the spectral domain. In addition, if there is any time-dependent loss in

the system (typically in pulse shapers when introducing the time delay), it needs to be accounted for while implementing the data analysis.

Assume that we have a time-dependent loss in the system $L(T)$, therefore, Eq. (3.8) becomes

$$\tilde{S}^{(+)}(\omega, T) = \frac{1}{2} \int d\omega' A^*(\omega) G(\omega, \omega') A(\omega') L(T) e^{iT(\omega-\omega')} e^{i\omega\tau}, \quad (3.22)$$

To this end, we invoke the no-pump correction representation of the transfer map introduced in Eq. (4.19),

$$G(\omega, \omega') = \delta(\omega, \omega') + \tilde{G}(\omega, \omega'), \quad (3.23)$$

such that

$$\begin{aligned} \tilde{S}^{(+)}(\omega, T) &= \frac{1}{2} \int d\omega' A^*(\omega) \delta(\omega, \omega') A(\omega') L(T) e^{iT(\omega-\omega')} e^{i\omega\tau} \\ &\quad + \frac{1}{2} \int d\omega' A^*(\omega) \tilde{G}(\omega, \omega') A(\omega') L(T) e^{iT(\omega-\omega')} e^{i\omega\tau}, \\ &= \frac{1}{2} |A(\omega)|^2 L(T) e^{i\omega\tau} \\ &\quad + \frac{1}{2} \int d\omega' A^*(\omega) \tilde{G}(\omega, \omega') A(\omega') L(T) e^{iT(\omega-\omega')} e^{i\omega\tau}, \end{aligned} \quad (3.24)$$

We then take the inverse Fourier transform of Eq. (3.24) with respect to T , we get

$$\begin{aligned} \tilde{S}^{(+)}(\omega, \nu) &= \frac{1}{\sqrt{2\pi}} \int dT \tilde{S}^{(+)}(\omega, T) e^{-i\nu T}, \\ &= \frac{1}{2\sqrt{2\pi}} |A(\omega)|^2 e^{i\omega\tau} \int dT L(T) e^{-i\nu T} \\ &\quad + \sqrt{\frac{\pi}{2}} \int d\omega' A^*(\omega) \tilde{G}(\omega, \omega') A(\omega') e^{i\omega\tau} \left[\int \frac{dT}{2\pi} L(T) e^{iT(\omega-\omega'-\nu)} \right], \\ &= \frac{1}{2\sqrt{2\pi}} |A(\omega)|^2 \Delta(\nu) e^{i\omega\tau} \\ &\quad + \sqrt{\frac{\pi}{2}} \int d\omega' A^*(\omega) \tilde{G}(\omega, \omega') A(\omega') \Delta(\omega - \omega' - \nu) e^{i\omega\tau}, \end{aligned} \quad (3.25)$$

where we define $\Delta(\nu)$ as the Fourier transform of the loss function $L(T)$ and $\Delta(\omega - \omega' - \nu)$ is the shifted Fourier transform. It should be noted that the first line of Eq. (3.25) is nothing but the spectral measurement when the pump is switched off, $\tilde{S}_{\text{no-pump}}^{(+)}(\omega, \nu)$.

Scanning time delay T over a finite sampling set instead of an infinite set gives rise to spectral broadening to the function Δ whose spectral bandwidth is proportional to $1/2T'$ where T' is the limit of the time scan. Due to this spectral broadening, it becomes challenging to extract the filtered transfer kernel $\tilde{G}(\omega, \omega')$ in a closed form. However, to circumvent this, we ensure that the sampling set over which we scan the time delay T is much longer than the temporal duration of the probe pulse τ_A . When this condition $T' \gg \tau_A$ is satisfied, the temporal duration of loss profile is much longer than all other time durations (see Fig. 4.8), and is nearly constant over the interaction time. As a result, the Fourier transform Δ can be approximated as a delta-like function (see Fig. 4.9 c and f). Therefore, Eq. (3.25) is approximated as

$$\begin{aligned} \tilde{S}^{(+)}(\omega, \nu) &\approx \tilde{S}_{\text{no-pump}}^{(+)}(\omega, \nu)e^{i\omega\tau} \\ &+ \sqrt{\frac{\pi}{2}}A^*(\omega)\tilde{G}(\omega, \omega')A(\omega')e^{i\omega\tau}, \end{aligned} \quad (3.26)$$

from which we can extract the filtered transfer map

$$\tilde{G}(\omega, \omega') \approx \sqrt{\frac{2}{\pi}} \frac{e^{-i\omega\tau}}{A^*(\omega)A(\omega')} \left[\tilde{S}^{(+)}(\omega, \nu) - \tilde{S}_{\text{no-pump}}^{(+)}(\omega, \nu) \right], \quad (3.27)$$

where $\tilde{S}_{\text{no-pump}}^{(+)}(\omega, \nu) = |A(\omega)|^2/2\sqrt{2\pi}$ is the spectral measurement when the pump is switched off. It is worth noting that this approximation holds for strong and moderate conversion limits and breaks down in weak conversion limit where the spectral width of the transfer map $\tilde{G}(\omega, \omega')$ is close to that of the Fourier transform $\Delta(\omega, \omega')$ of the loss profile.

CHAPTER 4

EXPERIMENTAL CHARACTERIZATION OF THE QPG

In this chapter, I describe the experimental demonstration of the characterization of the QPG using the CTMT-SI method presented in the previous chapter. First, I describe the setup of the QPG which was developed by the Raymer group [Red17]. The waveguide that was employed for the QPG setup is described in Sec. 4.1. The laser system that was used in the experimental setup is a home-built Ti:Sapphire laser and is presented in Sec. 4.2. In Sec. 4.3, I present the pulse shaper that was used to carve up the probe and pump pulses to characterize the QPG. I outline the experimental results of the characterization of the QPG in Sec. 4.4.

Experimental Design

4.1 Waveguide

The QPG utilized in this work is based on Reddy [Red17] who did an extensive analysis to choose the waveguide for a highly selective quantum pulse gate. The optimum requirements of the QPG rely on ensuring a long effective interaction time inside the waveguide between the group-velocity matched (GVM) pump and signal pulses. In the configuration of a second-harmonic generation (SHG) waveguide, which converts light from 812 nm to 406 nm at a temperature of 24.25°C, frequency conversion (FC) is achieved by positioning the probe and pump frequencies on opposite sides of the SHG pump frequency's red band. The bandwidths for SHG acceptance are characteristically narrow, ensuring efficient frequency conversion. To prevent the unintended production of spurious blue light solely from the pump, it is crucial that the FC pump frequency is adequately separated from the SHG pump frequency. This separation, combined with the inherent spectral flatness associated with normal dispersion, facilitates conditions close to group-velocity matching (GVM), optimizing the efficiency of the frequency conversion process. When SHG waveguides are pumped at the sum frequency, the process can lead to the creation of degenerate photon pairs through Spontaneous Parametric Down-Conversion (SPDC). The joint spectral distribution of these photon pairs demonstrates a strong anticorrelation which is indicative of the limited acceptance bandwidth of the SHG process's red pump band [LCS09]. Nonetheless, the spec-

tral width of each photon in the pair is broad, permitting the occurrence of sum frequency generation (SFG) from two spectral domains situated adjacent to the SHG pump frequency. This behavior renders commercial SHG waveguides as viable components for conducting frequency conversion (FC) experiments with a focus on temporal mode (TM) selectivity. Fig. 4.2 shows the blue light generated when Gaussian pump and signal pulses were coupled into the waveguide. As can be observed, there are two peaks in the blue spectral region at the 405.5 nm, which is the SFG peak, and at 407.5 nm which is the pump-only SHG peak which is independent of the signal presence. The two peaks were separated by a Semrock TBP01-400/16 tunable bandpass filter at angle of incidence 17° . The SHG signal-only peak is ignored since I work with weak signal powers.

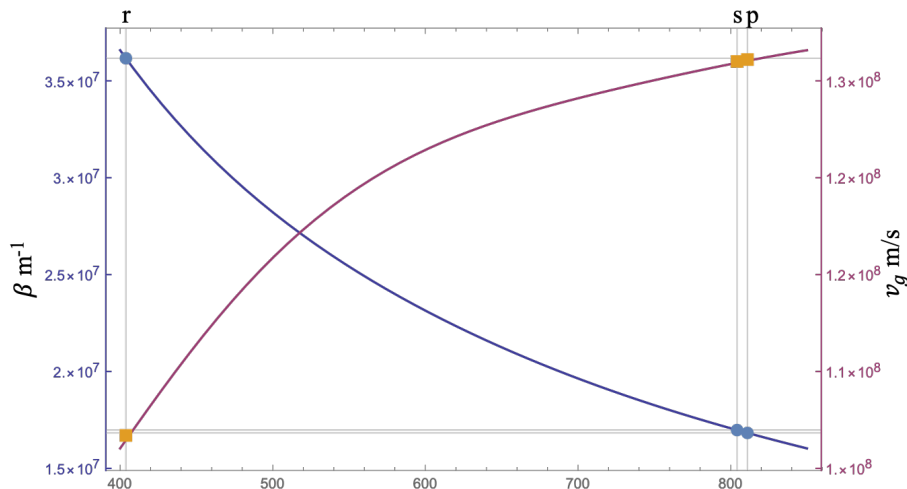


Figure 4.1. The wavenumber (β) and the group velocity ($v_g = d\omega/d\beta$) versus wavelength (λ) for a typical $5 \mu\text{m}$ wide, periodically-poled, MgO:LN waveguide. Also shown are the r-, s-, and p- bands that I utilize for SFG.

I employed a 10 mm MgO-doped PPLN wafer from the company AdvR, which was poled to perform Type-0 SHG (all fields co-polarized) from NIR (810 nm) to blue (405 nm) wavelengths. The waveguide ensured near-GVM conditions as shown in Fig. 4.1 where the group velocities of the pump and probe are nearly identical. I used a waveguide oven whose temperature control accuracy is $\pm 0.01^\circ\text{C}$ and was designed and built at the University of Oregon Machine shop by Cliff Dax and Jeffrey Garman.

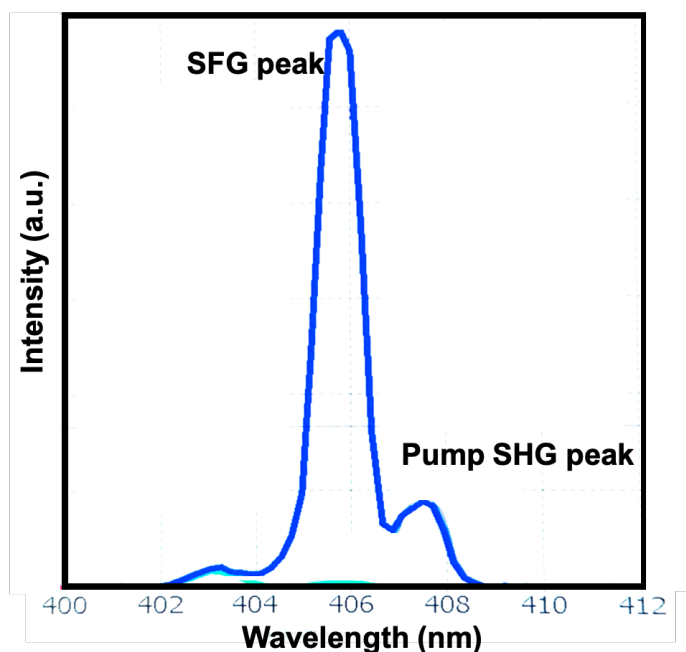


Figure 4.2. Blue light spectra generated from the QPG in a typical run. The SFG peak requires both the pump and signal to be present at the input, whereas the pump-only SHG peak remains even without the signal, and occurs due to imperfections in poling.

4.2 Ultrafast Laser

The experimental design necessitated the generation of pump and probe pulses with tunable shapes, closely spaced in their wavelengths (a spectral separation of approximately 8 nm) and temporally synchronized to optimize for conversion efficiency. To achieve this, the construction of an in-house ultrafast, Kerr-lens mode-locked Titanium-Sapphire (Ti:Sapphire) laser was undertaken, offering a broad spectral bandwidth from which the desired pump and signal spectra could be meticulously extracted.

The architecture of the Ti:Sapphire laser system employed a Brewster-angle cut Ti:Sapphire crystal, integrated within a water-cooled assembly for thermal management. The pumping mechanism involved the focal concentration of continuous wave (CW) laser light, specifically at a wavelength of 532 nm, into the crystal's core. This was facilitated by a 15 W Sprout-G diode-pumped Nd:YVO₄ (Neodymium-doped Yttrium Vanadate) laser, sourced from LightHouse Photonics.

The excitation of the Ti:Sapphire crystal by the green pump laser induced a broad fluorescence spectrum in the near-infrared (near-IR) range, serving as the fundamental emission for the laser operation.

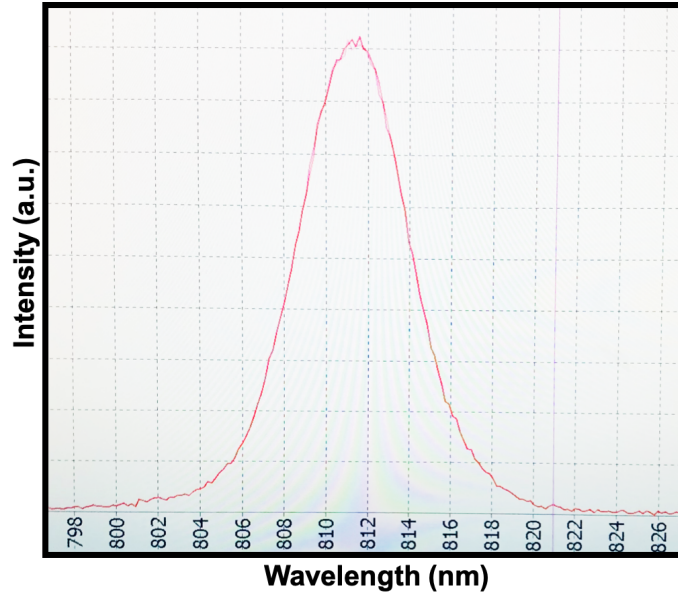


Figure 4.3. The spectrum of the in-house built Ti:Sapphire laser system tuned at $\lambda_0 \sim 811$ nm and bandwidth $\Delta\lambda \sim 8$ nm.

To construct the resonant optical cavity, a combination of curved and flat mirrors, designed to minimize group-delay dispersion (GDD), were mounted around the crystal. This arrangement formed a linear cavity that, when aligned to resonate at specific fluorescence wavelengths, facilitated the amplification of spontaneous emission through stimulated emission processes, thereby initiating lasing. The cavity's design included one partially transmissive end-mirror to allow a fraction of the coherent light to emerge as the usable laser output.

For the generation of ultrafast pulses, the Ti:Sapphire laser system was further modified with the inclusion of a pair of highly dispersive prisms, serving as a mechanism for dispersion compensation. This arrangement allowed for the differential path length adjustment for various wavelengths, thereby supporting multi-wavelength resonance within the cavity. The intrinsic Kerr nonlinearity of the Ti:Sapphire crystal, denoted as $\chi^{(3)}$, played a pivotal role in modulating the crystal's refractive index based on the electric field intensity of the intracavity light. At high field

intensities, this nonlinearity could induce self-focusing effects, contributing to the formation of a lensing effect within the crystal medium. This phenomenon, in concert with the dispersion-compensating prisms, facilitated the stable generation of ultrawide-band pulses characterized by significant peak intensities.

The transition from continuous wave to pulsed operation, or mode-locking, was instigated by a minor mechanical perturbation applied to the cavity structure, typically affecting the prism mounts. This mode-locking process resulted in the production of pulses at a repetition rate determined by the cavity's round-trip time, which, in this specific setup, was 76 MHz. The pulse's spectral bandwidth and central frequency were fine-tuned through the introduction of an adjustable slit, formed by two razor blades placed within the cavity. The manipulation of the slit's dimensions and position allowed for precise control over the pulse's spectral properties.

This description encapsulates the design and operational principles underlying the construction and utilization of an in-house ultrafast, Kerr-lens mode-locked Ti:Sapphire laser system for the generation of manipulated, temporally synchronized pump and probe pulses, tailored for advanced quantum optics experiments and applications. The spectrum of the in-house build Ti:Sapphire laser system is shown in Fig. 4.3.

4.3 4f-Line Pulse Shaping

The laser was tuned to generate pulses with a bandwidth of 8 nm and centered at 811 nm at repetition rate of 76 MHz. In order to manipulate the shape of the laser pulses, we used a home-built pulse shaper that relies on the configuration of Treacy-grating pair 4f-line system [Tre69] as shown in Fig. 4.4.

The 4f-line pulse shaping technique is a cornerstone in the field of ultrafast optics, enabling the precise manipulation of the temporal and spectral characteristics of ultrashort laser pulses. This method hinges on the principle of Fourier transform optics, utilizing a 4f optical configuration to shape light pulses. This setup consists of two identical diffraction gratings aligned in the Littrow configuration [Wei00; MWC10]. These gratings are instrumental in dispersing the frequency components of an incoming pulse across varied angles, a process described by the grating equation

$$d(\sin \alpha + \sin \beta) = \lambda, \quad (4.1)$$

where d represents the line spacing of the grating, α the incident angle, β the first-order diffraction angle, and λ is the wavelength of the incident pulse. The configuration aims to approximate the Littrow condition ($\alpha = \beta$) as closely as possible to optimize the angular dispersion. Subsequent to dispersion, a lens positioned at its focal length from the grating maps angle to position the spectral components onto the Fourier plane, where a spatial light modulator (SLM) applies specific amplitude and phase modulations. In a 4f-line pulse shaper, the spectral components are first spatially dispersed by a diffraction grating and focused onto a spatial light modulator (SLM) by a lens with focal length f . The SLM modulates the phase and amplitude of these components, which are then recombined by a second identical lens and grating to form the shaped pulse. The SLM modulation is governed by the transfer function $H(\omega)$, facilitating the synthesis of the shaped pulse

$$E_{\text{out}}(\omega) = \mathcal{F}\{E_{\text{in}}(t)\} = \frac{1}{\sqrt{2\pi}} \int_{-\infty}^{\infty} E_{\text{in}}(t) e^{-i\omega t} dt, \quad (4.2)$$

where $E_{\text{in/out}}(\omega)$ represents the input/output electric field of the incident and shaped light, respectively, in the frequency domain, ω is the angular frequency, and \mathcal{F} denotes the Fourier transform.

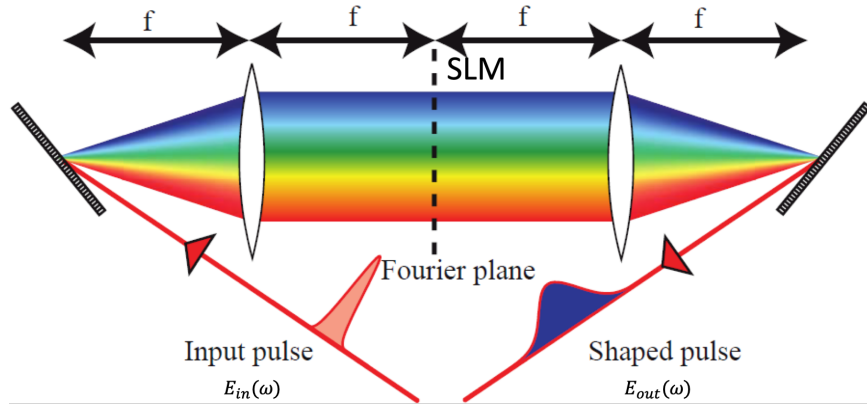


Figure 4.4. Schematic of a 4f-line pulse shaper that consists of two diffraction gratings, two lenses and a spatial light modulator (SLM) placed at the Fourier plane.

The modulation imposed by the SLM is described by a transfer function $H(\omega)$, yielding the shaped pulse

$$E_{\text{shaped}}(\omega) = H(\omega)E_{\text{out}}(\omega). \quad (4.3)$$

The temporal profile of the shaped pulse is retrieved by the inverse Fourier transform

$$E_{\text{shaped}}(t) = \mathcal{F}^{-1}\{E_{\text{shaped}}(\omega)\} = \frac{1}{\sqrt{2\pi}} \int_{-\infty}^{\infty} E_{\text{shaped}}(\omega)e^{i\omega t}d\omega. \quad (4.4)$$

The pulse shaping depends on the spectral resolution and diffraction efficiency of the gratings, the temporal range which is the maximum temporal window that can be shaped, and the spectral resolution of the SLM which depends on the number of pixels in the SLM. For a given collimated beam incident on the grating with an initial spot diameter denoted by w_0 , the consequent spot diameter projected onto the Fourier plane is determined by $w_f = \lambda_0 f / (\pi w_0)$, where λ_0 is the central wavelength of the incident pulse and f is the focal length of the lens. This relationship implies that as the focal length f increases, both the spatial separation and the diameters of the focused spots corresponding to different spectral components exhibit proportional enlargement. The choice of focal length is thus critical, tailored to align the spot diameter at the Fourier plane with the spatial resolution or the pixel dimensions of the modulating devices, without exceeding these parameters. Additionally, the diameter of the incoming beam must be sufficiently broad to fulfill the plane-wave approximation, enhancing the grating's resolution by engaging a larger number of its lines. In our experimental setup, the ultrafast laser beam was spatially broadened to achieve a transverse diameter of approximately 7 mm, subsequently channeled through a Treacy-grating-pair pulse shaper configured in a folded 4f arrangement [Tre69]. This configuration incorporated a reflective spatial light modulator (SLM) positioned at the Fourier plane. The pulse shaping system employed a holographic grating with 1800 lines/mm, optimized to operate close to the Littrow configuration, and a cylindrical lens with a 250 mm focal length to accurately focus the spectral components onto the SLM. The cylindrical lens's was chosen to disperse the beam's intensity along the vertical axis, thereby preventing potential damage to the SLM. The resulted spot diameter of the shaped beam was approximately 5 μm for each wavelength component.

The SLM used in the setup is a Meadowlark 8-bit, 2D, phase-only liquid-crystal spatial light modulator of 1920×1152 pixel resolution and array size of 17.6 mm \times

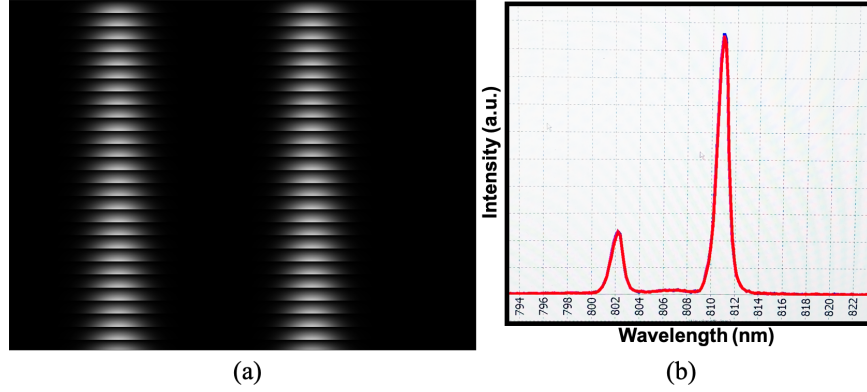


Figure 4.5. Modulation mask on the SLM (a) and the respective spectra (b) of the carved out pulses in the pump and signal bands.

10.7 mm. The pixels were squares of side $9.2 \mu\text{m}$ and the fill factor was 95.7% and the reflectivity is 97.%. The modulation of both phase and amplitude of the incident pulse is performed through applying a vertical blazed grating mask on the SLM [Red17]. The $m = 1$ order reflection is then picked off as the output shaped beam. An example of such masks applied on the SLM is shown in Fig. 4.5 where we carve out two bands for the pump and signal. The probe and pump frequency bands can be independently manipulated by changing the mask over the pixels that cover each band. As described in our CTMT-SI method in Section 3.2, the probe pulse $A(\omega, T) = A(\omega)e^{-i\omega T}$ is temporally delayed through the application of a linear phase ramp to the probe band of the modulation mask on the SLM as shown in Fig. 4.6.

Spatial-Spectral Coupling in Pulse Shaping

An intriguing phenomenon encountered in the realm of 4f-line pulse shaping is the spatial-spectral coupling, a direct consequence of introducing phase modulations via the SLM. When a phase pattern is imparted onto the spectral components of a pulse by the SLM, not only are the temporal characteristics of the pulse altered, but there is also a resultant spatial displacement of the beam. This displacement arises due to the phase gradient introduced across the beam's profile, leading to an angular deviation as the beam exits the pulse shaper.

The mathematical foundation of this effect can be traced to the principle of

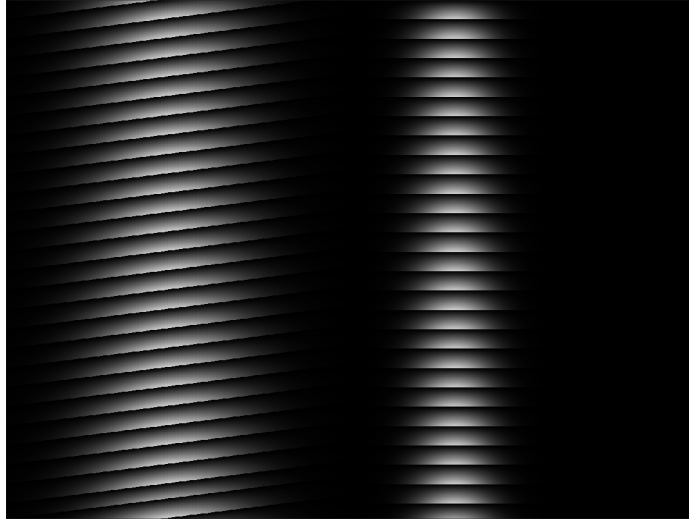


Figure 4.6. Linear phase ramp applied to the probe band of the modulation mask on the SLM.

angular dispersion in optics, where the phase modulation $\Phi(\omega)$ introduced by the SLM imparts a wavevector shift Δk to the diffracted beam. This shift can be expressed as

$$\Delta k = \frac{d\Phi(\omega)}{cd\omega}. \quad (4.5)$$

This wavevector shift translates to an angular deviation $\Delta\theta$ of the beam, given by the relation

$$\Delta\theta = \frac{\lambda}{2\pi}\Delta k. \quad (4.6)$$

Consequently, the spatial displacement of the beam at a distance L from the pulse shaper can be quantified as $L\Delta\theta$, illustrating the spatial manifestation of the temporal modulation.

It is worth noting that the spatial-spectral coupling effect has implications for applications that rely on precise beam positioning and alignment. The interplay between the spatial and temporal domains necessitates careful calibration of the phase modulation patterns to mitigate undesired beam displacements, ensuring that the intended temporal shaping is achieved without compromising the spatial integrity of the beam.

Due to the spatial-spectral coupling in the pulse shaper, the efficiency of beam coupling into the waveguide decreases with increasing the time delay imposed on

the probe pulse as shown in Fig. 4.7. The spatial displacement of the first-order diffracted beam δx in the horizontal plane increases proportionally with increasing the temporal delay imposed on the probe pulse as shown in the far right and far left beams. On top of that, such spatial displacement is larger in the configurations when the pulse shaper is not well optimized. It is worth mentioning that such spacial displacement is a fundamental characteristic of the intertwined spectral and temporal nature of ultrashort pulses and will persist to exist no matter how perfectly the pulse shaper is aligned. As a result, the efficiency of the coupling the shaped beam into the waveguide reduces with increasing the temporal delay that is applied on the beam. Several methods to mitigate the effect of the spatial-temporal interference are introduced below.

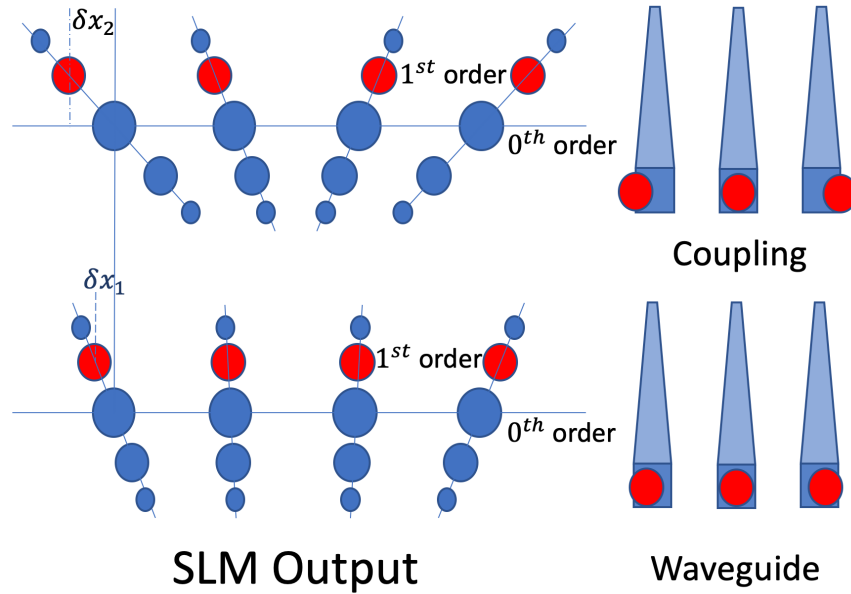


Figure 4.7. Schematic of spatial displacement of the $m = 1$ reflected beam due to spatial-temporal interference in the pulse shaper when a linear phase mask is applied to the SLM to temporally delay the incident pulse. Larger displacements occur when the pulse shaper is not well-optimized (top) and when longer delays are imposed (far right and far left beams). The efficiency of the coupling in the waveguide is directly affected by beam displacement (right).

Mitigation Strategies

To counteract the effects of spatial-temporal interference, several strategies have been developed, focusing on both the design of the pulse shaping setup and the modulation patterns applied to the SLM.

1. **Adaptive Phase Compensation:** By implementing adaptive optics techniques, the phase modulation pattern on the SLM can be dynamically adjusted to compensate for the induced spatial displacement. This approach involves iteratively optimizing the phase pattern to minimize beam displacement while achieving the desired temporal shaping [Tre69].
2. **Beam Steering Mechanisms:** Incorporating active beam steering elements, such as piezo-electrically controlled mirrors, in the optical path following the pulse shaper allows for the correction of beam displacement in real-time. This method provides a direct means to re-align the shaped beam to its intended spatial trajectory [Wei11].
3. **Pre-dispersion Compensation:** By pre-shaping the beam before it enters the 4f-line setup with a complementary spatial phase profile, the effects of spatial-temporal interference can be neutralized. This pre-compensation requires careful calibration based on the specific phase modulations applied by the SLM [MWC10].
4. **Dual SLM Configuration:** Employing a second SLM in the pulse shaping setup, dedicated solely to spatial shaping, allows for independent control over spatial and temporal characteristics of the beam. This dual SLM approach decouples the temporal shaping from spatial effects, providing a versatile solution to the challenge of spatial-temporal interference [Wei00].

In practice, my mitigation strategy was to optimize the pulse shaper as well as possible and then incorporate such loss effect in the analysis so that the data is reliable. I measured the loss in intensity of the transmitted signal at the output of the waveguide when scanning over time and then I introduce a transmission function $L(T)$ in my analysis. The transmission function is found to be close to both Gaussian and super Gaussian functions as depicted in Fig. 4.8. For the sake of simplicity, I chose the transmission function to be Gaussian, thus $L(T) \sim \exp(-T^2/2\tau_L^2)$,

where τ_L is the bandwidth of $L(T)$. The transmission function profile in the spectral domain is shown in Fig. 4.9 for different temporal bandwidths compared to the temporal bandwidth of the probe pulse. In our experiment, the temporal bandwidth of the probe pulse is $\tau_a \sim 230$ fs and for the measured transmission function $L(T)$ is $\tau_L \sim 3000$ fs, therefore their ratio is approximately 13. This ratio as shown in Fig. 4.9.d enables us to approximate this transmission function $L(T)$ in the spectral domain as a Dirac delta function. As shown in Fig. 4.10, the transmission function value is almost constant over the interaction time of the pump and probe enabling us to approximate the extraction of the filtered transfer map $\tilde{G}_{rr}(\omega_r, \omega'_r)$.

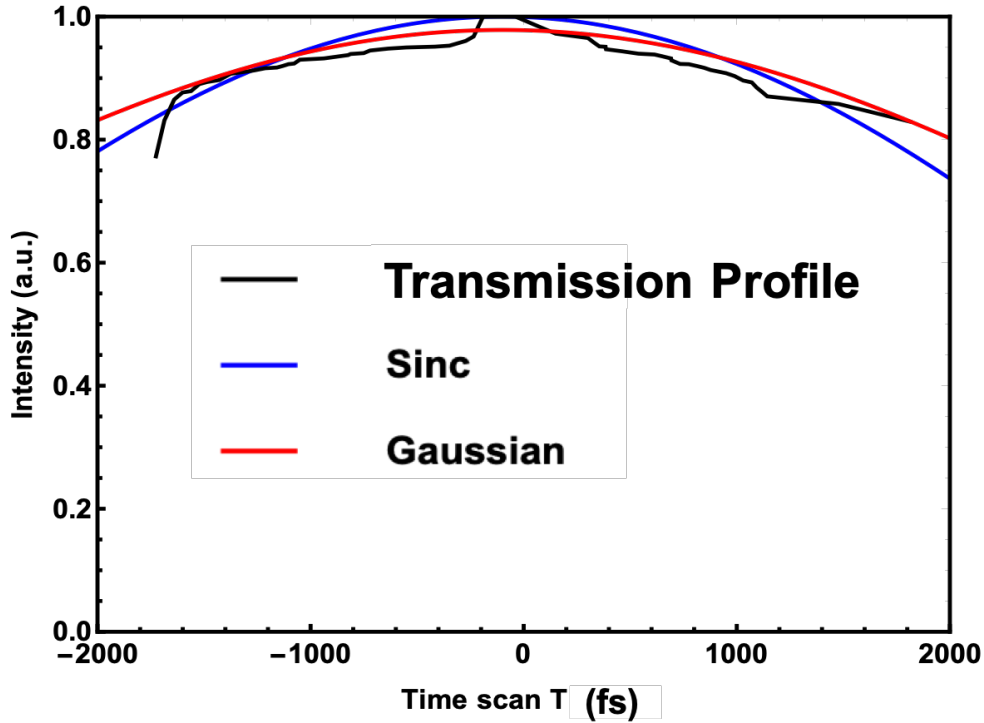


Figure 4.8. Measured loss profile $L(T)$ (Black), a Sinc function (Blue) and a Gaussian profile (Red).

Subtraction of the No-Pump Transfer Map

To mitigate the loss effects in the analysis of our data, we invoke the no-pump correction representation which was introduced in Section 2.6. The main idea is to

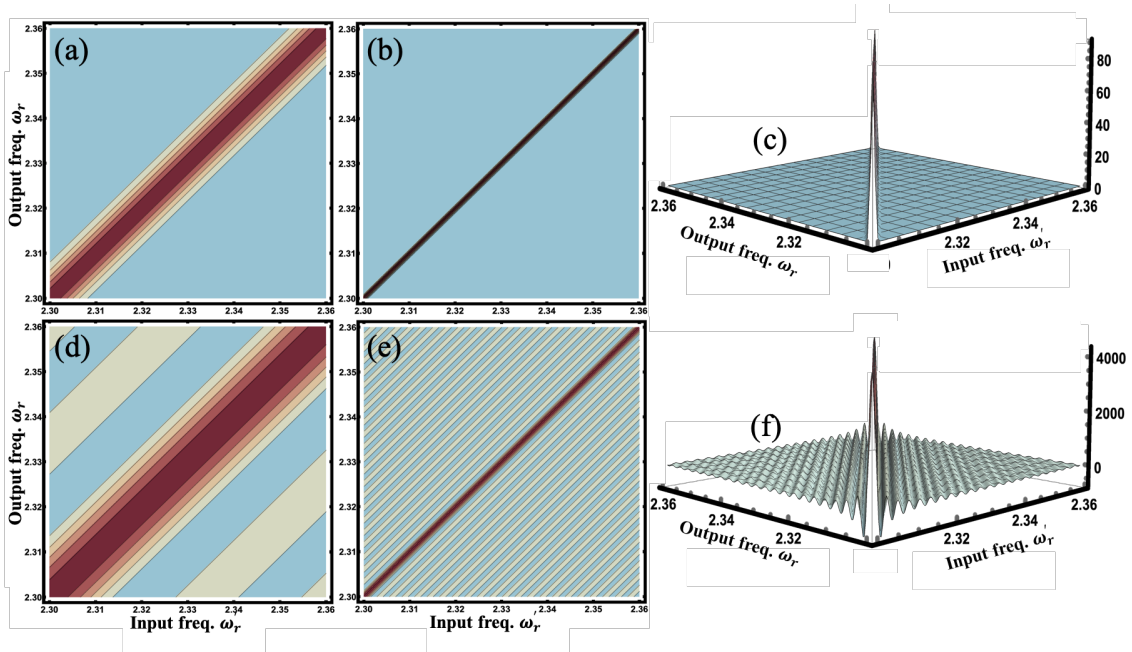


Figure 4.9. Modeling of the loss profile $L(T)$ in the spectral domain over finite time scan T as a Gaussian profile (a —c) and a Sinc function (d —f) for bandwidths $\tau_L \sim \tau_A$ in (a, c) and $\tau_L \sim 10\tau_A$ in (b, d) compared to the bandwidth of the probe pulse. 3D plots of (b, d) are shown in (e, f).

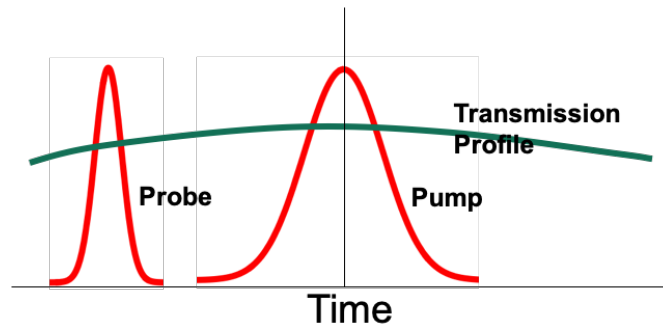


Figure 4.10. A schematic depiction of the probe and pump interaction inside the waveguide in the time domain where we fix the pump and sweep the probe along time with the transmission function profile. The transmission function value is almost constant over the interaction time of the pump and probe.

take same spectral measurements but when the device is switched off (mode does not undergo a temporal mode transformation) and then subtract it at the end in order to extract the filtered $\tilde{G}(\omega, \omega') = G(\omega, \omega') - \delta(\omega, \omega')$ such that

$$\tilde{G}(\omega, \omega') \approx \sqrt{\frac{2}{\pi}} \frac{e^{-i\omega\tau}}{A^*(\omega)A(\omega')} \left[\tilde{S}^{(+)}(\omega, \nu) - \tilde{S}_{\text{no-pump}}^{(+)}(\omega, \nu) \right], \quad (4.7)$$

where $\tilde{S}_{\text{no-pump}}^{(+)}(\omega, \nu)$ is the same spectral measurement in the case of no temporal mode transformation when the pump is switched off.

We use the ideal and realistic cases of the Green transfer maps shown in Fig. 2.5 (a) and (c) as two examples to examine this filtering technique. In the ideal case as shown in Fig. 4.11, we simulate measuring the spectral data in the absence of the pump pulse and with a transmission function whose temporal bandwidth is the same as that of the probe pulse as shown in Fig. 4.11.a. We then switch on the pump and repeat the simulation of the spectral measurement and then reconstruct the transfer map. By subtracting the no-pump and loss measurement we can retrieve the Green transfer map as shown in Fig. 4.11.c. As can be easily seen, the ideal case of a Green transfer map is not drastically affected by such loss or convolution even though the loss is quite temporally narrow. In realistic systems, this is not the case as shown in Figs. 4.12 and 4.13. For temporally narrow loss as depicted in panels 4.12.a, the filtered reconstructed Green transfer map as in Fig. 4.12.c is altered and the spectral measurements do not reflect the actual TMT under investigation. Hence, characterization of the TMT can not be addressed. On the other hand, temporally broad loss profiles give better results for the reconstruction of the Green transfer map as shown in Fig. 4.13.c. As mentioned above, the temporal bandwidth of the measured loss profile in our setup is approximately more than 10 times longer than that of the probe pulse. In other words, this means that the loss is approximately constant during the interaction time within the waveguide over the scan range used in the experiment. Consequently, the no-pump correction is viable in order to mitigate loss effects to a good approximation within a marginal error leading to a reliable characterization of the TMT under investigation.

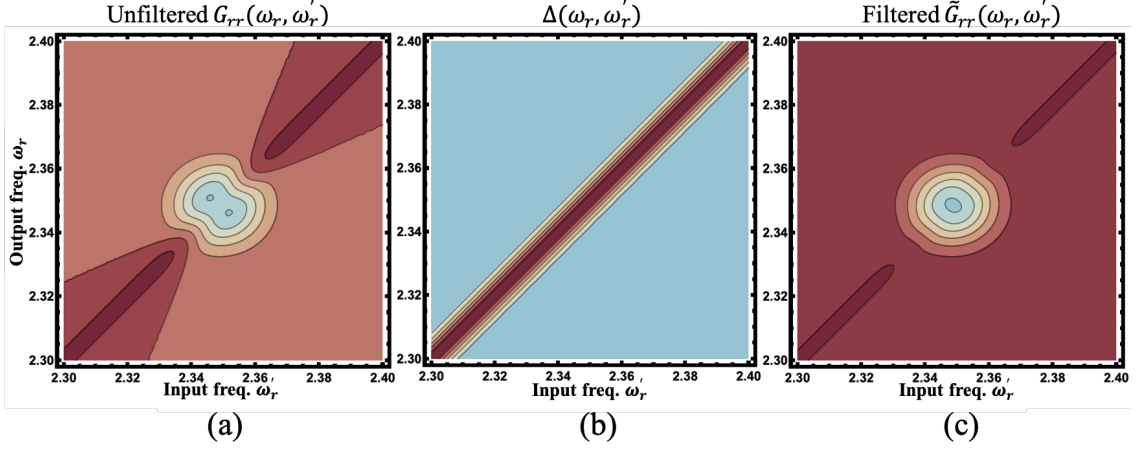


Figure 4.11. The numerically-simulated unfiltered $G_{rr}(\omega, \omega')$ transfer map (a) due to the broadening of the loss spectral profile $\Delta(\omega, \omega')$ (b) and the filtered $G_{rr}(\omega, \omega')$ transfer map (c) calculated by subtracting $G_{rr}(\omega, \omega') - \Delta(\omega, \omega')$ for an ideal QPG with selectivity ~ 1 . The bandwidth of the broadening is $\tau_L \sim \tau_A$.

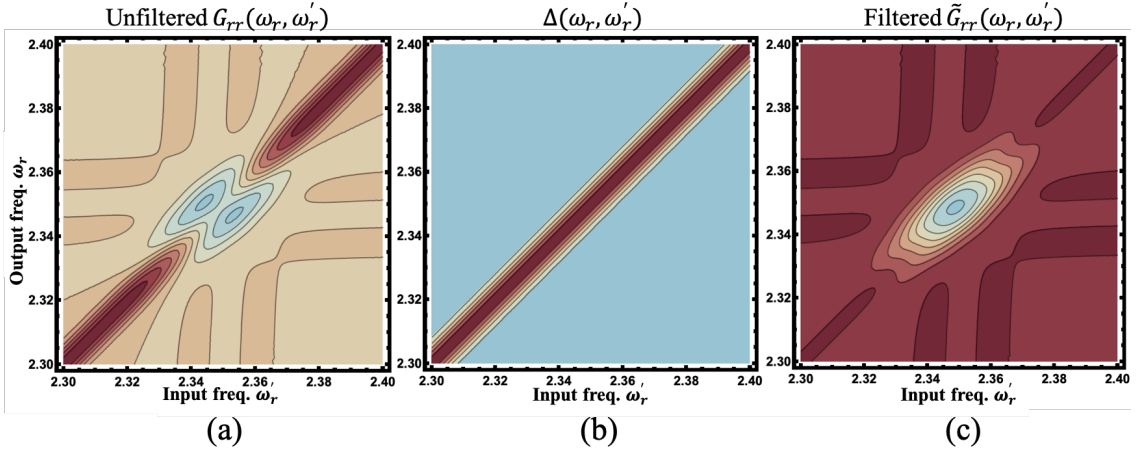


Figure 4.12. The numerically-simulated unfiltered $G_{rr}(\omega, \omega')$ transfer map (a) due to the broadening of the loss spectral profile $\Delta(\omega, \omega')$ (b) and the filtered $G_{rr}(\omega, \omega')$ transfer map (c) calculated by subtracting $G_{rr}(\omega, \omega') - \Delta(\omega, \omega')$ for a realistic QPG with selectivity ~ 0.5 . The bandwidth of the broadening is proportional to $1/\tau_L \sim 1/\tau_A$ where τ_L is the time duration of the transmission profile of the loss and τ_A is the temporal duration of the probe pulse $A(\omega)$.

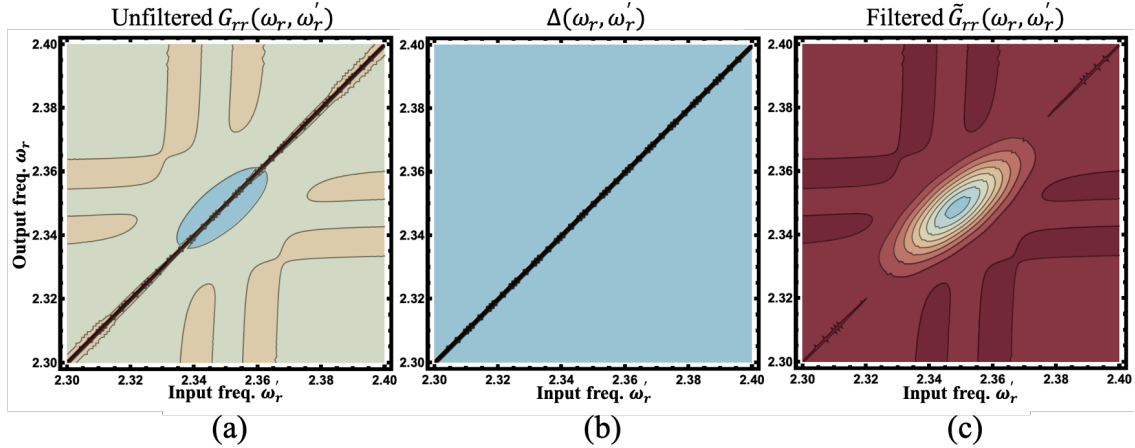


Figure 4.13. The numerically-simulated unfiltered $G_{rr}(\omega, \omega')$ transfer map (a) due to the broadening of the loss spectral profile $\Delta(\omega, \omega')$ (b) and the filtered $G_{rr}(\omega, \omega')$ transfer map (c) calculated by subtracting $G_{rr}(\omega, \omega') - \Delta(\omega, \omega')$ for a realistic QPG with selectivity ~ 0.5 . The bandwidth of the broadening is $\tau_L \sim 10\tau_A$.

4.4 Characterization of QPGs

Infrared (IR) Part: $G_{rr}(\omega_r, \omega_r')$

Fig. 4.14 shows the experimental setup employed in order to characterize the quantum pulse gate under investigation. It reconstructs the Green transfer map $G_{rr}(\omega_r, \omega_r')$ in the IR spectral region where ω_r and ω_r' stand for the frequency of the transmitted and input signal in the IR spectral region respectively.

The output of the Ti:Sapphire laser centered around $\lambda_0 = 811$ nm and has a bandwidth of $\Delta\lambda = 8$ nm is split by a beam splitter into two parts. The first beam (far left) is filtered by a Semrock LL01-810-12.5 bandpass filter to create the reference pulse $A(\omega)$ which goes through a fixed time delay τ and then coupled with the output of the waveguide on another beam splitter. The other part of the Ti:Sapphire laser output is directed into the pulse shaper to generate a pump and probe pulse $A(\omega, T)$ similar to the output of the bandpass filter. I carve the probe band pulse around 804 nm with a bandwidth of 4 nm the pump band around 811 nm with a 2 nm bandwidth. The time durations of both probe and pump band pulses are 230 fs and 500 fs respectively. I then apply a changing linear phase ramp only over the pixels of the probe band to scan the time delay T . The probe is short

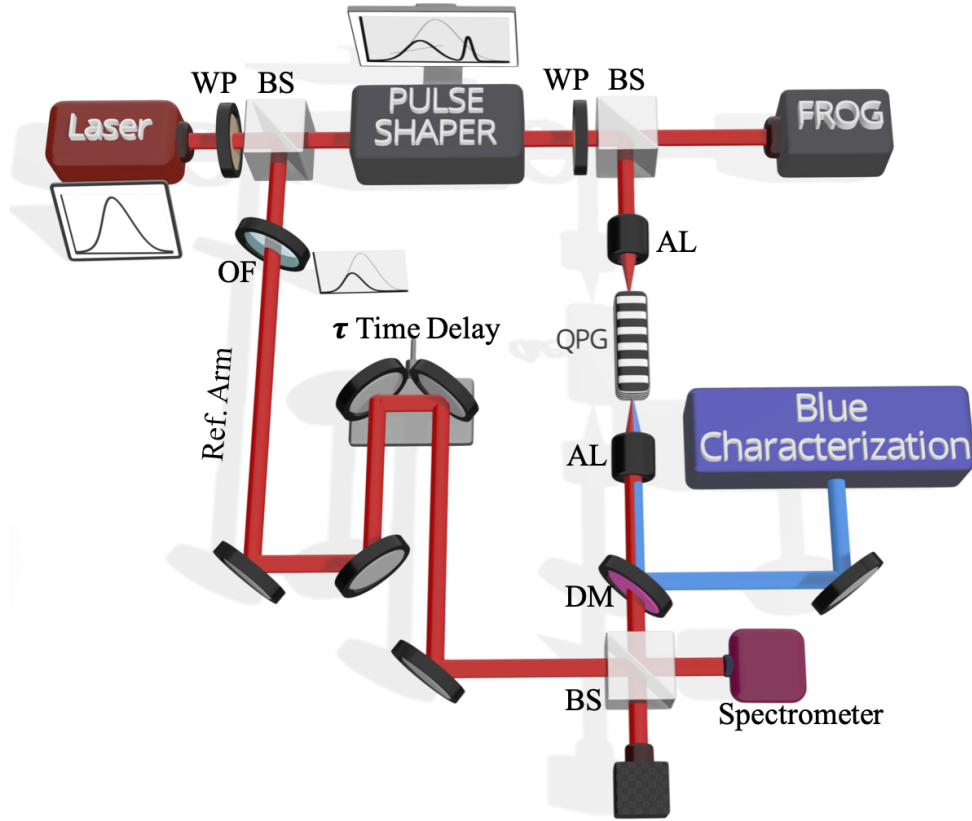


Figure 4.14. Experimental setup of our technique of characterizing the quantum pulse gate that reconstructs the Green transfer map $G_{rr}(\omega_r, \omega'_r)$ in the IR spectral region. WP is waveplate, BS is beam splitter, OF is optical filter, AL is aspherical lens and DM is dichroic mirror. Other optical components are not shown.

in time to ensure that a Gaussian probe is a superposition of the input modes of the QPG. The pump power coupled into the waveguide was varied from 0 —2.92 mW which was sufficient for high conversion efficiency without much pump depletion. I use Reddy’s [Red17] method of representing the pump powers in $\bar{\gamma} \sim 18\sqrt{W}$ for the sake of consistency. The probe pulse power was $80 \mu\text{W}$, therefore its SHG is neglected.

The co-propagating pump and probe are then coupled into the waveguide (QPG in Fig. 4.14) with an aspheric lens of $f = 11 \text{ mm}$. The output of the waveguide is spectrally split by a Thorlabs DMLP650 bandpass dichroic mirror operating at 45° . The blue output propagates through the blue part of the experiment (right part of Fig. 4.14) to be investigated which we will discuss later. The transmitted red

output is interfered with the reference pulse on a beam splitter and the spectral measurements are collected by a spectrometer of 0.1 nm resolution.

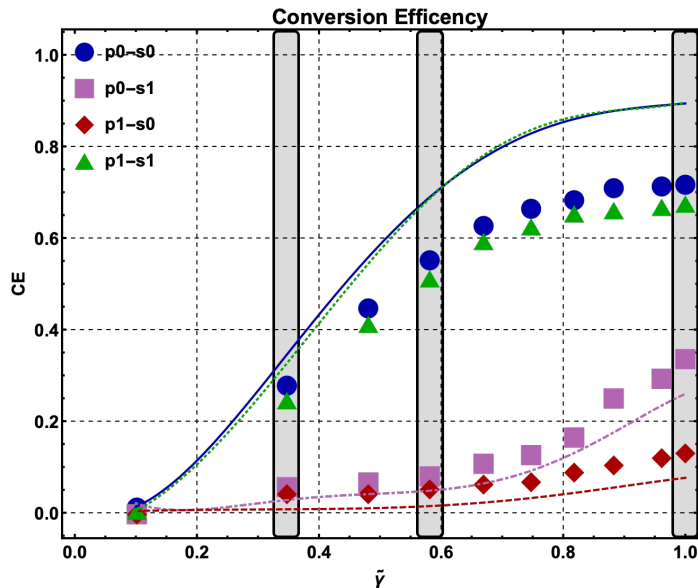


Figure 4.15. CE versus $\bar{\gamma} \propto \sqrt{P_{\text{pump}}}$ for zeroth and first order HG pump pulses. Curves are theory in case of Schmidt modes and marker points are for zeroth and first order HG signal pulses. Blue circles show the case where both pump and signal are zeroth-order HG shape, purple squares is for zeroth-order HG pump and first-order HG signal, red diamond-shaped points are for first-order HG pump and zeroth-order HG signal and green triangle points are for first-order HG shapes for both pump and signal pulses. The three gray boxes designate the values of the pump power at which we run our CTMT-SI technique. From right to left, we have weak (0.32 mW), moderate (0.98 mW) and strong (2.92 mW) pump powers.

To ensure the QPG is operating as expected without performing characterization, a quick check involves measuring the CE for a given pump pulse shape at different pump power levels and for different input signal pulse shapes. As a reference, I repeat Reddy's [Red17] direct measurements of the CE for the single-stage experiment where I match and mismatch the pump and signal pulse shapes (using zeroth and first order HG modes) while varying the pump power. Fig. 4.15 shows the CE vs pump power ($\bar{\gamma} \propto \sqrt{P_{\text{pump}}}$) curves for zeroth- and first- order HG pump shapes. The signal pulse takes the shapes of zeroth- and first- order HG modes. The solid lines are the theoretical prediction in case of input Schmidt modes of the QPG and the plotted points are for the experimentally measured Hermite-Gaussian

zeroth and first order pulse shapes. My data seems lower in CE compared to the results in [Red17] because they are shifted horizontally towards the right due to the use of different maximum pump power. The goal is to characterize the QPG rather than optimizing it in order to reach maximum conversion efficiency. The selectivity versus $\bar{\gamma}$ of the QPG, Eq. (2.85), is plotted in Fig. 4.16.

The CE vs pump power measurements is also used as a way to verify that the proposed CTMT-SI technique to characterize QPGs works reasonably well. The main idea of verification is to try to deduce the values of the CE at a given pump power without direct measurements and compare it with what we measure directly. The three gray boxes in Fig. 4.15 designate the values of the pump power at which we run our CTMT-SI technique. From right to left, we have weak (0.32 mW), moderate (0.98 mW) and strong (2.92 mW) pump powers. We repeat the experiment at every pump power for zeroth-, first- and second-order HG shapes for the pump pulse and calculate the CE for the first Schmidt modes of the signal and compare them to the directly-measured CE values as shown in the right panels of Figs. 4.29—4.31.

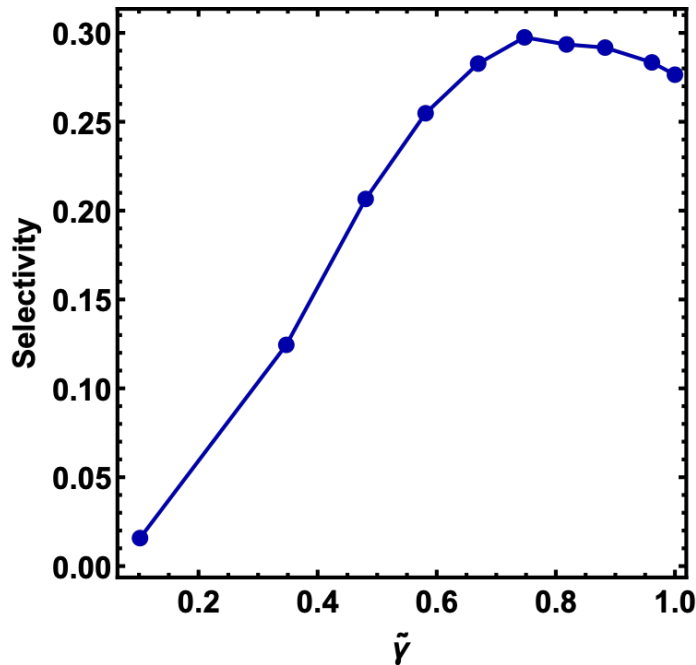


Figure 4.16. Selectivity versus $\bar{\gamma} \propto \sqrt{P_{\text{pump}}}$, Eq. (2.85), of the QPG under examination for a zeroth-order HG pump shape.

Next I take the spectral interferometric measurements of the red part from which I reconstruct the filtered Green transfer map, $\tilde{G}_{rr}(\omega_r, \omega'_r)$, of the QPG under investigation. Fig. 4.17 shows a numerically-simulated interferograms of our CTMT-SI model describing the QPG for different time steps. In the numerical simulations, I scan the time delay T over a 1 ps time period and the pulse duration of the probe is 160 fs while that of the pump pulse is 500 fs and of zeroth-order HG shape. I measure spectral interferograms with changing the time delay T between pump and probe in the pulse shaper as shown in Fig. 4.18.

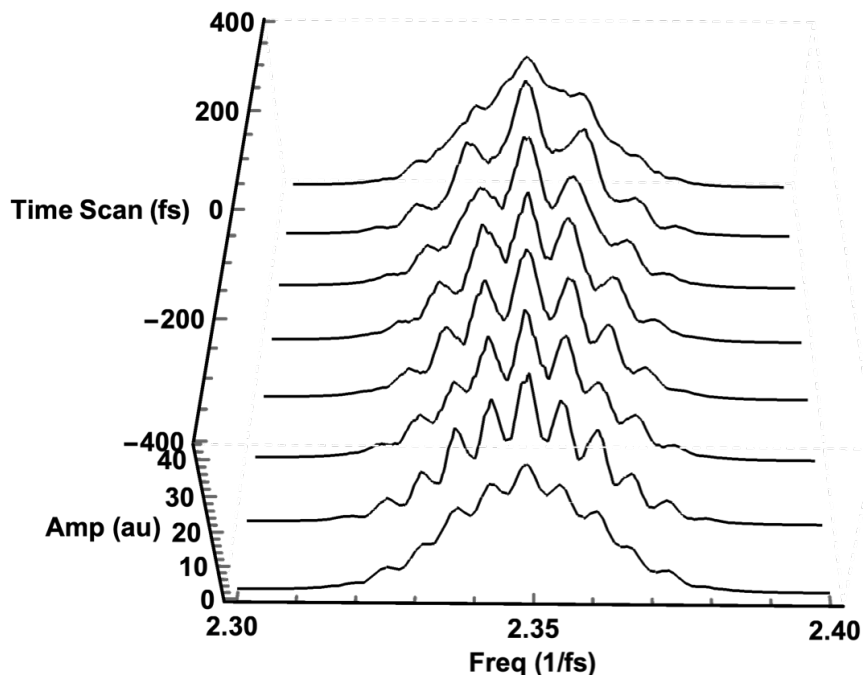


Figure 4.17. Numerically-simulated spectral interferograms over time scan of different delays between the pump and probe of the QPG.

Applying the algorithm described in Section 3.2 and outlined in Fig. 3.6, I was able to reconstruct the filtered Green transfer map, $\tilde{G}_{rr}(\omega_r, \omega'_r)$, of the QPG at different pump powers (0.32 mW, 0.98 mW, 2.92 mW) and different pump shapes (HG0, HG1, HG2) as shown in Figs. 4.20 — 4.28. As can be observed from the figures, the shape of the filtered transfer map of the transmitted signal $\tilde{G}_{rr}(\omega_r, \omega'_r)$ resembles the same shape expected from theory, Fig. 2.5.c for low selectivity of value $\approx 26\%$ for the strong pump case (2.92 mW) and it gets narrower for lower selectivity values as expected.

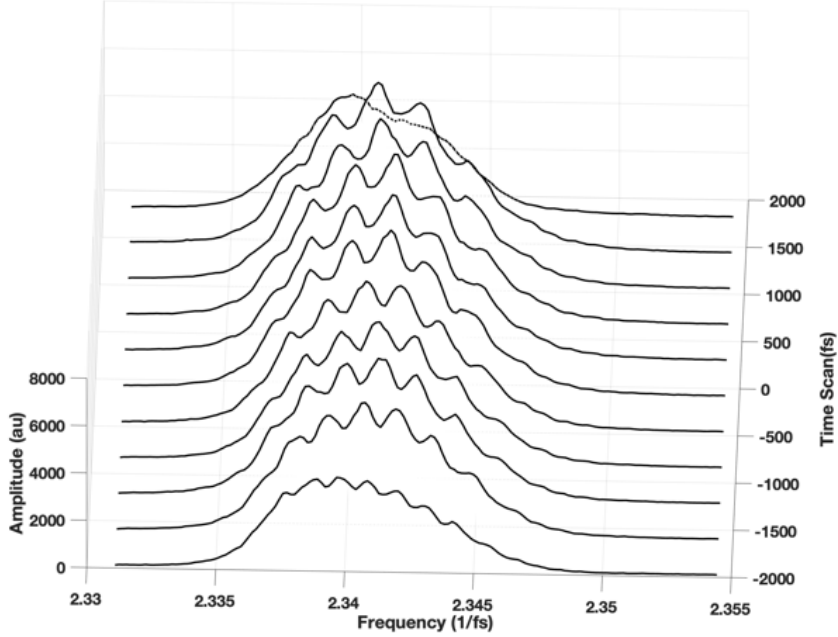


Figure 4.18. Experimental measurement of the spectral interferograms over time scan of different delays between the pump and probe of the QPG.

The transmission function introduced by the spatial-spectral coupling in the pulse shaper as discussed in Section 4.3 as well as the scan over a finite time period T instead of infinite time scan will give rise to the spectral broadening in case of no-pump and is shown in Fig. 4.19. Fortunately, the time duration of the time scan T of ~ 3.5 ps is much longer than the 230 fs time duration of the probe pulse. That indicates that in the frame of the probe pulse, both loss and finite scan are nearly constant giving rise to slightly broadening the Dirac delta function $\Delta(\omega_r, \omega'_r)$ in the spectral domain. Therefore, I switch off the pump by removing the grading mask over the pixels of the pump band and repeat the same spectral measurement and follow the exact same algorithm to reconstruct the broadened delta-like mapping $\Delta(\omega_r, \omega'_r)$ of the interference probe and reference without frequency conversion as shown in Fig. 4.19. By subtracting, Eq. (3.27), we obtain the filtered transfer map shown on the right panels in Figs. 4.20—4.28. As can be seen from the filtered transfer maps, in the case of strong and moderate conversion limits, the results show reasonably well shaped transfer maps from which we can extract the

SVD structures. However, in the weak conversion regime, the shapes are deformed and the extracted SVD structure is not descriptive of the actual QPG under investigation. When verifying our method against direct measurements of the conversion efficiency (see Figs. 4.29 —4.31), the error value is 2% and 3% for the strong and moderate conversion limits. In the case of weak conversion limit, the error value is about 8% showing that our method breaking down in that limit.

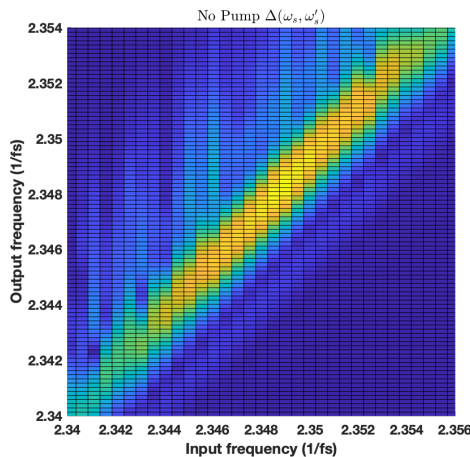


Figure 4.19. Experimental reconstruction of the no-pump IR Green transfer map $\Delta(\omega_r, \omega_r')$ of the QPG that will be subtracted from the reconstructed $G_{rr}(\omega_r, \omega_r')$ to give the filtered $\tilde{G}_{rr}(\omega_r, \omega_r')$ through Eq. (3.27).

Conversion Efficiency (CE)

As discussed previously in Sec. 4.4, the singular-value decomposition of the reconstructed Green transfer map gives the estimated transmission coefficients τ_n as well as the Schmidt modes $\phi_n(\omega_r')$ and $\Phi_n(\omega_r)$ as expressed in Eq. 2.86. We therefore perform the single value decomposition (SVD) of the filtered $\tilde{G}_{rr}(\omega_r, \omega_r')$ to obtain transmission coefficients $\tau_n = |1 - \lambda_n|$ and Schmidt modes, where λ_n are the Schmidt coefficients of $\tilde{G}_{rr}(\omega_r, \omega_r')$. For a zeroth-order HG pump of 2.92 mW power and 530 fs temporal duration, the transmission coefficients τ_n of the first three modes are (0.518, 0.866, 0.961). We repeat the same calculations in case of first and second order HG pump pulses. The transmission coefficients of the first three modes are given in table 4.3. In the table we notice that the values of transmission coefficients are lower for matching mode shapes meaning that less light get

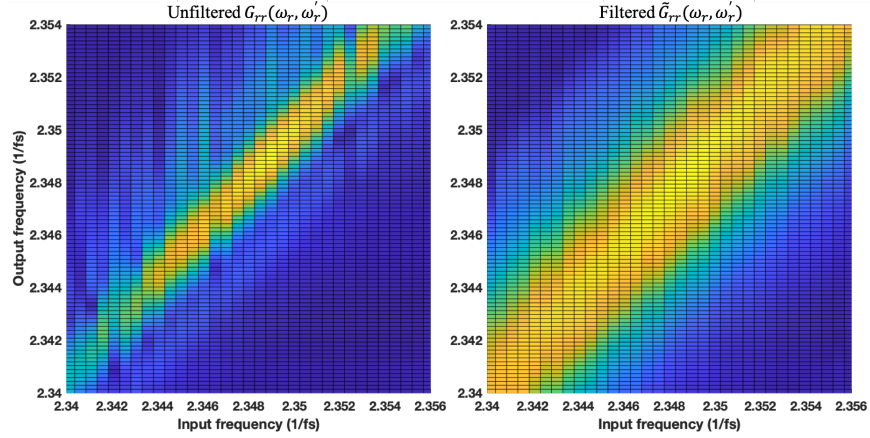


Figure 4.20. Experimental reconstruction of the IR Green transfer map $G_{rr}(\omega_r, \omega'_r)$ of the QPG for zeroth order HG pump pulse at 2.92 mW. The unfiltered $G_{rr}(\omega_r, \omega'_r)$ (left) when the pump is switched on. By subtracting the no-pump transfer map $\Delta(\omega_r, \omega'_r)$ in Fig. 4.19, we obtain the filtered $\tilde{G}_{rr}(\omega_r, \omega'_r)$ (right).

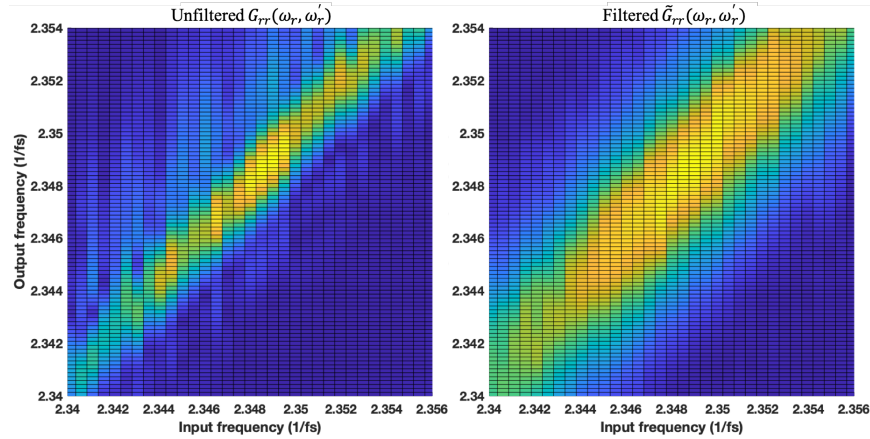


Figure 4.21. Experimental reconstruction of the IR Green transfer map $G_{rr}(\omega_r, \omega'_r)$ of the QPG for first order HG pump pulse at 2.92 mW. The unfiltered $G_{rr}(\omega_r, \omega'_r)$ (left) when the pump is switched on. By subtracting the no-pump transfer map $\Delta(\omega_r, \omega'_r)$ in Fig. 4.19, we obtain the filtered $\tilde{G}_{rr}(\omega_r, \omega'_r)$ (right).

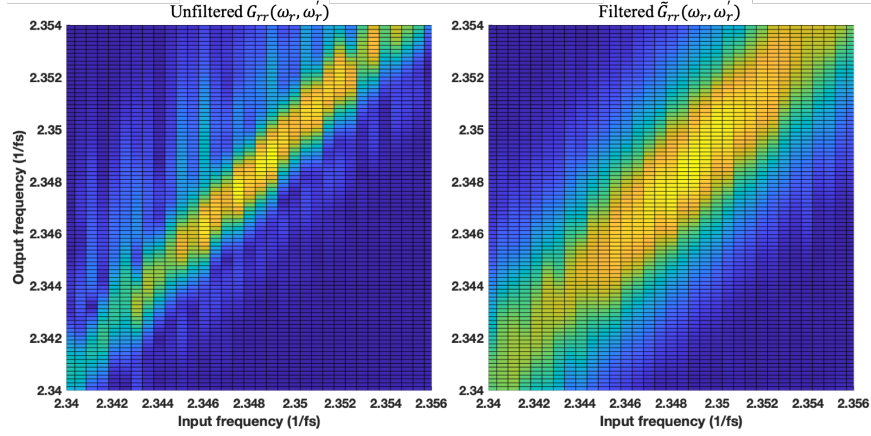


Figure 4.22. Experimental reconstruction of the IR Green transfer map $G_{rr}(\omega_r, \omega'_r)$ of the QPG for second order HG pump pulse at 2.92 mW. The unfiltered $G_{rr}(\omega_r, \omega'_r)$ (left) when the pump is switched on. By subtracting the no-pump transfer map $\Delta(\omega_r, \omega'_r)$ in Fig. 4.19, we obtain the filtered $\tilde{G}_{rr}(\omega_r, \omega'_r)$ (right).

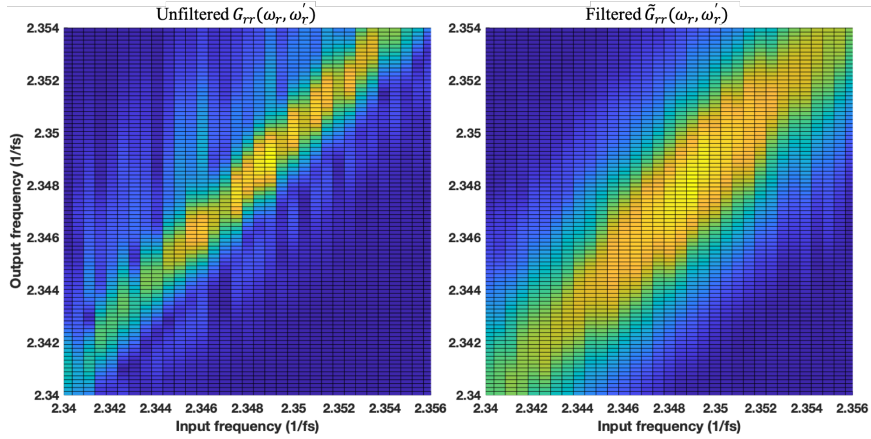


Figure 4.23. Experimental reconstruction of the IR Green transfer map $G_{rr}(\omega_r, \omega'_r)$ of the QPG for zeroth order HG pump pulse at 0.98 mW. The unfiltered $G_{rr}(\omega_r, \omega'_r)$ (left) when the pump is switched on. By subtracting the no-pump transfer map $\Delta(\omega_r, \omega'_r)$ in Fig. 4.19, we obtain the filtered $\tilde{G}_{rr}(\omega_r, \omega'_r)$ (right).

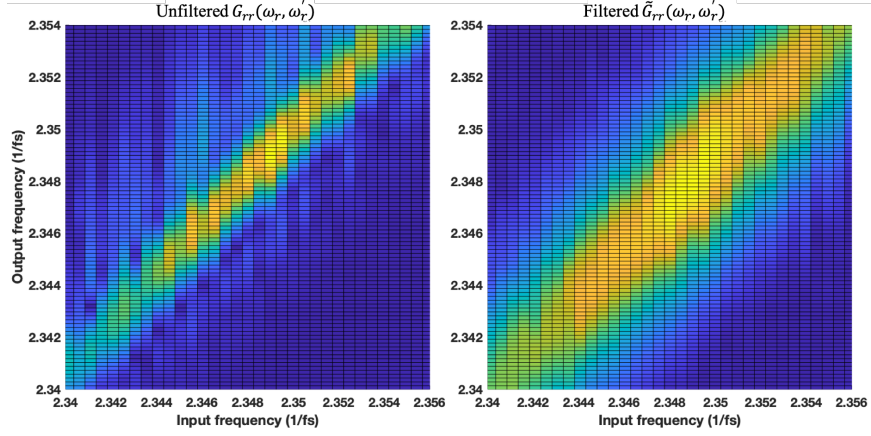


Figure 4.24. Experimental reconstruction of the IR Green transfer map $G_{rr}(\omega_r, \omega_r')$ of the QPG for first order HG pump pulse at 0.98 mW. The unfiltered $G_{rr}(\omega_r, \omega_r')$ (left) when the pump is switched on. By subtracting the no-pump transfer map $\Delta(\omega_r, \omega_r')$ in Fig. 4.19, we obtain the filtered $\tilde{G}_{rr}(\omega_r, \omega_r')$ (right).

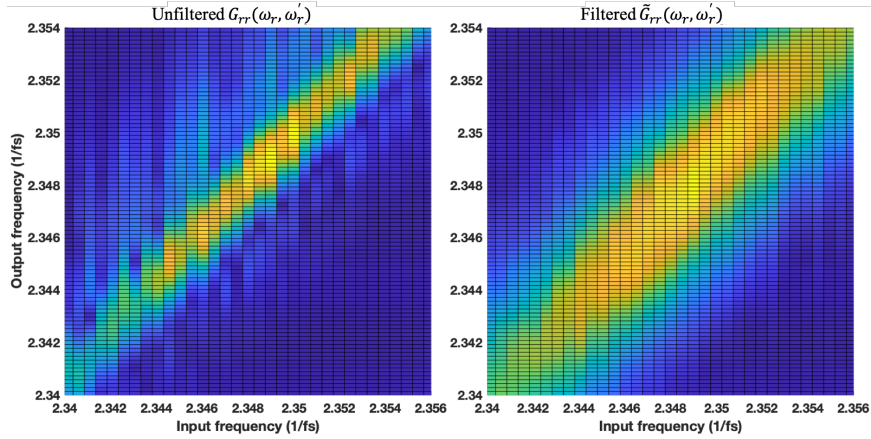


Figure 4.25. Experimental reconstruction of the IR Green transfer map $G_{rr}(\omega_r, \omega_r')$ of the QPG for second order HG pump pulse at 0.98 mW. The unfiltered $G_{rr}(\omega_r, \omega_r')$ (left) when the pump is switched on. By subtracting the no-pump transfer map $\Delta(\omega_r, \omega_r')$ in Fig. 4.19, we obtain the filtered $\tilde{G}_{rr}(\omega_r, \omega_r')$ (right).

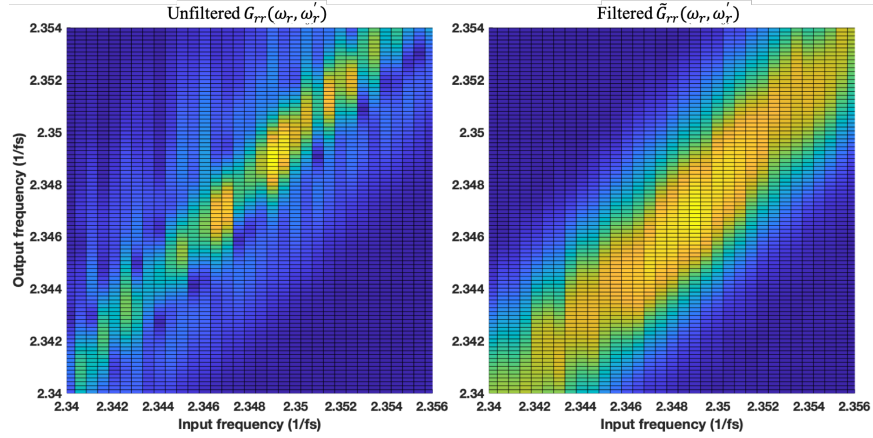


Figure 4.26. Experimental reconstruction of the IR Green transfer map $G_{rr}(\omega_r, \omega_r')$ of the QPG for zeroth order HG pump pulse at 0.32 mW. The unfiltered $G_{rr}(\omega_r, \omega_r')$ (left) when the pump is switched on. By subtracting the no-pump transfer map $\Delta(\omega_r, \omega_r')$ in Fig. 4.19, we obtain the filtered $\tilde{G}_{rr}(\omega_r, \omega_r')$ (right).

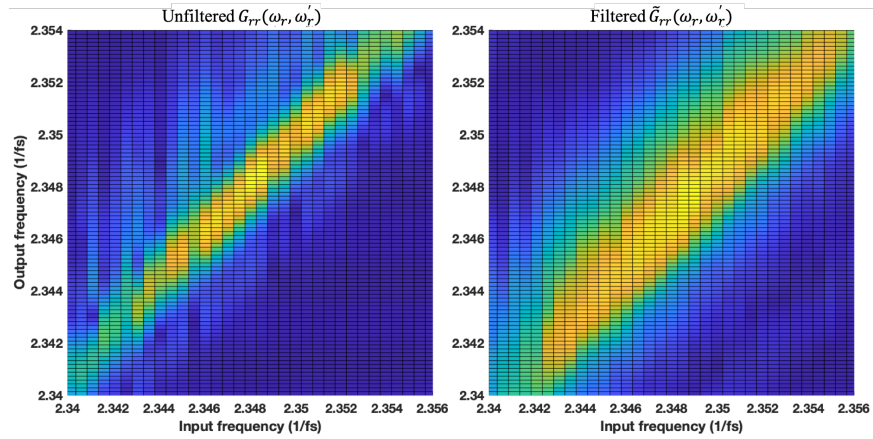


Figure 4.27. Experimental reconstruction of the IR Green transfer map $G_{rr}(\omega_r, \omega_r')$ of the QPG for first order HG pump pulse at 0.32 mW. The unfiltered $G_{rr}(\omega_r, \omega_r')$ (left) when the pump is switched on. By subtracting the no-pump transfer map $\Delta(\omega_r, \omega_r')$ in Fig. 4.19, we obtain the filtered $\tilde{G}_{rr}(\omega_r, \omega_r')$ (right).

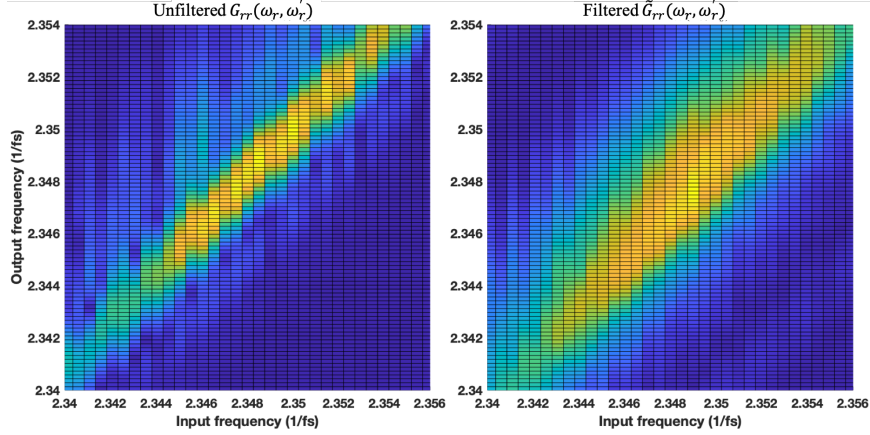


Figure 4.28. Experimental reconstruction of the IR Green transfer map $G_{rr}(\omega_r, \omega'_r)$ of the QPG for second order HG pump pulse at 0.32 mW. The unfiltered $G_{rr}(\omega_r, \omega'_r)$ (left) when the pump is switched on. By subtracting the no-pump transfer map $\Delta(\omega_r, \omega'_r)$ in Fig. 4.19, we obtain the filtered $\tilde{G}_{rr}(\omega_r, \omega'_r)$ (right).

transmitted in the red frequency band and gets converted in the blue frequency band which is expected from the QPG action.

	τ_0	τ_1	τ_2
Pump HG0	0.518	0.866	0.961
Pump HG1	0.941	0.556	0.903
Pump HG2	0.948	0.897	0.605

Table 4.1. Transmission coefficients τ_n for the leading three Schmidt modes of $\tilde{G}_{rr}(\omega_r, \omega'_r)$ with respect to the leading three HG pump modes with strong pump power of 2.92 mW.

Assuming unitarity of the QPG, we are able to calculate the conversion efficiencies directly from

$$\text{CE} = |\rho_n|^2 = 1 - |\tau_n|^2. \quad (4.8)$$

The conversion efficiencies for the first three modes with respect to the first three HG modes of the pump pulse are shown in Fig. 4.29.a. The difference between the conversion efficiencies obtained from our CTMT-SI technique and the conversion efficiencies measured directly from the QPG is shown in Fig. 4.29.b. As can be observed, the difference between the conversion efficiencies obtained from our CTMT-SI technique and the conversion efficiencies measured directly is within

	τ_0	τ_1	τ_2
Pump HG0	0.651	0.962	0.972
Pump HG1	0.977	0.682	0.947
Pump HG2	0.979	0.929	0.733

Table 4.2. Transmission coefficients τ_n for the leading three Schmidt modes of $\tilde{G}_{rr}(\omega_r, \omega'_r)$ with respect to the leading three HG pump modes with moderate pump power of 0.98 mW.

	τ_0	τ_1	τ_2
Pump HG0	0.889	0.990	0.995
Pump HG1	0.974	0.918	0.995
Pump HG2	0.994	0.990	0.934

Table 4.3. Transmission coefficients τ_n for the leading three Schmidt modes of $\tilde{G}_{rr}(\omega_r, \omega'_r)$ with respect to the leading three HG pump modes with weak pump power of 0.32 mW.

$\pm 2\%$ which provides confidence that the measured $\tilde{G}_{rr}(\omega_r, \omega'_r)$ is accurate. Figs. 4.30 and 4.31 show the calculated CE from our CTMT-SI method in panels (a) and the difference between conversion efficiencies of CTMT-SI against directly measured CE of the QPG in panels (b). As can be easily observed, in case of moderate pump power of 0.98 mW, the agreement between the directly-measured CE and that calculated from the CTMT-SI method is still within a reasonable margin of 3%. Reducing the pump power to 0.3 mW, the amount of discrepancy becomes noticeable, 8%, and this can be attributed to the fact that the spectral bandwidths of the filtered $\tilde{G}_{rr}(\omega_r, \omega'_r)$ and that of the no-pump case $\Delta(\omega_r, \omega'_r)$ are comparable to each other which can be observed in the right panels of Figs. 4.26 — 4.28. This means that the approximation introduced in Eq. (3.27) breaks down in the weak conversion limit giving rise to noticeable discrepancy. Silberhorn group [Ans+18b] introduced a tomography method, that relied on direct measurements of conversion probabilities, that works in weak conversion limit. The method they introduced has challenges in strong conversion limit since the Schmidt modes are distorted due to the time-ordering effects in the strong coupling limit. Therefore, the proposed method in the present work complements their work with the additional benefit of extracting the Schmidt modes of the transfer maps. Future improvements need to be devised to account for the issues that arise from the finite time sampling as well

as the time-dependent loss introduced in the system components.

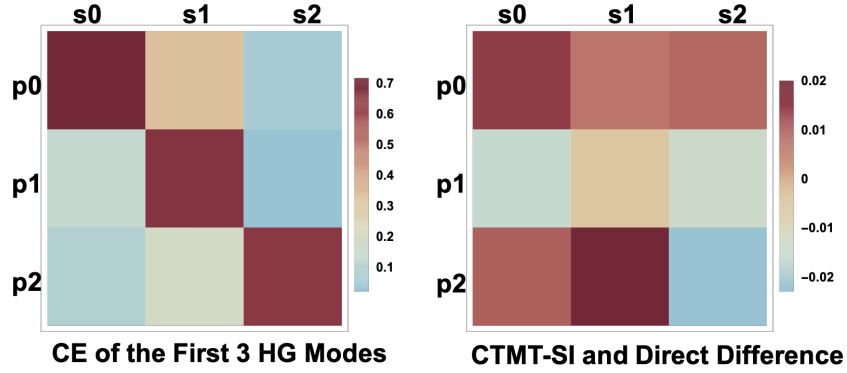


Figure 4.29. (a) CE of the first 3 Schmidt modes for the first 3 HG modes of the pump deduced from our CTMT-SI technique with strong pump power of 2.92 mW. (b) The difference between conversion efficiencies of CTMT-SI against directly measured CE of the QPG showing good agreement within $\pm 2\%$.

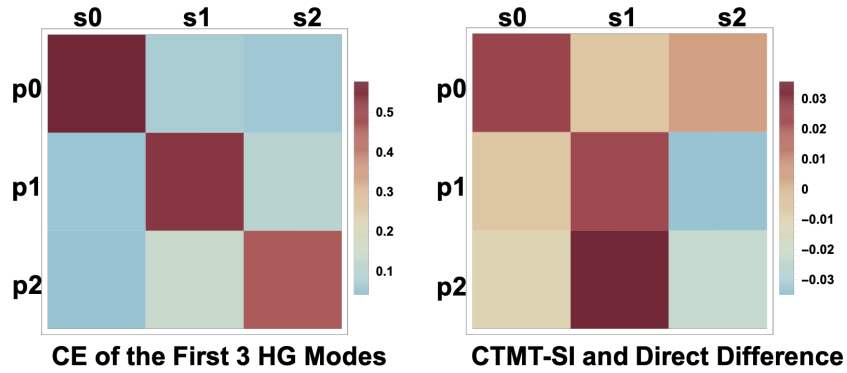


Figure 4.30. (a) CE of the first 3 Schmidt modes for the first 3 HG modes of the pump deduced from our CTMT-SI technique with moderate pump power of 0.98 mW. (b) The difference between conversion efficiencies of CTMT-SI against directly measured CE of the QPG showing reasonable agreement within $\pm 3\%$.

Schmidt Modes

The first three Schmidt modes of the QPG, when the pump is set to zeroth-order HG mode and 2.92 mW, are shown in Fig. 4.32 along with the HG modes

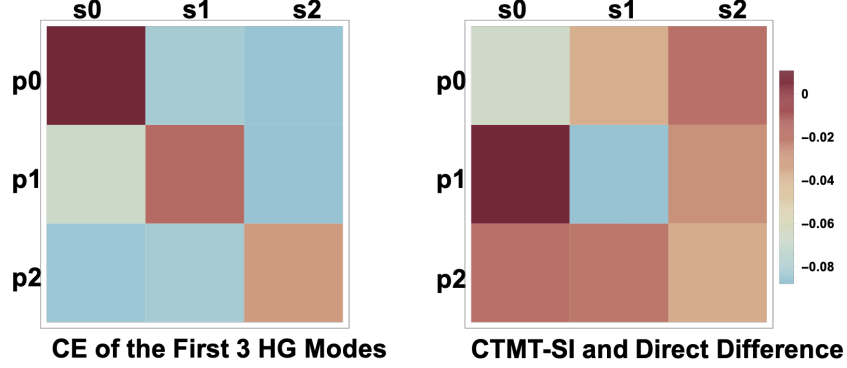


Figure 4.31. (a) CE of the first 3 Schmidt modes for the first 3 HG modes of the pump deduced from our CTMT-SI technique with weak pump power of 0.32 mW. (b) The difference between conversion efficiencies of CTMT-SI against directly measured CE of the QPG showing noticeable error of approximately 8%.

for reference. The overlap or the direct product of them is plotted in Fig. 4.33 for zeroth- and first-order Schmidt and HG modes. Since there is little difference between the HG and Schmidt modes as can be observed in Fig. 4.32, we would expect that the CE for these modes to be nearly the same indicating that CE of Schmidt modes does not change noticeably especially at low pump powers. To verify that, we measure the CE for both HG and Schmidt modes when the pump is set to zeroth- and first-order HG modes respectively. Fig. 4.34 shows the CE versus $\bar{\gamma}$ for both zeroth and first HG and Schmidt modes when the pump is set to zeroth- and first-order HG modes. Note the increase in CE at high pump powers for the mode orthogonal to the pump, and the plateau in CE for the target mode which is attributed to the distortion of modes due to time ordering effects of the interaction Hamiltonian [Red17].

To verify the temporal shapes of the Schmidt modes to ensure that the proposed CTMT-SI works reasonably well we need to measure them by defining the SLM mask according to the calculated Schmidt modes from the SVD of the reconstructed transfer map $\tilde{G}_{rr}(\omega_r, \omega'_r)$. However, since their time duration is long ($\tau \sim 500$ fs), it is somewhat simpler to measure them in the spectral domain. The spectral resolution of the spectrometer (0.2 nm) cannot however show the differences between Schmidt modes and HG modes so I use Spectral Interferometry (SI) once again to measure the Schmidt modes. Fig. 4.35 shows the spectral shapes of

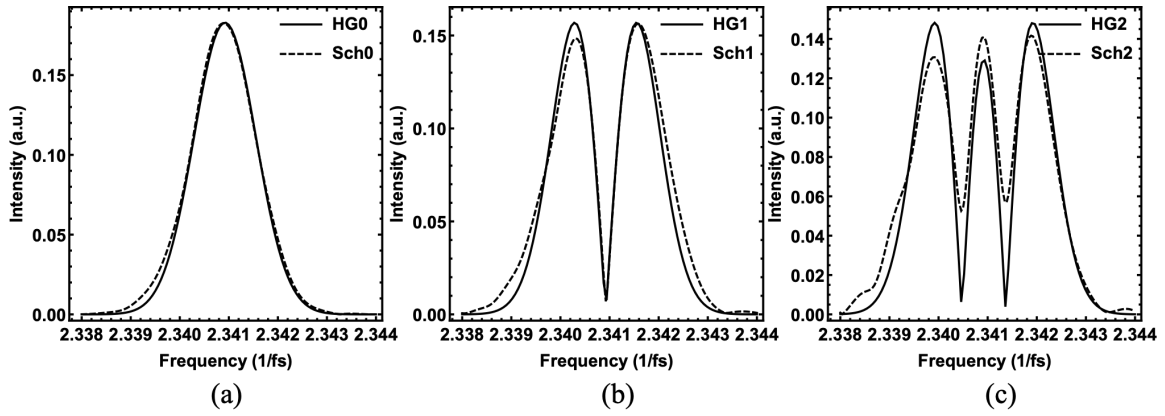


Figure 4.32. Zeroth (a), first (b) and second (c) Schmidt modes of the Green transfer map $G_{rr}(\omega_r, \omega_r')$ reconstructed from CTMT-SI plotted with HG modes for clarification

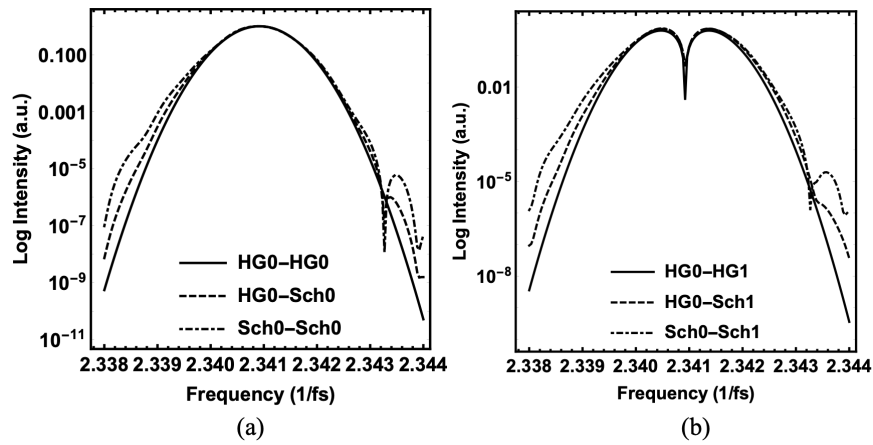


Figure 4.33. The overlap between zeroth (a) and first (b) Schmidt modes and HG modes.

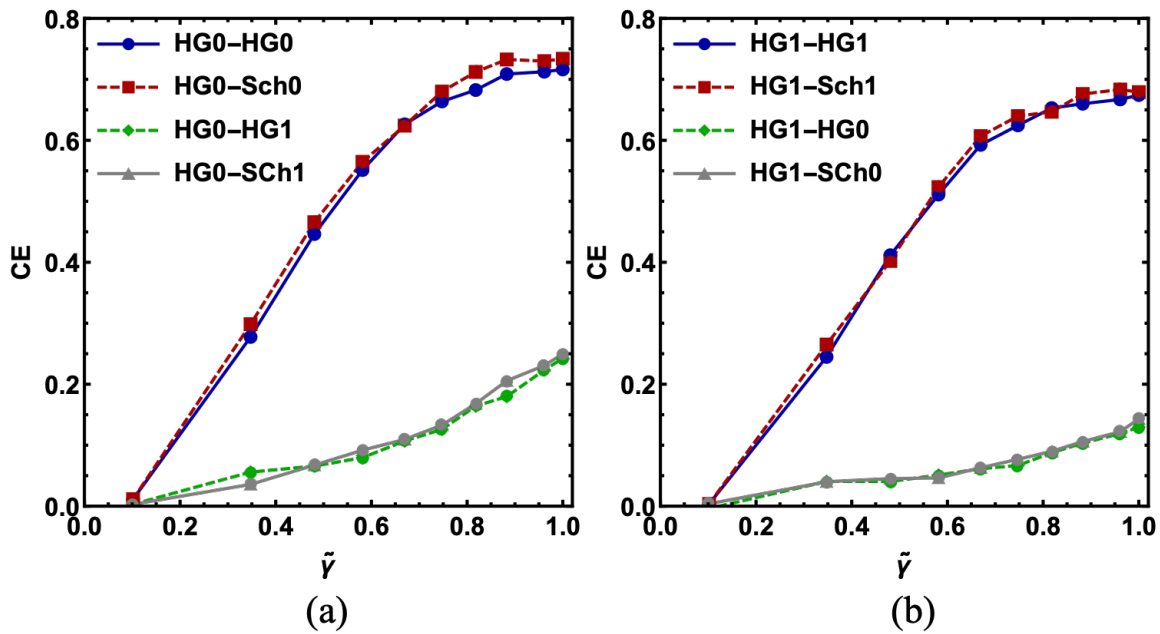


Figure 4.34. CE vs $\bar{\gamma}$ for zeroth (a) and first (b) HG pump and both HG and Schmidt signal modes.

the first three Schmidt modes.

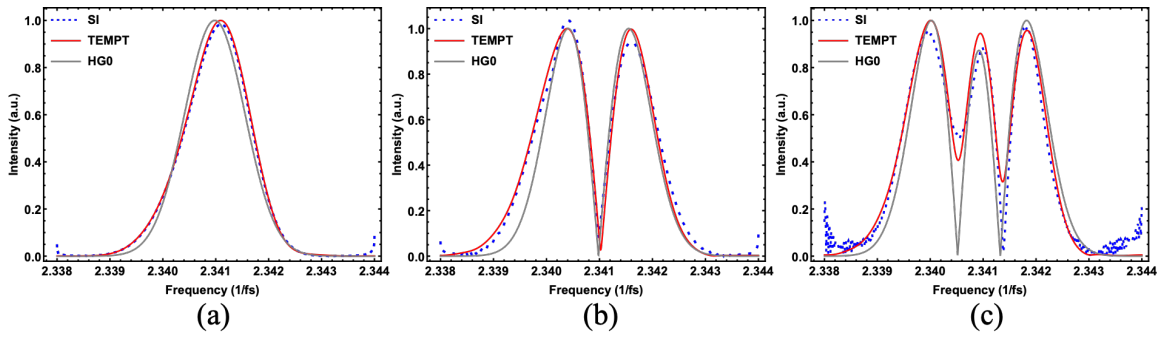


Figure 4.35. Spectral interferometric measurement (blue) of the zeroth order (a), first order (b) and second order (c) Schmidt modes generated by the pulse shaper and obtained from our CTMT-SI technique (red) and respective HG modes (Gray) shown for reference.

CHAPTER 5

FUTURE DIRECTIONS

In this chapter, I propose two experiments to characterize the QPG in the blue spectral region. The first experiment is proposed to reconstruct the Green transfer map $G_{br}(\omega_b, \omega'_r)$ of the QPG in the blue spectral region and follows similarly the method of the IR-CTMT-SI of the first experiment discussed in Chapter 4.

The second experiment I propose is what I call DFG-SPIDER, which directly characterizes the temporal structure of the output TMs in the blue spectral region, the missing piece of information from the IR-CTMT-SI experiment. The naming stems from using a similar technique to SPIDER [IW99] in characterizing ultra-short pulses while employing DFG to access the temporal structure of the TMs in the blue spectral region.

5.1 Blue Part: $G_{br}(\omega_b, \omega'_r)$

I provide two schemes for this experiment based on second harmonic generation (SHG-CTMT-SI) as shown in Fig. 5.1 and on difference frequency generation (DFG-CTMT-SI) as shown in Fig. 5.2 respectively. Either SHG-CTMT-SI or DFG-CTMT-SI are expected to provide information about the temporal structure of input and output TMs in the blue spectral region as well as conversion probabilities (and transmission probabilities) and the temporal structure of the input TMs in the IR spectral region if the QPG were to perform in reverse action through DFG instead of SFG where the signal is in the blue spectral frequency band and the downconverted output is in the IR spectral frequency band. This information can be calculated from the reconstruction of the transfer map

$$G_{br}(\omega_b, \omega_r) = \sqrt{\frac{2}{\pi}} \frac{\tilde{S}_{\text{blue}}^{(+)}(\omega_b, \nu) e^{i\omega_b \tau}}{A^*(\omega'_r) A_{SHG}(\omega_b)}, \quad \text{SHG} \quad (5.1)$$

$$G_{br}(\omega_b, \omega'_r) = \sqrt{\frac{2}{\pi}} \frac{\tilde{S}_{\text{red}}^{(+)}(\omega_r, \mu) e^{i\omega_b \tau}}{A^*(\omega'_r) A_{DFG}(\omega_b)}, \quad \text{DFG} \quad (5.2)$$

where $\nu = \omega_b - \omega'_r$, $\mu = \omega_r - \omega'_r$ and τ is the fixed time delay. In Eqs. (5.1) and (5.2), the $\tilde{S}_{\text{blue}}^{(+)}(\omega_b, \nu)$ and $\tilde{S}_{\text{red}}^{(+)}(\omega_r, \mu)$ are the spectral measurements in the blue (see Fig. 5.1) and the red (see Fig. 5.2) interferometers respectively. We perform the same algorithm outlined in Fig. 3.6 to extract the transfer map $G_{br}(\omega_b, \omega_r)$.

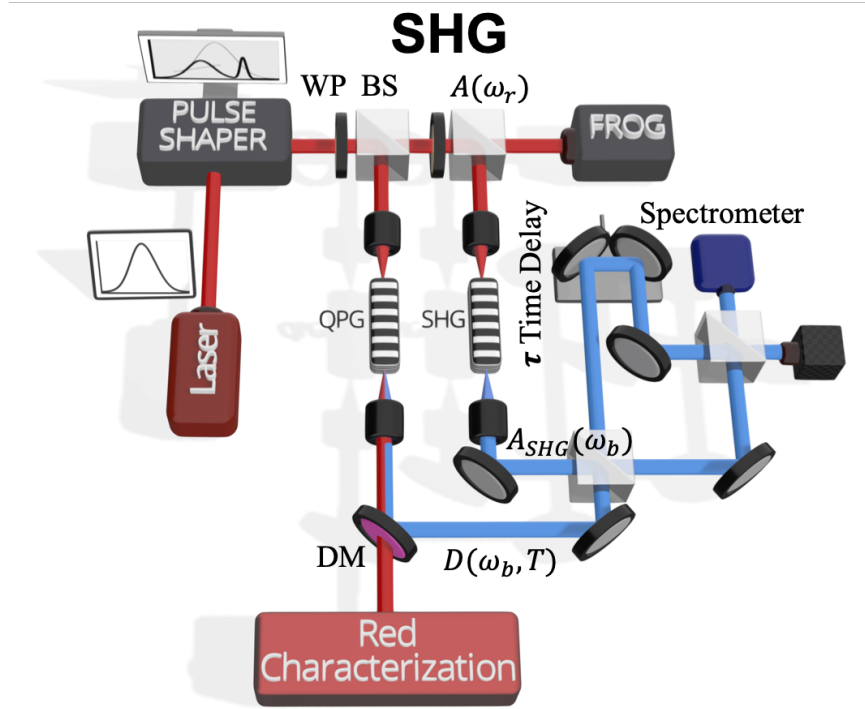


Figure 5.1. SHG-CTMT-SI schematic proposed setup. The QPG is probed by a probe pulse $A(\omega_r, T)$ and the upconverted output blue is $D(\omega_b, T) = \int d\omega'_r G_{br}(\omega_b, \omega'_r) A(\omega_r, T)$ which is interfered with a frequency-doubled replica of the reference pulse $A_{SHG}(\omega_b)$ in the blue interferometer to extract $G_{br}(\omega_b, \omega_r)$.

Both experimental schemes come with their own technical challenges. The SHG experiment shown in Fig. 5.1 depends on performing spectral interferometry in the blue spectral region. The spectral fringes are oscillating at a frequency $\nu = \omega_b - \omega_r \sim 2.343 \times 10^3$ THz which is impossible to resolve in current commercial spectrometers. In order to dodge around this problem, we propose to build Michelson interferometer and do a double pass of the time delay τ with a highly sensitive and stable translation stage with steps of ~ 5 nm in order to scan over the spectral range of the bandwidth of the SHG probe and output of the QPG.

The DFG-Blue experiment shown in Fig. 5.2 is much easier to build and characterize since the DFG signal is in the IR spectral region which is accessible to resolve the spectral fringes in the IR with commercial spectrometers. However, special attention should be paid to compensate for the DFG action of the DFG wave-

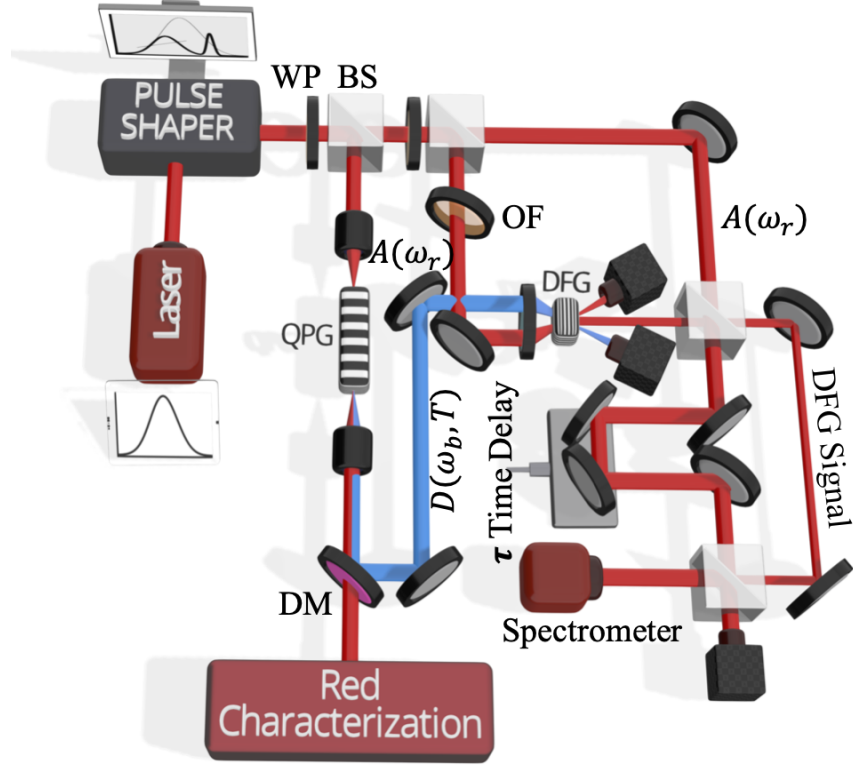


Figure 5.2. DFG-CTMT-SI schematic proposed setup. The QPG is probed by a probe pulse $A(\omega_r, T)$ and the upconverted output blue is $D(\omega_b, T) = \int d\omega'_r G_{br}(\omega_b, \omega'_r) A(\omega_r, T)$ which is coupled with a replica of the reference pulse $A(\omega_r)$ in the DFG waveguide. The DFG signal $A_{DFG}(\omega_r, T)$ is then interfered with a replica of the reference pulse $A(\omega_r)$ in the red interferometer to extract $G_{br}(\omega_b, \omega_r)$.

uide in the analysis of extracting the Green transfer map $G_{br}(\omega_b, \omega'_r)$. This means that the DFG waveguide must be well characterized, that is its phase-matching function is well identified.

Since the only missing information of the characterization of the QPG in the IR spectral region discussed in Chapter 4 is the Schmidt modes of the converted output in the blue spectral region, I propose an experiment that directly characterizes the blue output which I discuss in the following section. It is worth mentioning that, this experiment which I call Blue-DFG-SPIDER is considered as a standalone experiment that is used in characterizing ultrashort pulses in the blue spectral region.

5.2 Temporal-Mode Characterization (Blue)

To characterize the output blue TM from the QPG which has a significantly more narrow bandwidth compared to the signal and pump fields. I propose to use the nonlinear optical process, difference frequency generation (DFG) between the output blue of the QPG and an auxiliary reference field. Assume we have an unknown blue pulse (as the output blue of the QPG) with an electric field component $E_B(t) = \mathcal{E}_B(t)e^{-i\omega_B t}$, where $\mathcal{E}_B(t) = |\mathcal{E}_B(t)|e^{i\phi(t)}$ is the slowly varying envelope with $\phi(t)$ is its phase, ω_B is its angular frequency and with a pulse duration τ_B . A known reference is a two-colored two short (delta-function like) pulses whose electric field is expressed as

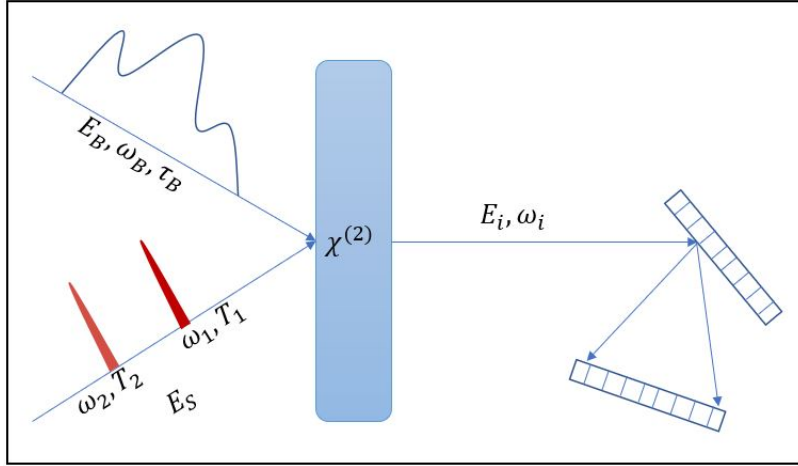
$$E_S(t) = \sum_{j=1,2} \mathcal{E}_S(t - T_j)e^{-i\omega_j t}, \quad (5.3)$$

where $\mathcal{E}_S(t - T_j) = |\mathcal{E}_S(t - T_j)|e^{i\Phi_j(t)}$ are delta-function like amplitudes with phases Φ_j and frequencies ω_j for $j = 1, 2$. Note that the duration of the blue pulse is assumed to be much longer than that of the red reference pulses. Both fields are interacting in a nonlinear optical crystal of $\chi^{(2)}$ nonlinearity as shown in Fig. (5.3). In the thin-crystal limit where the phase-matching bandwidth is broad, the difference frequency field, or idler, is given by the product of the strong field and the blue field,

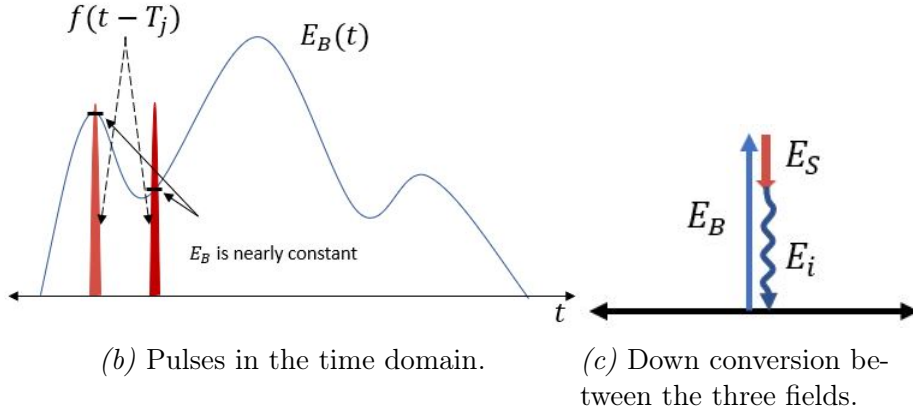
$$\begin{aligned} E_i(t) &\propto E_B(t)E_S^*(t), \\ &= \sum_{j=1,2} \mathcal{E}_B(t)\mathcal{E}_S^*(t - T_j)e^{-i(\omega_B - \omega_j)t}. \end{aligned} \quad (5.4)$$

Taking the Fourier transform of Eq. (5.4) gives the spectral amplitude of the idler field,

$$\begin{aligned} \tilde{E}_i(\omega) &= \int dt E_i(t)e^{i\omega t}, \\ &= \sum_{j=1,2} \int dt \mathcal{E}_B(t)\mathcal{E}_S^*(t - T_j)e^{-i(\omega_B - \omega_j - \omega)t}, \\ &\approx \sum_{j=1,2} \mathcal{E}_B(T_j) \int dt \mathcal{E}_S^*(t - T_j)e^{-i(\omega_B - \omega_j - \omega)t}, \\ &= \sum_{j=1,2} \mathcal{E}_B(T_j) \int dx_j \mathcal{E}_S^*(x_j)e^{-i(\omega_B - \omega_j - \omega)(x_j + T_j)}, \end{aligned}$$



(a) Schematic diagram.



(b) Pulses in the time domain.

(c) Down conversion between the three fields.

Figure 5.3. DFG Spider.

$$= \sum_{j=1,2} \mathcal{E}_B(T_j) \tilde{\mathcal{E}}_S^*(\omega_B - \omega_j - \omega) e^{-i(\omega_B - \omega_j - \omega)T_j}. \quad (5.5)$$

where $x_j = t - T_j$ and $\tilde{\mathcal{E}}_S^*(\omega) = [\int dx \mathcal{E}_S(x) e^{-i\omega x}]^*$. We define the functions

$$F_j(T_j, \omega) = \mathcal{E}_B(T_j) \tilde{\mathcal{E}}_S^*(\omega_B - \omega_j - \omega), \quad (5.6)$$

then the energy spectrum of the idler field is given as

$$\begin{aligned} S_i(T_1, T_2; \omega) &= \langle |\tilde{E}_i(\omega)|^2 \rangle, \\ &= \langle \left| \sum_{j=1,2} F_j(T_j, \omega) e^{-i(\omega_B - \omega_j - \omega)T_j} \right|^2 \rangle, \end{aligned}$$

$$\begin{aligned}
&= \langle |F_1(T_1, \omega)|^2 \rangle + \langle |F_2(T_2, \omega)|^2 \rangle \\
&\quad + 2 \Re \langle [F_1^*(T_1, \omega) F_2(T_2, \omega)] e^{i(\omega_B - \omega_1 - \omega)T_1} e^{-i(\omega_B - \omega_2 - \omega)T_2} \rangle, \\
&= \langle |F_1(T_1, \omega)|^2 \rangle + \langle |F_2(T_2, \omega)|^2 \rangle \\
&\quad + 2 \Re \langle [F_1^*(T_1, \omega) F_2(T_2, \omega)] e^{i(\bar{\omega}_i - \omega)(T_1 - T_2)} e^{-i\Delta\omega(T_1 + T_2)} \rangle, \quad (5.7)
\end{aligned}$$

where $\Delta\omega = \frac{1}{2}(\omega_1 - \omega_2)$, $\bar{\omega}_S = \frac{1}{2}(\omega_1 + \omega_2)$, $\bar{\omega}_i = \omega_B - \bar{\omega}_S$ and the brackets $\langle \cdot \rangle$ denote the first-order coherence function. We change the variables $\Delta\omega_2 = \omega - \bar{\omega}_i$, $\delta\omega_1 = \Delta\omega_2 + \Delta\omega$ and $\delta\omega_2 = \Delta\omega_2 - \Delta\omega$, then we obtain

$$\begin{aligned}
S_i(T_1, T_2; \omega) &= \langle |F_1(T_1, \omega)|^2 \rangle + \langle |F_2(T_2, \omega)|^2 \rangle \\
&\quad + 2 \Re \langle [F_1^*(T_1, \omega) F_2(T_2, \omega)] e^{-i\delta\omega_1 T_1} e^{i\delta\omega_2 T_2} \rangle. \quad (5.8)
\end{aligned}$$

We now take the Fourier Transform of Eq. (5.8) with respect to time T_1 , therefore

$$\begin{aligned}
S_i(\Omega, T_2; \omega) &= \int dT_1 S_i(T_1, T_2; \omega) e^{i\Omega T_1}, \\
&= \langle |F_1(\Omega, \omega)|^2 \rangle + \langle |F_2(T_2, \omega)|^2 \rangle \\
&\quad + \langle \mathcal{E}_B^*(\Omega - \delta\omega_1) \mathcal{E}_B(T_2) \mathcal{E}_S(-\delta\omega_1) \mathcal{E}_S^*(\delta\omega_2) \rangle e^{i\delta\omega_2 T_2} \\
&\quad + \langle \mathcal{E}_B(\Omega + \delta\omega_1) \mathcal{E}_B^*(T_2) \mathcal{E}_S^*(-\delta\omega_1) \mathcal{E}_S(\delta\omega_2) \rangle e^{-i\delta\omega_2 T_2}. \quad (5.9)
\end{aligned}$$

The first two terms of Eq. (5.9) represent the DC component of the spectrum while the last two terms represent the AC component with the third (fourth) term representing the negative (positive) sideband. In order to filter out the DC and negative AC components, we apply a fourth-order super Gaussian function shifted by $\delta\omega_1$ and with a spectral bandwidth of $\delta\omega_1/2$. Therefore,

$$FS_i(\Omega, T_2; \omega) = e^{-\ln(2) \left[\frac{2(\Omega - \delta\omega_1)}{\delta\omega_1/2} \right]^4} S_i(\Omega, T_2; \omega). \quad (5.10)$$

Substituting Eq. (5.9) into Eq. (5.10) and rearranging we get

$$\langle \mathcal{E}_B(\Omega + \delta\omega_1) \mathcal{E}_B^*(T_2) \rangle = \frac{FS_i(\Omega, T_2; \omega) e^{i\delta\omega_2 T_2}}{\langle \mathcal{E}_S^*(-\delta\omega_1) \mathcal{E}_S(\delta\omega_2) \rangle}. \quad (5.11)$$

We then take the Inverse Fourier Transform of Eq. (5.11) with respect to Ω ,

$$\langle \mathcal{E}_B(T_1) \mathcal{E}_B^*(T_2) \rangle e^{i\delta\omega_1 T_1} = \frac{FS_i(T_1, T_2; \omega) e^{i\delta\omega_2 T_2}}{\langle \mathcal{E}_S^*(-\delta\omega_1) \mathcal{E}_S(\delta\omega_2) \rangle}, \quad (5.12)$$

which contains all the information needed to retrieve amplitude and phase of the blue ultrashort pulse. The phase difference is therefore obtained from

$$\phi(T_1) - \phi(T_2) = \arg \left[\frac{FS_i(T_1, T_2; \omega) e^{i\delta\omega_2 T_2}}{\langle \mathcal{E}_S^*(-\delta\omega_1) \mathcal{E}_S(\delta\omega_2) \rangle} \right] - \delta\omega_1 T_1. \quad (5.13)$$

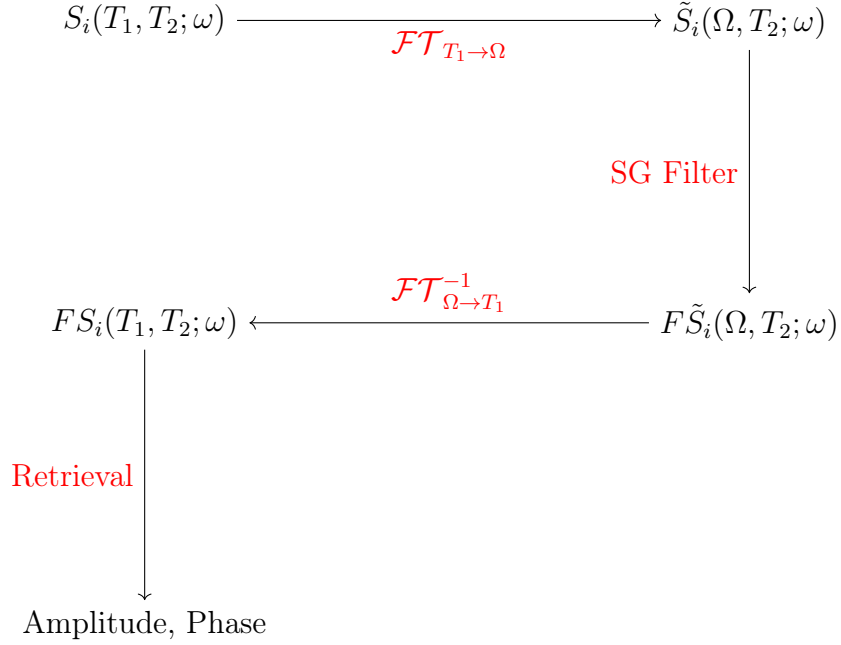


Figure 5.4. Layout of the reconstruction algorithm.

In this algorithm, we probe the blue pulse by scanning the time delays, T_1 and T_2 back and forth which maps out the first-order coherence function $\langle \mathcal{E}_B^*(T_2) \mathcal{E}_B(T_1) \rangle$. The spectral data consists of spectra on a 2D array for both time delays T_1 and T_2 . If we slice up the space horizontally or vertically in the spectral domain, any slice of spectral data can be used to retrieve the amplitude and phase of the unknown blue pulse following the algorithm outlined in Fig. 5.4.

DFG SPIDER Proposed Setup

A schematic representation of the proposed setup is shown in Fig. (5.5). We have a femtosecond pulsed Ti-Sapphire laser whose generated pulse is split into two parts. The first part is used for the QPG setup that generates the blue pulse to be characterized and the second part is used to generate the reference probe pulses. We use optical filters to carve out the Ti:Sapphire laser spectrum as shown in Fig. (5.6). We then combine the two arms with delay lines T_1 (scanned) and T_2 (fixed) to form the strong field, Eq. (5.3) that interacts with the blue field within a $\chi^{(2)}$ nonlinear crystal.

The data inversion algorithm is shown in Fig. (5.4). We measure the spectrum

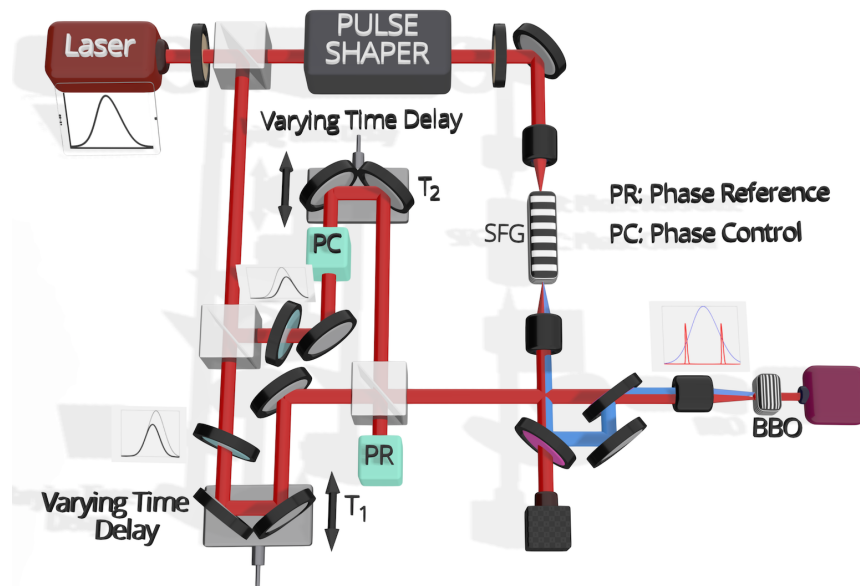


Figure 5.5. DFG-SPIDER Schematic proposed setup.

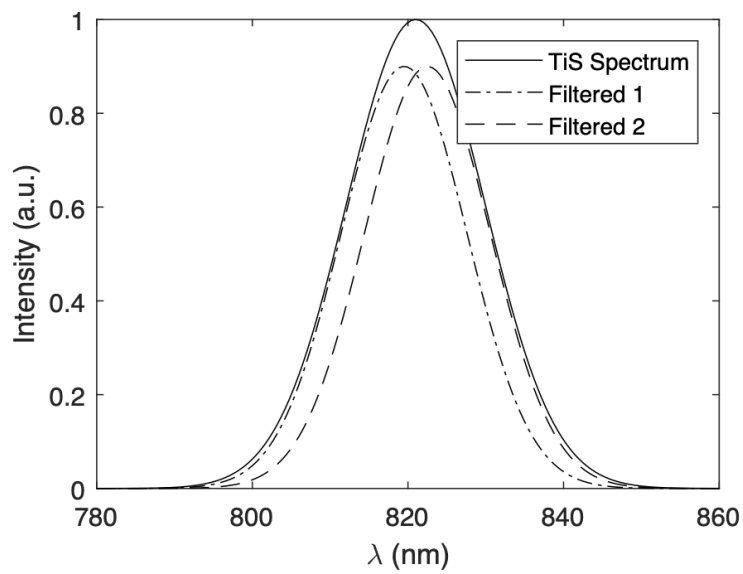


Figure 5.6. Spectrum of the Ti:Sapphire laser (solid) and the spectra of the two reference pulses used to characterize the blue unknown pulse.

vs. scanning delay line T_1 while delay line T_2 is fixed. We then take the Fourier Transform with respect to delay line T_1 that has components centered near $\Omega \sim \pm\delta\omega_1$ as well as a component at $\Omega = 0$. The component at $\Omega = 0$ is the Fourier transform of the DC portion of the interferogram while the sideband components near $\Omega \sim \pm\delta\omega_1$ arise from the Fourier transform of the AC portions of the interferogram. For sufficiently large $\delta\omega_1$, the $\Omega = 0$ and $\pm\delta\omega_1$ components are well separated in frequency domain and, as a result, the DC and negative AC components can be removed by filtering. The argument of the filtered signal is the temporal phase difference. Figs. 5.7 and 5.8 show examples of numerical simulations of the reconstruction zeroth- and first-order HG pulses with 200 fs temporal duration respectively.

To show the validity of our proposed technique to characterize temporal modes in the blue spectral region, we show numerical simulations of the reconstruction of zeroth-order HG (Fig. 5.7) and first-order HG (Fig. 5.8) pulses.

Numerical Simulations

In conclusion, we have presented a full scheme for characterizing QPG output pulses in the blue spectral region based on DFG in which two well-characterized ultrashort pulses, frequency-sheared with respect to each other sample the test pulse in a $\chi^{(2)}$ crystal. Our algorithm laid out in Fig. 5.4 shows that we can retrieve both the amplitude and phase of the temporal mode to be characterized from Eqs. (5.12) and (5.13).

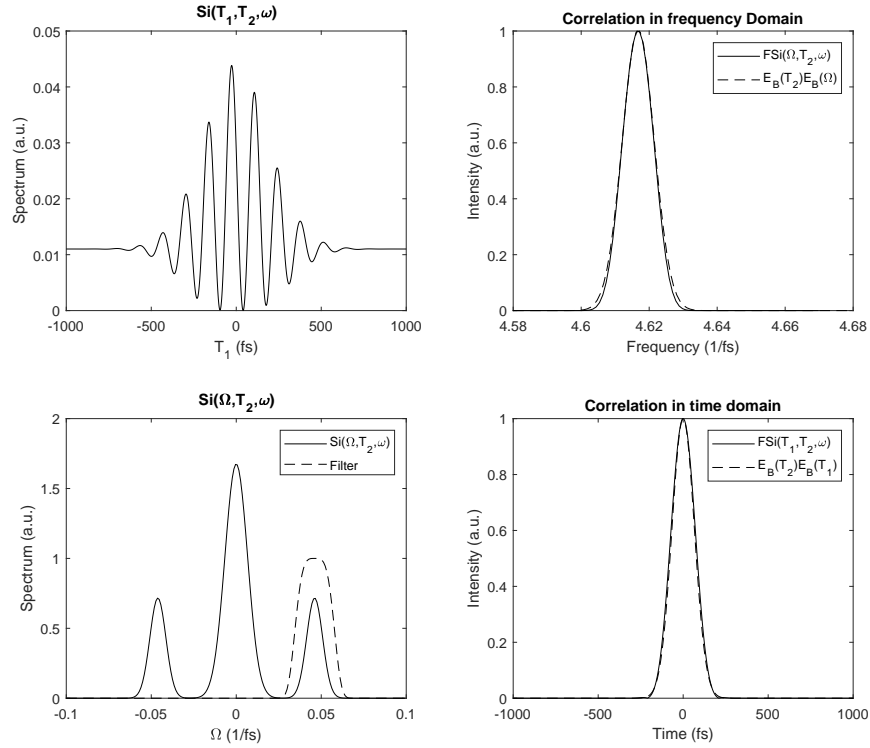


Figure 5.7. Numerical simulation of the steps of reconstructing an ultrashort pulse in the blue spectral region of a zeroth-order HG TM. The top left plot shows the spectrum $S_i(T_1, T_2; \omega)$ while scanning the time delay T_1 and fixing T_2 . The bottom left is the Fourier transform of $S_i(T_1, T_2; \omega)$ with respect to T_1 which shows the DC signal with the AC sideband signals. The top left shows the correlation $\langle \mathcal{E}_B(T_2) \mathcal{E}_B(\Omega) \rangle$ compared to the filtered spectral measurement $FS_i(\Omega, T_2; \omega)$ in the frequency domain while the bottom right shows the same in the time domain.

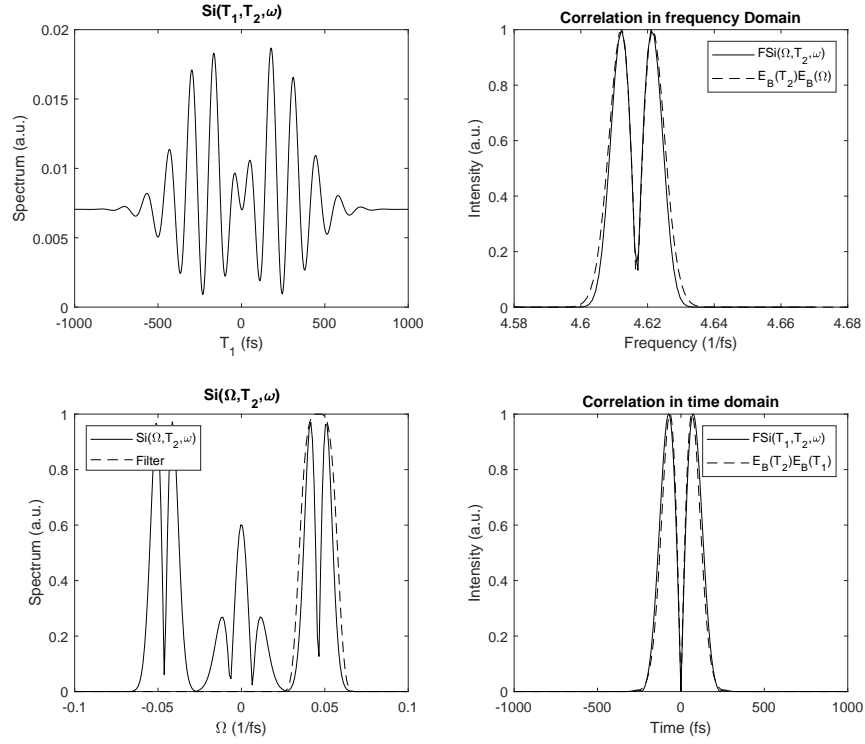


Figure 5.8. Numerical simulation of the steps of reconstructing an ultrashort pulse in the blue spectral region of a first-order HG TM. The top left plot shows the spectrum $S_i(T_1, T_2; \omega)$ while scanning the time delay T_1 and fixing T_2 . The bottom left is the Fourier transform of $S_i(T_1, T_2; \omega)$ with respect to T_1 which shows the DC signal with the AC sideband signals. The top left shows the correlation $\langle \mathcal{E}_B(T_2) \mathcal{E}_B(\Omega) \rangle$ compared to the filtered spectral measurement $FS_i(\Omega, T_2; \omega)$ in the frequency domain while the bottom right shows the same in the time domain.

CHAPTER 6

CONCLUSION

In this work, I introduced a method to characterize temporal-mode transformations (TMTs) specifically QPGs. The main idea of the presented method relies upon spectral interferometry in which a short probe pulse $A(\omega_r)$ is time delayed over a time scan T and is incident on a QPG. The output pulse $C(\omega_r, T)$ is then interfered with a reference pulse which is a replica of $A(\omega_r)$. Through Fourier analysis, I was able to reconstruct the Green transfer map of the transmitted signal of the QPG $\tilde{G}_{rr}(\omega_r, \omega'_r)$ from which information about transmission and conversion probabilities along with the Schmidt modes were retrieved. I presented experimental data showcasing the validity of the proposed method especially in the strong and moderate conversion limits. The values of conversion efficiencies between different HG modes deduced from our proposed method, CTMT-SI, agree with the directly-measured values proving the success of our method in characterizing QPGs in the strong and moderate conversion limits which has not been done prior to the proposed method.

However, in the weak conversion limit, it becomes challenging to retrieve reliable calculations since the spectral bandwidth of the transfer map $\tilde{G}_{rr}(\omega_r, \omega'_r)$ is comparable to the spectral broadening of the transfer map in case of no pump $\Delta(\omega_r, \omega'_r)$.

I also proposed an experiment in order to reconstruct the transfer map in the up-converted spectral region and provide two schemes based on SHG and DFG respectively. Either SHG-TEMPT or DFG-TEMPT are expected to provide information about the temporal structure of input and output TMs in the up-converted spectral region as well as conversion probabilities (and transmission probabilities) and the temporal structure of the input TMs in the IR spectral region if the QPG were to perform in reverse action.

The third experiment I proposed is what I call DFG-SPIDER which directly characterizes the temporal structure of the output TMs in the up-converted (blue) spectral region, the missing piece of information from the IR-TEMPT experiment. The naming stems from using a similar technique to SPIDER in characterizing ultrashort pulses while employing DFG to access the temporal structure of the TMs in the up-converted (blue) spectral region. I presented numerical simulations reconstructing TMs from the proposed method showing the validity of it.

The main lessons learnt have been to look for solutions to advanced problems (characterizing QPGs) and to look for approximate solutions when exact ones prove elusive. The problem of characterizing QPGs is an important one for quantum information applications. Methods presented earlier through direct measurement of conversion efficiencies provide an *incomplete* solution of the problem of characterizing QPGs. I used spectral interferometry, a well studied technique, and developed a method to provide a complete framework of characterizing QPGs which can be applied to other devices that manipulate temporal modes.

REFERENCES CITED

- [All+92] L. Allen et al., *Orbital angular momentum of light and the transformation of Laguerre-Gaussian laser modes*, Phys. Rev. A **45** (1992), 8185, DOI: 10.1103/PhysRevA.45.8185.
- [Ans+17] V. Ansari et al., *Temporal-mode measurement tomography of a quantum pulse gate*, Phys. Rev. A **96** (2017), 063817.
- [Ans+18a] V. Ansari et al., *Tailoring nonlinear processes for quantum optics with pulsed temporal-mode encodings*, Optica **5** (2018), 534.
- [Ans+18b] V. Ansari et al., *Tomography and Purification of the Temporal-Mode Structure of Quantum Light*, Phys. Rev. Lett. **120** (2018), 213601.
- [Ans18] V. Ansari, *Quantum optics with temporal modes*, Ph.D. thesis, University of Paderborn, 2018.
- [Aru+19] F. Arute et al., *Quantum supremacy using a programmable superconducting processor*, Nature **574** (2019), no. 7779, 505–510.
- [AW04] M. A. Albota and F. N. C. Wong, *Efficient single-photon counting at 1550 nm by means of frequency upconversion*, Optics Letters **29** (2004), 1449–1451.
- [Ben+93] C. H. Bennett et al., *Teleporting an unknown quantum state via dual classical and Einstein-Podolsky-Rosen channels*, Phys. Rev. Lett. **70** (1993), no. 13, 1895–1899.
- [BK05] S. D. Barrett and P. Kok, *Efficient high-fidelity quantum computation using matter qubits and linear optics*, Phys. Rev. A **71** (2005), no. 6, 060310.
- [Blo+90] K. Blow et al., *Continuum fields in quantum optics*, Phys. Rev. A **42** (1990), 4102.
- [Bou+97] D. Bouwmeester et al., *Experimental quantum teleportation*, Nature **390** (1997), no. 6660, 575–579.
- [Boy08] R. Boyd, *Nonlinear Optics*, Third, Academic Press, 2008.
- [Bre+11] B. Brecht et al., *From quantum pulse gate to quantum pulse shaper—engineered frequency conversion in nonlinear optical waveguides*, New J. Phys. **13** (2011), 065029.

- [Bre+14] B. Brecht et al., *Demonstration of coherent time-frequency Schmidt mode selection using dispersion-engineered frequency conversion*, Phys. Rev. A **90** (2014), 030302.
- [Bre+15a] B. Brecht et al., *Photon Temporal Modes: A Complete Framework for Quantum Information Science*, Physical Review X **5** (2015), no. 4, 041017.
- [Bre+15b] B. Brecht et al., *Photon temporal modes: A complete framework for quantum information science*, Phys. Rev. X **5** (2015), 041017.
- [Bre14] B. Brecht, *Engineering ultrafast quantum frequency conversion*, Ph.D. thesis, University of Paderborn, 2014.
- [Bri+10] H. Briegel et al., *The Physics of Quantum Information*, Springer, Berlin, Heidelberg, 2010.
- [Bri+98] H. J. Briegel et al., *Quantum Repeaters: The Role of Imperfect Local Operations in Quantum Communication*, Phys. Rev. Lett. **81** (1998), no. 26, 5932–5935.
- [BW08] R. Blatt and D. Wineland, *Entangled states of trapped atomic ions*, Nature **453** (2008), no. 7198, 1008–1015.
- [CD03] G. Cerullo and S. De Silvestri, *Ultrafast optical parametric amplifiers*, Review of Scientific Instruments **74** (2003), 1–18.
- [CH13] L. Childress and R. Hanson, *Diamond NV Centers for Quantum Computing and Quantum Networks*, MRS Bulletin **38** (2013), no. 2, 134–138.
- [Cho+99] M.-H. Chou et al., *Multiple-channel wavelength conversion by use of engineered quasi-phase-matching structures in LiNbO₃ waveguides*, Optics letters **24** (1999), 1157–1159.
- [Chr+15] J. B. Christensen et al., *Temporal Mode Sorting Using Dual-Stage Quantum Frequency Conversion by Asymmetric Bragg Scattering*, Opt. Express **23** (2015), 23287.
- [Dir27] P. A. M. Dirac, *The Quantum Theory of the Emission and Absorption of Radiation*, Proceedings of the Royal Society of London. Series A, Containing Papers of a Mathematical and Physical Character **114** (1927), no. 767, 243–265, DOI: 10.1098/rspa.1927.0039.

- [DK98] C. Dorrer and I. Kang, *Characterization of ultrashort electromagnetic pulses*, Phys. Rev. A **58** (1998), no. 1, 740–755.
- [Doh+13] M. W. Doherty et al., *The nitrogen-vacancy colour centre in diamond*, Physics Reports **528** (2013), no. 1, 1–45.
- [DP09] G. M. D’Ariano and P. L. Presti, *Quantum State Estimation*, Lecture Notes in Physics, Springer, Berlin, 2009, 297.
- [DS13] M. H. Devoret and R. J. Schoelkopf, *Superconducting Circuits for Quantum Information: An Outlook*, Science **339** (2013), no. 6124, 1169–1174.
- [Dua+01] L. M. Duan et al., *Long-distance quantum communication with atomic ensembles and linear optics*, Nature **414** (2001), no. 6862, 413–418.
- [EBS11] A. Eckstein, B. Brecht, and C. Silberhorn, *A quantum pulse gate based on spectrally engineered sum frequency generation*, Opt. Express **19** (2011), 13770.
- [El +] M. E. El Demery et al., *Characterization of quantum pulse gates via spectral interferometry*, To be submitted.
- [El +23] M. E. El Demery et al., *Characterization of a temporal-mode sorter using multiple-delay crossed-beam spectral interferometry*. Proc. SPIE 12405, Nonlinear Frequency Generation and Conversion: Materials and Devices XXII (2023), 124050I.
- [EM12] M. E. El Demery and S. M. A. Maize., *Sideband control of optical bistability in tunnel-coupled double quantum wells*. Nonlinear Optics and Quantum Optics **46** (2012), 1.
- [EPR35] A. Einstein, B. Podolsky, and N. Rosen, *Can Quantum-Mechanical Description of Physical Reality Be Considered Complete?*, Physical Review **47** (1935), no. 10, 777–780.
- [FJ55] P. B. Fellgett and P. Jacquinot, *Fourier Transform Spectroscopy*, Advances in Optics and Electron Microscopy **7** (1955), 315–375.
- [Gao+13] W. Gao et al., *Quantum teleportation from a propagating photon to a solid-state spin qubit*, Nature Communications **4** (2013), 2744, DOI: 10.1038/ncomms3744.

- [Ha14] T. P. Harty and et al., *High-Fidelity Preparation, Gates, Memory, and Readout of a Trapped-Ion Quantum Bit*, Phys. Rev. Lett. **113** (2014), no. 22, 220501, DOI: 10.1103/PhysRevLett.113.220501.
- [Han+07] R. Hanson et al., *Spins in few-electron quantum dots*, Rev. Modern Phys. **79** (2007), no. 4, 1217–1265.
- [HM84] M. Hillery and L. D. Mlodinow, *Quantization of electrodynamics in nonlinear dielectric media*, Phys. Rev. A **30** (4 1984), 1860–1865, DOI: 10.1103/PhysRevA.30.1860.
- [Hor+09] R. Horodecki et al., *Quantum entanglement*, Rev. Modern Phys. **81** (2009), no. 2, 865–942.
- [HR06] S. Haroche and J.-M. Raimond, *Exploring the Quantum: Atoms, Cavities, and Photons*, Physics Today **59** (2006), no. 7, 36–42.
- [HT56] R. Hanbury Brown and R. Q. Twiss, *A Test of a New Type of Stellar Interferometer on Sirius*, Nature **178** (1956), no. 4537, 1046–1048.
- [IW99] C. Iaconis and I. Walmsley, *Self-Referencing Spectral Interferometry for Measuring Ultrashort Optical Pulses*, IEEE Journal of Quantum Electronics **35** (1999), no. 4, 501–509.
- [Kim08] J. Kimble, *The Quantum Internet*, Nature **453** (2008), 1023.
- [Kru+23] V. Krutyanskiy et al., *Entanglement of trapped-ion qubits separated by 230 meters*, Phys. Rev. Lett. **130** (2023), no. 5, 050803.
- [Kum90] P. Kumar, *Quantum Frequency Conversion*, Opt. Lett. **15** (1990), 1476.
- [Kur+15] G. Kurizki et al., *Quantum technologies with hybrid systems*, Proceedings of the National Academy of Sciences **112** (2015), no. 13, 3866–3873.
- [Lam95] W. E. Lamb, *Anti-photon*, Applied Physics B **60** (1995), 77.
- [LCS09] K. Laiho, K. N. Cassemiro, and C. Silberhorn, *Producing high fidelity single photons with optimal brightness via waveguided parametric down-conversion*, Opt. Express **17** (2009), no. 25, 22823–22837, DOI: 10.1364/OE.17.022823.

- [Lia+18] S. K. Liao et al., *Satellite-Relayed Intercontinental Quantum Network*, Phys. Rev. Lett. **120** (2018), no. 3, 030501.
- [Lod+15] P. Lodahl et al., *Interfacing single photons and single quantum dots with photonic nanostructures*, Rev. Modern Phys. **87** (2015), no. 2, 347.
- [LR09] A. I. Lvovsky and M. G. Raymer, *Continuous-variable Optical Quantum-state Tomography*, Rev. Modern Phys. **81** (2009), no. 1, 299.
- [Mai+01] A. Mair et al., *Entanglement of the orbital angular momentum states of photons*, Nature **412** (2001), no. 6844, 313–316.
- [Mar+17a] N. Maring et al., *Photonic quantum state transfer between a cold atomic gas and a crystal*, Nature **551** (2017), no. 7681, 485–488.
- [Mar+17b] N. Maring et al., *Photonic quantum state transfer between a cold atomic gas and a crystal*, Nature **551** (2017), 485–488.
- [Mar15] J. M. Martinis, *Superconducting Qubits: Current State of Play*, Annual Review of Condensed Matter Physics **6** (2015), 305–329, DOI: 10.1146/annurev-conmatphys-031214-014714.
- [Mar91] D. Marcuse, *Theory of Dielectric Optical Waveguides*, Academic Press, 1991.
- [Mey+17] E. Meyer-Scott et al., *Limits on the heralding efficiencies and spectral purities of spectrally filtered single photons from photon-pair sources*, Phys. Rev. A **95** (2017), 061803.
- [Mic81] A. A. Michelson, *On the Application of Interference Methods to Spectroscopic Measurements*, The London, Edinburgh, and Dublin Philosophical Magazine and Journal of Science **11** (1881), no. 65, 158–167.
- [Mon+14] C. Monroe et al., *Large Scale Modular Quantum-Computer Architecture with Atomic Memory and Photonic Interconnects*, Phys. Rev. A (2014).
- [Mon+95] C. Monroe et al., *Demonstration of a Fundamental Quantum Logic Gate*, Phys. Rev. Lett. **75** (1995), no. 25, 4714–4717.
- [MR59] J. M. Manley and H. E. Rowe, *General Energy Relations in Nonlinear Reactances*, Proceedings of the IRE **47** (1959), 2115–2116.

- [MRL08] M. Mohseni, A. T. Rezakhani, and D. A. Lidar, *Quantum-process tomography: Resource analysis of different strategies*, Phys. Rev. A **77** (3 2008), 032322, DOI: 10.1103/PhysRevA.77.032322.
- [MWC10] A. Monmayrant, S. Weber, and B. Chatel, *A newcomer's guide to ultrashort pulse shaping and characterization*, Journal of Physics B: Atomic, Molecular and Optical Physics **43** (2010), no. 10, 103001.
- [NC10a] M. A. Nielsen and I. L. Chuang, *Entanglement*, Quantum Computation and Quantum Information: 10th Anniversary Edition, Cambridge University Press, 2010, 99–110.
- [NC10b] ———, *Quantum Teleportation*, Quantum Computation and Quantum Information: 10th Anniversary Edition, Cambridge University Press, 2010, 347–355.
- [Nik05] D. N. Nikogosyan, *Nonlinear Optical Crystals: A Complete Survey*, Springer, 2005.
- [NPT99] Y. Nakamura, Y. A. Pashkin, and J.-S. Tsai, *Coherent control of macroscopic quantum states in a single-Cooper-pair box*, Nature **398** (1999), no. 6730, 786–788.
- [NTH12] C. Natarajan, M. Tanner, and R. Hadfield, *Superconducting nanowire single-photon detectors: physics and applications*, Superconductor Science and Technology **25** (2012), 063001.
- [Pan+12] J.-W. Pan et al., *Entanglement swapping for quantum networking*, Nature Photonics **6** (2012), no. 12, 726–734.
- [Pay92] J. Paye, *The chronocyclic representation of ultrashort light pulses*, IEEE J. Quan. Elec. **28** (1992), 2262.
- [Pel+12] J. S. Pelc et al., *Downconversion quantum interface for a single quantum dot spin and 1550-nm single-photon channel*, Optics Express **20** (2012), 27510–27519.
- [PSM87] S. Prasad, M. O. Scully, and W. Martienssen, *A quantum description of the beam splitter*, Optics Communications **62** (1987), 139.
- [QS16] N. Quesada and J. E. Sipe, *High Efficiency in Mode-Selective Frequency Conversion*, Opt. Lett. **41** (2016), 364.

- [QS17] N. Quesada and J. E. Sipe, *Why you should not use the electric field to quantize in nonlinear optics*, Opt. Lett. **42** (2017), no. 17, 3443–3446, DOI: 10.1364/OL.42.003443.
- [Ray+10] M. G. Raymer et al., *Interference of Two Photons of Different Color*, Opt. Comm. **283** (2010), 747.
- [RE24] K. J. Randles and S. J. van Enk, *Success probabilities in time reversal based hybrid quantum state transfer*, arXiv preprint arXiv:2401.08110 (2024), arXiv: 2401.08110 [quant-ph].
- [Red+13] D. Reddy et al., *Temporal mode selectivity by frequency conversion in second-order nonlinear optical waveguides*, Opt. Express **21** (2013), 13840.
- [Red17] D. Reddy, *Temporal-Mode Interferometry: A Technique for Highly Selective Quantum Pulse Gating via Cascaded Frequency Conversion in Nonlinear Optical Waveguides*, Ph.D. thesis, University of Oregon, 2017.
- [Rou+04] R. V. Roussev et al., *Periodically poled lithium niobate waveguide sum-frequency generator for efficient single-photon detection at communication wavelengths*, Optics letters **29** (2004), 1518–1520.
- [RR17] D. Reddy and M. Raymer, *Engineering temporal-mode-selective frequency conversion in nonlinear optical waveguides: From theory to experiment*, Opt. Express **25** (2017), 12952.
- [RR18] D. V. Reddy and M. G. Raymer, *High-selectivity quantum pulse gating of photonic temporal modes using all-optical Ramsey interferometry*, Optica **5** (2018), 423.
- [RRM15] D. V. Reddy, M. G. Raymer, and C. J. McKinstrie, *Sorting photon wave packets using temporal-mode interferometry based on multiple-stage quantum frequency conversion*, Phys. Rev. A **91** (2015), 012323.
- [RS12] M. G. Raymer and K. Srinivasan, *Manipulating the color and shape of single photons*, Physics Today **65** (2012), no. 11, 32–37, DOI: 10.1063/PT.3.1786.
- [Rüt+17] H. Rütz et al., *Quantum Frequency Conversion between Infrared and Ultraviolet*, Physical Review Applied **7** (2017), 1–7.

- [San+11] N. Sangouard et al., *Quantum repeaters based on atomic ensembles and linear optics*, Rev. Modern Phys. **83** (2011), no. 1, 33–80.
- [SF03] T. Suhara and M. Fujimura, *Waveguide Nonlinear-Optic Devices*, 1st, Springer-Verlag Berlin Heidelberg, 2003.
- [SR07] B. Smith and M. Raymer, *Photon wave functions, wave-packet quantization of light, and coherence theory*, New J. Phys. **9** (2007), 414.
- [SSW17] P. Senellart, G. Solomon, and A. White, *High-Performance Semiconductor Quantum-Dot Single-Photon Sources*, Nature Nanotechnology **12** (2017), no. 11, 1026–1039.
- [Ste07] D. Steck, *Quantum and Atom Optics*, 2007.
- [Tak+15] H. Takesue et al., *Quantum key distribution over a 40-dB channel loss using superconducting single-photon detectors*, Nature Photonics **9** (2015), no. 12, 827–831.
- [TG66] U. Titulaer and R. Glauber, *Density Operators for Coherent Fields*, Phys. Rev. **145** (1966), 1041.
- [Thy+09] K. Thyagarajan et al., *Generation of polarization-entangled photons using type-II doubly periodically poled lithium niobate waveguides*, Physical Review A - Atomic, Molecular, and Optical Physics **80** (2009), 1–8.
- [Tre69] E. B. Treacy, *Optical pulse compression with diffraction gratings*, IEEE Journal of Quantum Electronics **5** (1969), no. 9, 454–458.
- [Tre97] R. Trebino, *Frequency-Resolved Optical Gating: The Measurement of Ultrashort Laser Pulses*, Kluwer Academic Publishers, 1997.
- [VK04] A. P. Vandevender and P. G. Kwiat, *High efficiency single photon detection via frequency up-conversion*, J. Modern Opt. **51** (2004), 1433–1445.
- [WEH18] S. Wehner, D. Elkouss, and R. Hanson, *Quantum internet: A vision for the road ahead*, Science **362** (2018), no. 6412, eaam9288.
- [Wei00] A. M. Weiner, *Femtosecond pulse shaping using spatial light modulators*, Review of Scientific Instruments **71** (2000), no. 5, 1929–1960.

- [Wei11] A. M. Weiner, *Ultrafast optical pulse shaping: A tutorial review*, Optics Communications **284** (2011), no. 15, 3669–3692.
- [Yin+17] J. Yin et al., *Satellite-Based Entanglement Distribution Over 1200 Kilometers*, Science **356** (2017), no. 6343, 1140–1144.
- [Zha+14] Z. Zhang et al., *Unconditional Security of Time-Energy Entanglement Quantum Key Distribution Using Dual-Basis Interferometry*, Phys. Rev. Lett. **112** (2014), 120506.
- [Żuk+93] M. Żukowski et al., *Event-ready-detectors Bell experiment via entanglement swapping*, Phys. Rev. Lett. **71** (1993), no. 26, 4287–4290.